MICROSTRUCTURAL EFFECTS ON
DIFFUSION AND MECHANICAL
PROPERTIES IN DIFFERENT
MATERIAL SYSTEMS

Thesis by

Shi (Eric) Luo

In Partial Fulfillment of the Requirements for

the degree of

Doctor of Philosophy

Caltech

CALIFORNIA INSTITUTE OF

TECHNOLOGY

Pasadena, California

2018

Defended October 4, 2017

To my family

ACKNOWLEDGEMENTS

manuscript. Dr. Hai Xiao mentored me in various simulation techniques, and also guided me to approach a lot of material science problems from a more fundamental perspective. And last but not the least, Dr. Zachary Aitken has always been a great friend and mentor. His helped me hone my skills in various experimental scenarios, get familiar and truly own the instruments, and brought a sense of positivity and humor to many of our Friday subgroup meetings.

My friends and colleagues are also an integral part to my experience at Caltech. I have yet to see a more tightly bonded, friendly and jovial team than the Greer group, and I'm truly grateful to know all of these fellow scientists. I will treasure the memories of scientific discussions in front of a white board, the Beer Hours every Friday that can have subjects changing from sports to quantum mechanics in a mere minute, and the wild food adventures across the crawling city of Los Angeles. I consider myself really fortunate, to have these colleagues in lab that are also my best friends. Outside the group, I would also like to extend my thanks to the many friends that I met throughout my time at Caltech. This includes fellow APhMS students, my friends from CaltechC, and many more. A lot of us are already scattered across the world, but I'll look forward to meeting each and every one of you in the next chapter of our lives.

Lastly, I'd like to thank my parents Chunchuan Luo and Baizhi Liu for their unconditional love and support through the ups and downs of my life. They encouraged and nurtured even my wildest curiosities ever since I was a child, and it is with their support and encouragement that I was able to pursue my dream in science.

ABSTRACT

Material microstructures is a very broad subject that encompasses most of the field of materials science. Advances in materials characterization and small scale mechanical experiments have brought about progress in the understanding of microstructural features and mechanisms down to the nanometer scale. In contrast to bulk features and properties, the small length scale of these microstructures lead to many interesting properties, and often requires a material-by-material, and even localized region-by-region study. While a thorough understanding of microstructural effects even in one material system is way beyond the scope of this thesis, there are nonetheless many common themes and properties that link together microstructures and their effects on different materials, especially in terms of mechanical properties.

In this thesis, the effects of microstructural features such as grain boundaries, surface modification and structural hierarchy are investigated using two sample material systems: Cu-In-Ga-Se (CIGS) thin films and marine diatom frustules. We find that grain structures (or a lack there of) play a major role in both systems, and lead to differences in material stiffness, strength, and diffusion of species. The latter is also significantly affected by material defects across length scales, exemplified in CIGS by both microscopic voids and pores, and atomic scale like substitutional point defects. On the other hand, in diatoms, a low flaw density combined with an effective hierarchical design can propel the mechanical

property of relatively simple ingredients like amorphous silica, to achieve extraordinary mechanical strength. We will conclude by showcasing that we can generalize some of these knowledge on microstructural effects across material systems, to help designing manmade structures that fully capture the material-level and structural-level properties of natural marine diatoms.

PUBLISHED CONTENT AND CONTRIBUTIONS

Z. Aitken, **S. Luo,** S.N. Reynolds, C. Thaulow, J.R. Greer, *Microstructure provides insights into evolutionary design and resilience of Coscinodiscus sp. frustule*, Proc Nat'l Acad Sciences of the USA 113 (8), 2017-2022 (2016), DOI: 10.1073/pnas.1519790113

Personal contribution: Conducted material characterization (microscopy, spectroscopy) and finite element simulations, helped writing the manuscript.

S. Luo, C. Eisler, T. Wong, H. Xiao, C. Lin, T. Wu, C. Shen, J. Shieh, C. Tsai, C. Liu, H.A. Atwater, W.A. Goddard III, J. Lee, J.R. Greer, *Suppression of surface recombination in CuInSe2 (CIS) thin films via Trioctylphosphine Sulfide (TOP:S) surface passivation,* Acta Materialia 106, 171-181 (2016), DOI: 10.1016/j.actamat.2016.01.021

Personal contribution: Designed and conducted material characterization experiments and density functional theory simulations, wrote the manuscript.

S. Luo, J.-H. Lee, C.-W. Liu, J.-M. Shieh, C.-H. Shen, T.-T. Wu, D. Jang, J.R. Greer, *Strength, Stiffness, and Microstructure of Cu(InGa)Se2 Thin Films Deposited via Sputtering and Co-Evaporation,* Applied Physics Letters 105 (2) (2014), DOI: 10.1063/1.4890086

Personal contribution: Designed and conducted mechanical experiments and material characterization

TABLE OF CONTENTS

LIST OF ILLUSTRATIONS AND TABLES

Chapter 1 : Introduction

1.1 Microstructure in Materials

The science of materials is, to a large extent, defined in terms of different length scales and their interactions. These length scales can range from single atoms like point defects to ordered arrangement of atoms like grain boundaries and twin boundaries, to macroscopic features visible to the naked eye, like heterogeneous p-n junction in semiconductors. While different length scales would lend different properties to different material systems, it is often the focus on intermediate scales between atomic and macroscopic range that distinguishes a lot of the works in materials science from other fields like physics or chemistry on one end, and mechanical engineering and on the other. Although the exact range is often not properly defined, for the sake of this thesis, the term microstructure refers features in the range of 10 nanometers to 100 micrometers. Examples of features at these length scales include grain boundaries, surface morphology, hierarchy and deformation mechanisms such as dislocation and twinning.[1]

Material microstructures has been shown to govern a wide variety of material properties ranging from optical[2], thermal[3], electrical[4] to mechanical[5]. A great example of the prevalence of such effect is how grain size and grain boundaries has long been shown to be a major

factor that governs the mechanical properties of materials.[6,7] In metals, presence of grain boundaries and twin boundaries often lead to slip planes in a dislocation event[5]; in ceramics, grain boundaries are also crucial in fracture and lead to catastrophic failure of materials.[5]

The link between microstructure and their length scale has been of particular interest in the field of mechanics. A full body of literature has been dedicated to discovering the different effect of characteristic length scales in different material systems like fcc, bcc and hcp metal, metallic glass and engineering ceramics.[5,8,9] These so called "material size effects" are closely related to the intrinsic microstructure of the material, and the characteristic length scale that's present in the samples, and has been widely studied and accepted since their discovery. More recently, significant efforts have been devoted to using hierarchical design to introduce a mixture of small and large length scale features to otherwise monolithic material systems, to take advantage of the size effect and reach new materials properties space.[1,10–12] An extension of this approach leads to the concept of meta-materials, the careful architecture and hierarchy is used to create materials with completely new properties like negative refractive index.[13,14]

1.2 Effect of Grain Structures on Material Properties

While there is no clear definition and categorization of microstructures, a significant number of materials fall under one of the three categories: single crystalline, poly crystalline and amorphous. Single crystalline materials contain one single continuous crystal lattice

throughout the whole material, with no grain boundaries. Common examples of single crystalline materials include high purity silicon and diamond. In contrast, polycrystalline consists of many microstructural units of varying shapes, sizes and crystallographic orientations. These ordered microstructures are referred to as "grains", and properties related to them such as grain size and grain boundaries are often important in material properties.[6] Most metals and a lot of ceramics fall under polycrystalline, and their grain sizes can vary from hundreds of nanometers to several milimeters.[15] Amorphous materials have no ordered grain structures at any length scale, nor do they have any ordered packing of atoms like single crystalline materials. Instead, amorphous materials often exhibit the same microstructure regardless of the magnification or length scale. The most common amorphous material is probably silica (glass) and metallic glass, which are a special type of metal alloy with no packing order.[16]

Grain structure is a generalized term that includes features such as grain size, grain boundaries, surface morphology and potential ordered arrangements of grains.[17,18] These features, or the lack of them are generally talked about in the context of polycrystalline and amorphous materials respectively.

Effects of grain structures are an extremely complex and encompassing topic, and more often than not the results vary significantly or even exhibit contradicting trends across different material systems. Take the example of grain size versus stiffness in metals, the magnitude

and even direction of the effects can change based on different materials, like fcc and bcc metals and metallic glasses.[19–22] Another example is grain boundary effects in semiconductors. In silicon, grain boundaries serve as recombination sites for carriers leading to increased defect density of states[23], and often need to be passivated in high-efficiency devices[24]; in gallium nitride (GaN) and gallium arsenide (GaAs), grain boundaries decrease carrier mobility[25,26], create high defect concentration[27,28], and often lead to significantly decreased efficiency compared to single crystalline counterparts[29]; in chalcopyrite systems such as Cu-In-Se and Cu-Zn-Te, grain boundaries have a more complex effect, with conflicting reports on either increased[30] or decreased[31,32] efficiency with increasing grain size. These examples serve to show that there is no generalized theory that governs the effect of grain structures in materials. To the contrary these properties should be studied in a careful, case-by-case manner.

1.3 Materials Size Effect: Smaller is Stronger and More

Traditional strengthening mechanisms like work hardening, precipitate, and grain boundary strengthening are all related to particular microstructural features and length scales that defines them. Changing these dimensions, such as grain size and precipitate size, twin boundary spacing or dislocation density, can directly alter the mechanical properties of the bulk materials system. In a sense, the effects of these microstructural features on mechanical properties of materials is well-documented, and can be predicted in a deterministic manner.[5]

In the last decade, advances in small-scale mechanical experiments and simulations have revealed a deviation from this paradigm, as many materials exhibit unexpected behavior when their characteristic dimension goes below micrometer and sub-micrometer scale. For example, metals like aluminum (Al)[33,34] and nickel (Ni)[8,35–38] exhibits higher strength in uniaxial compression tests when the sample size decreases, while other metals like tungsten (W) and molybdenum (Mo) becomes more ductile at smaller sizes[39–42]; properties of intrinsically brittle materials like ceramics and metallic glasses also show various differences compared to their bulk counterparts when tested in a small-scale environment, ranging from distinct deformation mode and stiffness[43–45], to emerging ductility[46–50]. These phenomena where a material system exhibit new behavior and properties that deviate from the bulk when the characteristic dimension gets smaller, have since been referred to as materials size effect. As shown earlier, the exact effects differ across different material systems, and significant efforts have been dedicated to studying and tabulating them. While the mechanisms are still unclear in some systems like hexagonal close packed (hcp) metals, two trends are now widely accepted: (1) "smaller is stronger" in face centered cubic (fcc) metals, and (2) "smaller is more ductile" in ceramics and metallic glasses[5]. As evidenced by Figure 1.1 (adapted from Greer and Hosson[5] and Jang and Greer[51]) that shows a measured flow stress, which signifies onset of failure in fcc metals, as a function of sample dimensions; as well as a clear necking behavior observed in zirconium (Zr) based metallic glasses which typically experience brittle failure. As the material characteristic dimension gets smaller, deformation mechanism

changes in these systems. In fcc metals, the strengthening size effect is mostly attributed to dislocation pile-ups and interaction between dislocations with the limiting sample geometry[52–55], and in metallic glasses, the transition to ductility has been linked to the initiation, propagation and interaction between shear bands and sample boundary[44,56–59]. For these systems, the underlying material and microstructure remain the same, yet significant changes in their mechanical response were unequivocally observed as a function of the sample characteristic length. For this reason, characteristic dimensions have increasingly been referred to as part of the intrinsic microstructural property of a given material system.
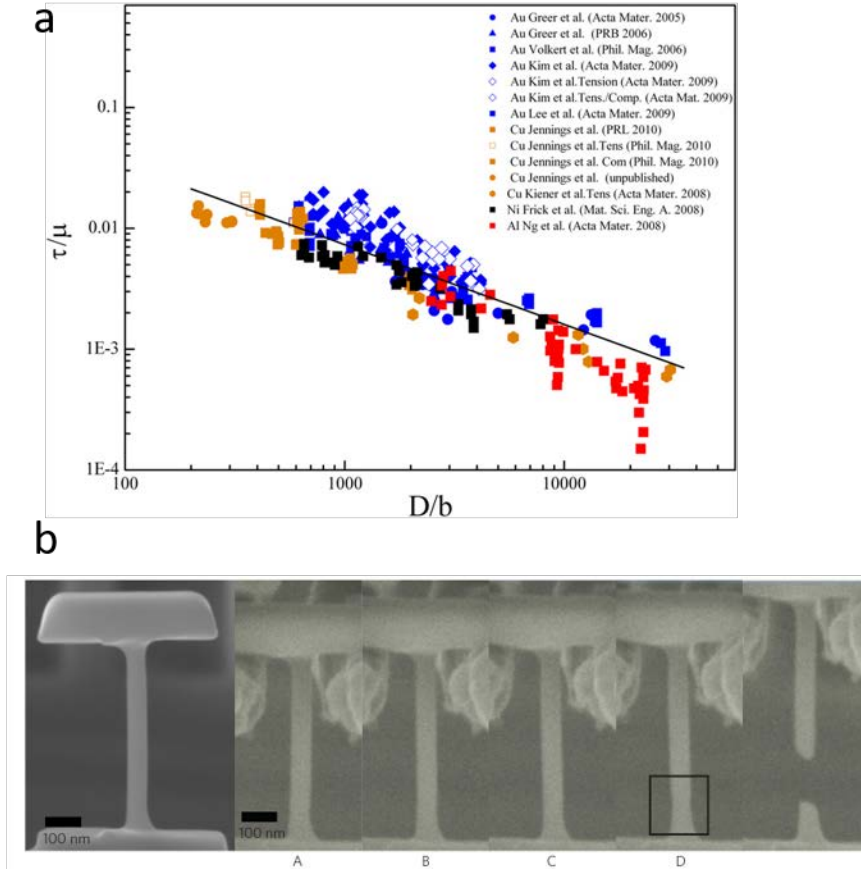
Figure 1.1 Size effect in materials. (a) Shear flow stress normalized by shear modulus on appropriate slip system for most face-centered cubic (fcc) metallic micro- and nano-pillars tested in compression and tension to date. Adapted from Greer et al.[5]; (b) SEM image of a typical as-fabricated 100-nm-diameter tensile sample, captured from a movie recorded during an *in situ* tension test. The square indicates necking that was observed before onset of failure. Adapted from Jang et al.[51]

1.4 Techniques and Challenges

1.4.1 Microstructural Characterization

Characterizing and visualizing the microstructures are often among the first steps in understanding their effects. Various spectroscopy and microscopy techniques are used to characterize nanometer-to-micrometer scale features. In particular, surface techniques such as scanning electron microscopy (SEM), x-ray photoelectron spectroscopy (XPS), energy dispersive electron spectroscopy (EDS), and cross-section techniques such as transmission electron spectroscopy (TEM) and electron energy loss spectroscopy (EELS) are all frequently utilized in the field.

SEM and TEM are at the core of materials characterization, as they enable us to visualize small scale samples and microstructural features, and can form the basis of many experiments such as *in-situ* testing. Both techniques visualize the sample in question based on energy loss from electrons after they interact with the sample[60,61]. SEM detects reflected electrons, and modern instruments can achieve ~10 nm resolution[62], while TEM uses the transmitted electrons and the state-of-the-art instrument and techniques can provide angstrom level resolution[63]. Recent advances, especially in aberration-corrected TEM, has fueled many exciting discoveries into the fundamental interactions in materials, for example Scott et al. achieved angstrom level resolution 3D tomography in different material systems[64]; and Oteyza et al. reported the first direct observation of covalent bonds between atoms[65].

However, working with TEM is a non-trivial task. As a significant number of electrons need to penetrate the sample to reach the detector on the other side, TEM sample thickness are in most cases limited to ~100 nm[61], even much smaller for ultra-high resolution studies. Traditionally these samples are prepared with a multi-step process that involves polishing, slicing and careful thinning using plasma mills such as argon (Ar) or neon (Ne)[61]. The biggest drawback of these sample preparation methods is they are not location specific, and it is almost impossible to know where the final sample slice will be beyond millimeter resolution during the sample fabrication process. In recent years, focused ion beam (FIB) milling has been gaining popularity and becoming a popular method for TEM sample preparation. FIB commonly uses Ga ions (although other ions such as Ne or Ar are also used) to physically bombard the sample in a controlled and precise dosage under vacuum condition[66]. This bombardment results in forced ejection of molecules and atoms from the sample site, in a similar fashion to that of source materials get ejected in a sputterer[67]. The ion beams are highly focused, enabling a resolution of ~ 10 nm in some state-of-the-art instruments[68], which would enable TEM samples to be fabricated in a highly location-specific fashion. However, using FIB comes with the drawback that bombarding the sample with a high dosage of high-energy ions would lead to radiation damage and ion implantation[69,70]. These implantation effects can sometimes completely change facets of material properties of the sample in question, such as amorphizing a region[40], or embrittle a material mechanically[71,72]. Recent advances in better beam control at low voltages[68], and more material-specific studies of the

radiation-implantation effect from FIBs suggests that using a low enough energy, the radiation effect can be contained to be within ~10 nm of the sample thickness[73], or almost completely eliminated in some materials systems[74]. Mechanical studies on FIB-milled micro pillars compared to electro-plated pillars of the same geometry show minimal difference in terms of strength and stiffness[75,76]. Building upon all these findings, using FIB milling to make site-specific TEM samples is now more popular than ever, and enabled many novel studies especially in the field of small scale mechanics and fracture, where site-specific TEM samples enabled viewing of the sample microstructures after mechanical experiments[20,77].

Finding better ways to probe the elemental composition of a material, in the form of either quantitative spectra or qualitative distribution maps is a field in itself. A lot of effort has been dedicated to improving the resolution of such measurements as well as the accuracy of quantitative analysis of the measured results[78]. EDS and EELS are two very similar techniques that provides information on elemental composition by measuring the energy of electrons after interaction with the sample. For EDS, the energy of emitted electrons from sample excitation is measured, whereas for EELS, the energy loss in transmitted electrons is measured instead. More quantitative and precise EDS and EELS measurements often takes place inside a TEM[78], and can drastically benefit from the advance in TEM instruments and sample fabrication techniques. State-of-the art resolution for EELS and EDS have reached single nanometer range, and recent works include atomic-scale mapping and quantification using EDS[79,80], and EELS[81,82] in various materials systems. However, quantitative analysis

of EDS and EELS results is highly sensitive to background noise and impurities present inside the sample chamber, such as the sample holder or chamber contamination. Thus for proper quantitative analysis, it is imperative to conduct the experiment on a "standard" first: a sample with a known composition that contains the same element as the actual sample.[78] On the other hand, qualitative studies such as elemental distribution maps, do not require such standard samples, and are seeing increasingly widespread use in both academic and industrial settings.

1.4.2 Nano-mechanical Testing

Small scale mechanical testing, including nanoindentation, cantilever bending, micro-pillar compression and other experiments, is a highly active field that often leverages advances in instruments and other techniques in materials science. The field was revolutionized decades ago following a method to extract material stiffness from nanoindentation experiments that accounts for substrate effects by Oliver and Pharr[83]. In the years that follows, an entire body of work has emerged to perfect the method and provide better understand of the different artifact that could arise in these experiments, such as dislocation pile-ups[84,85], substrate effect (sink-ins)[86], and pre-yield strain bursts (avalanches)[87,88]. In the recent years, following the advances of in-situ instruments and techniques, an increasing number of nano-mechanical experiments are conducted in an in-situ fashion often inside scanning electron microscopes[89]. In particular, Greer et al. conducted the in-situ tension-compression experiments on FIB-

milled micropillars of different materials, inside an SEM that has been custom fitted with a nanoindentor arm[90]. These experiments combine real time video observation of the sample region of interest (ROI) with precise measurements of the mechanical response, and provide insights into microstructural effects on mechanical properties in various materials systems such as metals[21,91], metallic glasses[49], ceramics[92], and other materials like carbon nanotubes[93].

Recent advances in in-situ mechanical testing instruments has seen commercial products that can be directly plug-and-use in different SEM chambers[94]. However, challenges remain to improve the load-cell limits of these systems to match that of a traditional nanoindentor arm, to enable longer travel distance of the tip, and testing of bigger samples. it is also increasingly important to separate various contribution to the overall mechanical response of the sample, such as from the substrate, from the instrument, and from the boundary conditions, away from the real material property[95]. Since many of these factors will have a more significant impact on the overall response of the system as the sample size becomes smaller. This phenomena has been observed in different small-scale mechanical experiments, from nanoindentation[8,95] to fracture experiments[96,97]. It is thus crucial to consider such size effects when designing and analyzing small scale mechanical experiments.

1.4 Research Plan and Thesis Layout

In this work we investigate vastly different materials systems, and investigate how microstructures and hierarchy affects their mechanical, electrical and chemical properties. In doing so we provide results that add to the knowledge base of these materials systems, but more importantly methods and knowledge that can be generalized in the further exploration of "designing" and "engineering" materials.

This thesis is outlined as follows: Chapter 1 gives an overview of materials microstructure and their effects. Chapter 2 discusses microstructure of Cu-In-Ga-Se (CIGS) thin film solar cells. Chapters 3 through 4 provide two example studies that investigates how fabrication processes and microstructure alterations affects the mechanical and chemical properties of CIGS thin films, and how these effects translate to solar cell performances. Chapter 5 switches gears and discusses hierarchical design and its application in natural hard biomaterials. Chapter 6 presents results from studies of microstructure and hierarchies in marine diatom frustules, with a focus on mechanical properties. Chapter 7 furthers this discussion and explores methodologies with which we can utilize diatom's unique combination of microstructure and hierarchical design to make stiff and strong man-made materials. Chapter 8 concludes the thesis with final remarks and suggestions of future work.

Chapter 2 : CIGS Solar Cells

We focus our first study of microstructural effects on Copper indium/gallium selenide (Cu(In,Ga)Se$_2$ or CIGS) thin films. CIGS is a mixture of CuInSe$_2$ (CIS) and CuGaSe$_2$ (CGS), which are both p-type polycrystalline semiconductor material belonging to the I–III–VI$_2$ family that have a tetragonal chalcopyrite crystal structure[98]. CIS and CGS have almost identical crystal structures and properties, since In and Ga are in the same family. For this reason, CIGS also share most of these structure and properties since it's an ordered mixture of CIS and CGS. Aside from instances where we specifically discuss their differences, CIS/CGS/CIGS will be referred to interchangeably in the following chapters. We will briefly discuss the history, research and current landscape of CIGS in this chapter; in Chapter 3 we will look into how different deposition processes lead to drastically different CIGS film microstructure, and how this affect the film property; in Chapter 4 we will investigate a surface passivation process that seemingly improve CIGS efficiency without changing the microstructure, and show that it achieves this by slight alteration of key defect specie concentration in the film through enhanced solid-state diffusion.

2.1 CIGS solar cells and history

CIS were first synthesized in 1953 by Hahn et al. as a candidate for photovoltaic applications[99]. A device efficiency of 12% for single crystalline cells was reached soon after

in 1974[100]. In 1976, Kazmerski et al. reported CIS/CdS thin film solar cell fabricated by evaporating $CuInSe_2$ powder in the presence of excess Se vapor[101]. Although the efficiency is relatively low at ~5%, this marks the first instance of the popular sputter/evaporation – selenization process, that would later become one of the most prevalent in low cost CIGS deposition. Boeing company later developed another important process by co-evaporating Cu-In- Se elemental sources at a pre-determined ratio, achieving a higher efficiency of ~ 9.4%[102]. After this, interest and development in CIGS thin films began to take off with breakthroughs such as fabricating CIGS by alloying CIS and CGS, doping the absorber layer with sodium (Na) and improvements in fabricating other layers in the solar cell stack such as cadmium sulfide (CdS) n-type buffer layer[103]. Fast forward to the present, the state-of-the-art CIGS cells has an efficiency value of 22.8%, achieved by a complex multi-stack cells with improved hetero-junction properties from a potassium fluoride (KF) layer deposited between the absorber and buffer layer[104]. This makes CIGS one of the highest efficiency thin film solar cell materials, as shown in the energy road map released by National Renewable Energy Laboratory (NREL)[105], as shown in Figure 2.1.
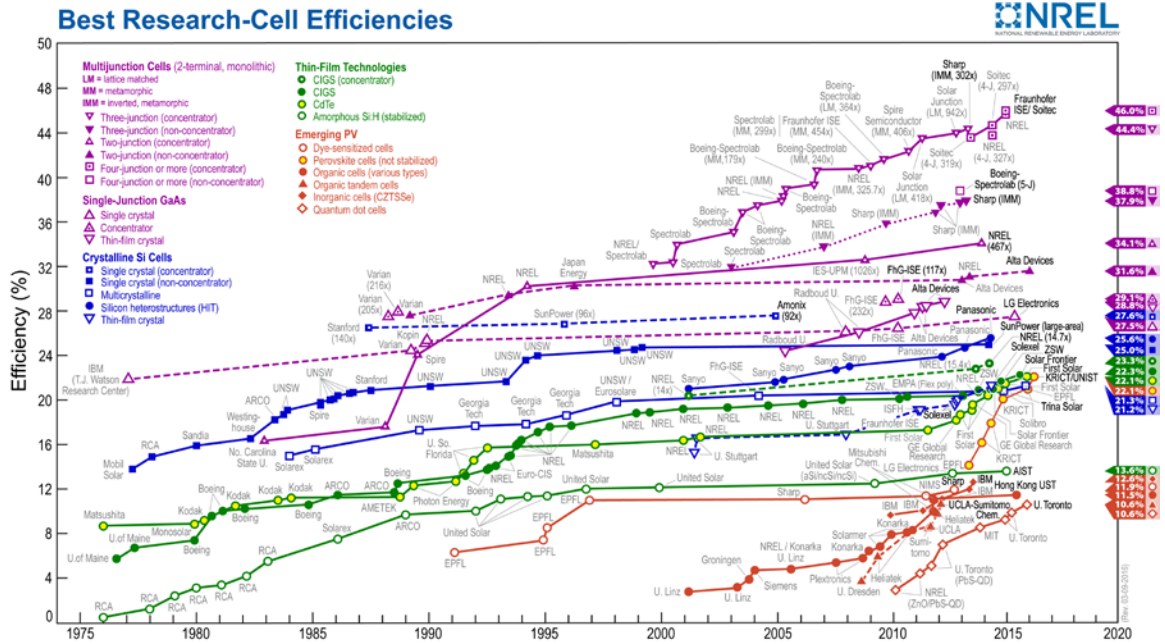
Figure 2.1: Efficiency chart for different photovoltaic materials, adapted from NREL[105]

There are several reasons why CIGS is able to reach such high efficiency among thin film photovoltaic materials:

(1) **High absorption coefficient:** CIS and by extension CIGS have among the highest absorption coefficient among known semiconductor materials[106]. This high absorption coefficient enables CIGS thin films to absorb significant amount of solar energy at a very low thickness. For commercial purposes an absorption layer thickness of 2 – 2.5 um is usually enough[98], which makes CIGS ideal for flexible substrates application. Coupled with the low density of CIGS relative to other materials such as gallium arsenide (GaAs), makes

it a prime candidate for low-weight thin film PV applications such as outer-space and portable devices[107].

(2) **Tunable bandgap:** CIS has an intrinsic bandgap of 1.04 eV[99]. This bandgap increases with increasing Ga concentration as the CIS/CGS alloy mixture shifts towards CGS. With 100% Ga replacement, the bandgap becomes 1.7 eV[108]. This enables 'tuning' of CIGS bandgap by varying In/Ga ratio, and makes CIGS a potential direct bandgap material (a direct bandgap material goes through a one-step excitation-absorption process under incident light) for a wide range of wavelength, as the bandgap can be tuned to accommodate most of the solar spectrum within 1 mm[107]. This tunable bandgap also results in a tunable, and potentially higher open circuit voltage (V_{oc}), as V_{oc} is directly proportional to the bandgap.

(3) **Low cost manufacturing:** CIGS is a polycrystalline material, the mixture of In and Ga also lends to some additional tolerance in terms of material stoichiometry. As a result, although the fabrication process of CIGS is complex and multi-steps in nature, during each step there is less stringent requirements on crystal growth or deposition rates[98]. This is in stark contrast with many other thin film solar cell materials such as GaAs, which usually requires highly directional deposition using techniques such as molecular beam epitaxy (MBE)[109,110]. Therefore, the deposition process for CIGS is comparatively easier to scale up. Its high absorption coefficient also makes very thin absorber layers possible, thus enabling roll-to-roll process on flexible substrates as a potential manufacturing option[103].

Current commercial and laboratory CIGS solar cells usually adopt a multi-stack layout, as shown in Figure 2.2. Key components of the stack include (from the top): Transparent conducting oxide (TCO) / zinc oxide (ZnO) window layer to allow light to shine through; CdS n-type buffer, CIGS p-type absorber, molybdenum (Mo) back contact and substrate. A p-n junction is created between CdS and CIGS where carriers are collected to generate current. The sputtered Mo back contact is crucial as it can reflect electrons in the CIGS layer back to the p-n junction[111]. Soda lime glass (SLG) is a common choice of substrate in CIGS devices, and serves the dual purpose of (1) providing a light-permitting, mechanically rigid backbone for the solar cell panel and (2) being the source for Na diffusion into CIGS layer to enhance various electrical properties[112].
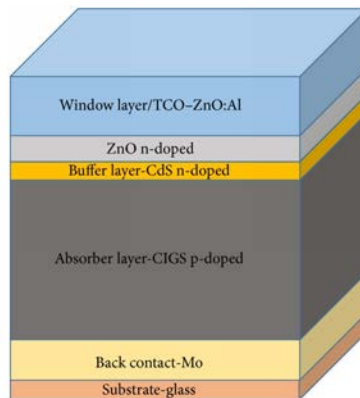
Figure 2.2 Schematic drawing of a typical CIGS solar cell stack

While CIGS has shown great promise for thin film photovoltaic applications, some limitations and challenges remain for its commercialization. (1) While the requirement on crystallinity during growth process is relatively low, maintaining compositional uniformity between different regions and among different batches is crucial in CIGS fabrication[98], as a horizontal compositional gradient or mismatch has been shown to significantly affect device performances[113,114]. As a result, complex control scheme is required in all CIGS deposition processes, leading to increased equipment and maintenance cost. (2) The fabrication process for CIGS is potentially scalable and more economically viable options compared to some alternative materials. However, the raw materials for CIGS is relatively expensive, especially In and Se, which are supply-limited, which casts an uncertainty on the prospect of the commercialization for CIGS. Given these two limitations, although as a material CIGS is showing great promise in efficiency and application, the current production volume is still small compared to the more mature Si-based solar cells[107].

2.2 Deposition Methods of CIGS thin films

A wide variety of thin-film deposition methods have been used to deposit CIGS, including sputtering, evaporation and other multi-step processes[98,103]. With the goal of commercial production in mind, the ideal deposition method should meet the following criteria: (1) low cost with high deposition rate, (2) high compositional uniformity over large areas, and (3) high efficiency ratings close to laboratory standards. Under these criteria, two methods have

been seeing high popularity in recent years: co-evaporation of Cu, In/Ga and Se elemental sources, and sputtering/evaporation of Cu, In/Ga followed by vapor selenization.

2.2.1 Co-evaporation

Arguably the most well studied method to deposit CIGS, co-evaporation uses heated Cu, In, Ga and Se sources to achieve direct line-of-sight delivery at high temperatures (usually ~ 600 degrees)[115]. Different evaporation profiles have been studied over the years, and the overall device efficiency has been steadily increasing with the complexity of these profiles, as shown in Figure 2.3. The single-stage evaporation (Figure 2.3 (a)) was the original process proposed by Hahn et al[99], in which the fluxes of different species as well as other deposition conditions are kept constant throughout the process, and is still a viable process up to this day[116]. Later studies reveal that introducing a Cu-rich (defined as Cu/(In,Ga) ratio > 1) region in the film can lead to improvements in film quality[117], which lead to the development of the bi-layer evaporation process (Figure 2.3 (b)) where Cu flux is kept intentionally high at the beginning of the process and decreases after parts of the film has been deposited. Gabor et al. later proposed an additional step in which In/Ga mixture is first deposited with Se at a lower temperature (~ 300 degrees), to form $(In,Ga)_2Se_3$, Cu is then introduced in the same bi-layer fashion until stoichiometry is reached[118]. This process has since been referred to as the three-stage-process (Figure 2.3(c)), and has been shown to result in smoother film morphology[98,119]. Finally, building on the bi-layer or three-stage process, further alteration

to In/Ga ratio can be introduced in any of the deposition stages to create a varying bandgap along the film thickness (Figure 2.3(d)). This lead to the graded bandgap approach and devices that can be specifically designed for different applications[120,121].
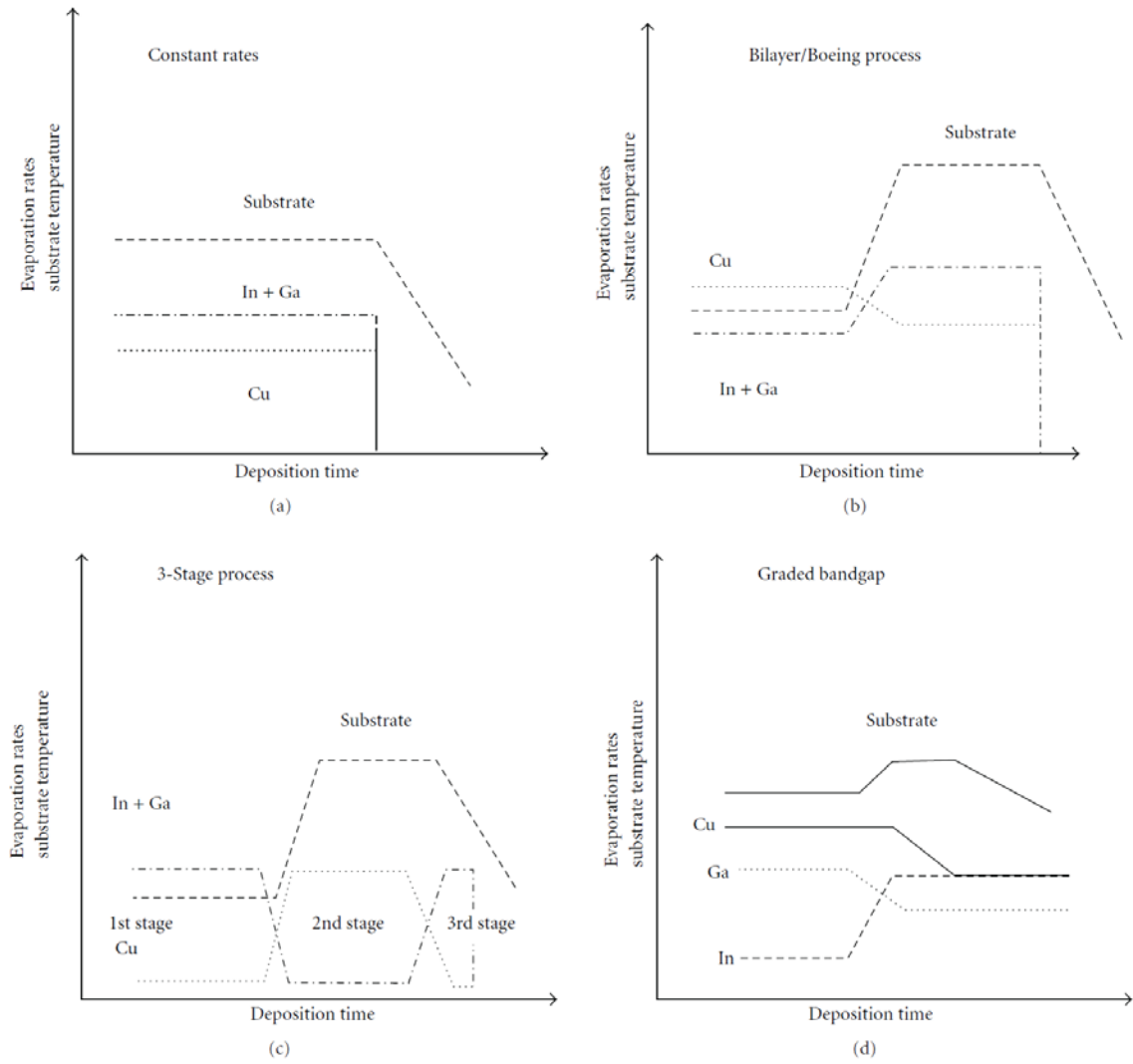
Figure 2.3 Schematic illustration of different co-evaporation processes. (a) single stage process, (b) bilayer or Boeing process (c) three stage process and (d) In, Ga and Cu fluxes are varied during the growth to obtain a graded structure. In processes (a)–(d), a constant Se flux is also supplied. Adapted from Singh et al.[103]

Using the three-stage method, commercial CIGS solar cells with efficiency 19.3% has been produced[122]. However, the yield from these co-evaporation processes is limited by the size of the evaporation chamber, which in turn is not yet suitable for commercial up-scaling. As a result, mass production using the co-evaporation process is still being developed.

2.2.2 Sequential Selenization

In the sequential approach, Cu, In/Ga metals are deposited first via a low cost deposition option, the metal mixture are then annealed in a Se atmosphere at high temperature[123]. As the name suggests, these approaches are defined by the separation of the metal-deposition and the chalcogenization reaction with Se which brings the mixture back to stoichiometry. One key advantage brought about by this separation is that metal deposition can be carried out in a low-temperature, low-cost, high-yield fashion. Sputtering[124–127] and thermal evaporation[128–131] are both commonly used, and can lead to a potential 10 fold yield increase compared to co-evaporation[132]. After the initial deposition, the Ci-In-Ga mixture is then annealed in a Se-rich environment. Both elemental Se vapor[133] or H_2Se gas[31,127] can be used for this purpose, in a high-temperature reaction at between 400 to 500 degrees[31,133]. The advantage of using H_2Se is the reaction happens at atmosphere pressure and is easy to control. However H_2Se is highly toxic, which brings additional requirement on the manufacturing environment[127]. On the other hand, using elemental Se vapor often requires thermally

evaporating a solid Se source[98], which significantly increases the manufacturing cost. As a result, H_2Se vapor is more commonly used in industrial manufacturing of CIGS.

One downside of the two-step process is lower device efficiency compared to the co-evaporation process. Among the highest-efficiency CIGS cell reported from a two-step process, H_2Se process led to an efficiency of 16.2%[31], and Se vapor has an efficiency of 19.2%[134] both of which are lower than state-of-the-art co-evaporation process at 22%[114]

2.2.3 Non-vacuum techniques

In an effort to lower the capital cost in CIGS manufacturing, non-vacuum based approaches to CIGS deposition has been receiving increasing attention[135]. Similar to vacuum based two-step methods discussed in 2.2.2, these non-vacuum methods also split the deposition into two stages: deposition of precursor materials at low temperature, and conversion of precursors into CIGS, usually via high-temperature annealing in a chalcogenide atmosphere[136]. The precursor deposition process can then be categorized based on the deposition method as (1) electrochemical process, (2) particulate process, and (3) solution based process[136]. The main advantages for these methods are the potential of lower production capital cost by getting rid of the vacuum deposition instruments; as well as the ease of up-scaling. Significant progress has been made in this area within the past few years[136], however most efforts are still limited to improving the specifics of each recipe.

Electro-chemical deposition processes involve depositing Cu/In/Ga elements in a single-[137] or multiple- step[138,139] electro-chemical process, while using complexing agents to bring the deposition potentials close to each other. Optimization for these processes is relatively difficult and several studies reported sub-par compositional uniformity after the annealing step[138,140]. Highest efficiency values for the electrochemical processes are 13.8% on glass[141] and 15.4% on stainless steel[142].

Particulate techniques include using screen printing[143], spray coating[144], or spin coating[145] to apply metal precursors in particle form, followed by a high-temperature annealing/sintering step similar to that in other multi-step processes. These methods have the highest efficiency among non-vacuum methods, with recent work using particle mixture of metal oxides and selenide powders achieving 17.1% efficiency on a flexible foil substrate[146]. However, sintering In/Ga metal particles require high temperature and specialized equipment, which in turn lead to significant cost increase for commercial production. The particle properties also factor heavily into the performance of the final product[145].

Solution-based approaches are relatively new, and involves reactions between hydrazine based compounds and organometallics, in a full solvo-thermal reaction[147]. A highest efficiency of 15.2% has been reported recently[148]. However, hydrazine compounds are highly toxic and reactive, as a result most solution-based methods are currently limited to laboratory scale.

2.3 Factors that affect CIGS solar cell efficiency

Due to various promising features of the CIGS material, there has been sustained interest in investigating and optimizing the factors that affect CIGS device efficiency. The majority of such research and breakthrough are focused on improving the stack[117,149] and fine tuning the deposition parameters[31,150]. More recently, there has been increasing interest in understanding the microstructure and process in CIGS absorber layer[131,151,152]. The most notable breakthrough and advances in understanding these effects are summarized in this section.

2.3.1 Na Diffusion and Incorporation

Na incorporation and its effect in CIGS has been widely studied both in terms of film microstructure[153,154] and electrical properties[150,155]. It is now widely accepted that low concentration of Na in CIGS has various beneficial effects in photovoltaic applications: (1) Na can bond with the Se in the film to form $NaSe_x$, which can reduce formation of undesirable donor-type Se vacancies that are common in CIGS[156]; (2) Na incorporation creates acceptor-type NaIn defects and passivates the grain boundary, leading to improved Voc, FF and device efficiency[157], (3) Na at film surface will lead to formation of In_2O_3 and Ga_2O_3, thus creating a Cu-deficient condition[158], which has been shown to reduce surface recombination between CIGS and CdS layers[159,160], (4) Na incorporation in CIGS can also lead to a decrease in device resistivity by up to two orders of magnitudes[161,162].

In addition to improving electrical performance of CIGS devices, Na has also been shown to affect grain growth during CIGS deposition. Several reports have suggested that Na enhances formation of grains with (112) orientation, as well as introducing (112) faceted textures on normal (110) grains [153,154]. There have also been various reports about Na affecting grain size in CIGS. Some authors suggested an increase in grain size in CIGS films with Na concentration ranging from 0.1% to 0.5%[154,163,164], some reported very similar grain size observations in CIGS grown with and without Na[112,165,166], and still some reported decreasing grain size with Na introduced via different methods[112,150,167]. Such differences in literature reports may be due to that Na incorporation and its effect on CIGS grain structure is highly dependent on the deposition processes and conditions, and at the same time these processes and conditions have their own unique effect on the grain structure of deposited CIGS films[168].

In summary, although the detailed mechanisms and effects are still unclear, it is widely accepted that Na incorporation plays an important role in both CIGS grain growth and microstructure formation, as well as impacting electrical performance of CIGS solar cell devices. A low Na concentration ($< 0.5\%$) is usually desired, and Na has been shown to congregate to grain boundary and film surfaces[157].

The most widely used method to introduce Na into CIGS is through diffusion from SLG substrate. During the high temperature deposition steps (in both co-evaporation and selenization pathways), Na will diffuse from the SLG substrate through the Mo layer, into

the CIGS film[169]. On other substrates such as polymer or metals, a thin (~ 10 nm) layer of sodium fluoride (NaF) is often deposited before the CIGS layer as a Na source, and the diffusion would activate in a similar thermal process[170].

2.3.2 Mo Back Contact

Several metals like platinum (Pt), gold (Au), silver (Ag) and molybdenum (Mo) have all been investigated as electrical back contact for CIS-based solar cells[171–173]. Mo eventually became the popular choice due to its stability at high temperature, resistance to alloying with Cu and In, and low contact resistance[173]. Mo back contact on CIGS is usually deposited via evaporation[174] or sputtering[175,176] on SLG substrate. Several reports have discussed the effect of residual stress[174,175], adhesion[173,177], and directionality[31] of Mo layer. In particular, Mo layer with residual compressive stress has been shown to possess more uniform grain structure and ultimately lead to better electrical performance, whereas Mo layers with residual tensile stress have been reported to have a more porous structure[174,175,178].

There have been inconclusive reports about the type of electrical contact between Mo layer and CIGS. Early results suggested that a Schottky-type barrier between CIS/Mo contact[179,180]. However, later work by Shafarman et al.[181] suggested the contact to be Ohmic as a direct result of $MoSe_2$ formation near the interface, this suggestion was later echoed by several other reports[182–184]. Additional studies on the formation and role of $MoSe_2$ layer later

proposed that MoSe$_2$ layer is mechanically stable with good adhesion and does not significantly impact the electrical performance of the CIGS devices[185,186].

The thickness and crystallinity of Mo layer is also important to the operation and performance of CIGS solar cells. For CIGS films deposited on a SLG substrate, Na would diffuse into the absorber layer through the Mo contact. As a result, increased Mo layer thickness would impede the Na diffusion process and lead to negatively affect electrical performance[187]. Yet a Mo layer that's too thin would lead to adhesion issues, as well as a decreased fill factor[187,188]. A well-accepted thickness for Mo layer in CIGS solar cells is between 200 to 400 nm[187,189,190].

2.4 Summary

CIGS-based materials are popular candidates for thin film photovoltaic applications mainly due to their high absorption coefficient and unique tunable bandgap. Remarkable progress has been made in this field over the last few decades. Currently CIGS have among the highest efficiency rating in thin film solar cell materials. The ever-increasing amount of research and industrial efforts into CIGS and related devices also show tremendous potential for further enhancement.

However, most of the research in the field of CIGS is confined to fine-tuning and improving on specific deposition processes, and different research groups still rely on special recipes

and processes to achieve high efficiency. While this approach has been effective so far in terms of improving the device efficiency of both laboratory-scale and commercialized productions, the underlying material properties of CIGS is not yet fully understood, especially those that are related to microstructural differences in CIGS films as a result of different deposition recipes. Some processes, like the effect of Na, has been acknowledged and widely studied, but a lot of the work still focus on finding a direct link between fabrication process (introducing Na) and device performance (efficiency), and relatively little attention and effort has been dedicated to the material-level mechanisms. As such, a more systematic and fundamental approach to understanding the physics and chemistry related to the CIGS material is required to further advance this field.

Chapter 3 : Microstructure and Mechanical Properties of CIGS Thin Films from Different Fabrication Processes

The effect of different deposition methods on film quality and device performance is an important area in the field of CIGS. However, as discussed in Chapter 2, most of the research in this space focus on fine-tuning the deposition recipes and trying to find a direct link between deposition process and device performance. In this chapter which is adapted from Luo et al.[191], we use a more fundamental approach to investigate the microstructure and mechanical properties of CIGS thin films fabricated by (1) selenization of pre-sputtered Cu-In-Ga mixture and (2) co-evaporation of each constituent.

The efficiency disparity between films deposited via these two methods is linked to differences in morphology and microstructure. Scanning probe microscopy (SPM) and SEM results show that selenized films have rougher surface morphology and poor adhesion to molybdenum back contact. TEM and EELS analysis reveal multiple voids and pores near the Mo layer in selenized films and a depletion region of Na and Se around the voids. Residual stresses in each film are analyzed using curvature measurements, with co-evaporated films sustaining biaxial stresses of 1.23 GPa. Elastic Hertzian contact model is applied to

nanoindentation data and reveal the indentation modulus of 68.9±12.4 GPa, which is in agreement with previous reports. Uniaxial compression experiments are performed on FIB-milled nanopillars with diameters of ~500nm extracted from co-evaporated films and revealed the elastic modulus of 70.4±6.5 GPa. This equivalence of the elastic moduli suggests that the microstructural differences manifest themselves after the yield point. Typical plastic behavior with two distinct failure modes is observed in the extracted stress-strain results, with the respective yield strength of 640.9±13.7 and 1100.8±77.8 MPa.

3.1 Introduction

$Cu(In,Ga)Se_2$ (CIGS) has become one of the most promising materials for thin film photovoltaics, with recent achievement in efficiency of over 20% on soda lime glass (SLG) substrates[122] as compared with traditional polycrystalline silicon cells.[192] The thin film nature of CIGS makes it a suitable material for depositing onto lightweight flexible substrates like polyimide (PI) films and metal foils, amenable to roll-to-roll processing, with efficiencies of 18.7% reported for CIGS on PI films[193] and of 17.9% on titanium foils[194]. Current studies of CIGS solar cells have been mainly focused on improving the fabrication process and on fine-tuning cell parameters to achieve better device performance[119]. Little effort has been dedicated to developing a fundamental understanding of the CIGS material, which is necessary to improve the device performance and to optimize the requirements for constituents within the device. Such analysis is required to understand the apparent disparity

in performance between Cu-In-Ga-Se devices fabricated by two different processes: (1) co-evaporation of each individual constituent and (2) selenization of the pre-sputtered Cu-In-Ga mixture. The latter has superior economic potential but its performance has been reported to be ~3/4 of that for the co-evaporated cells, as shown in Figure 3.1.
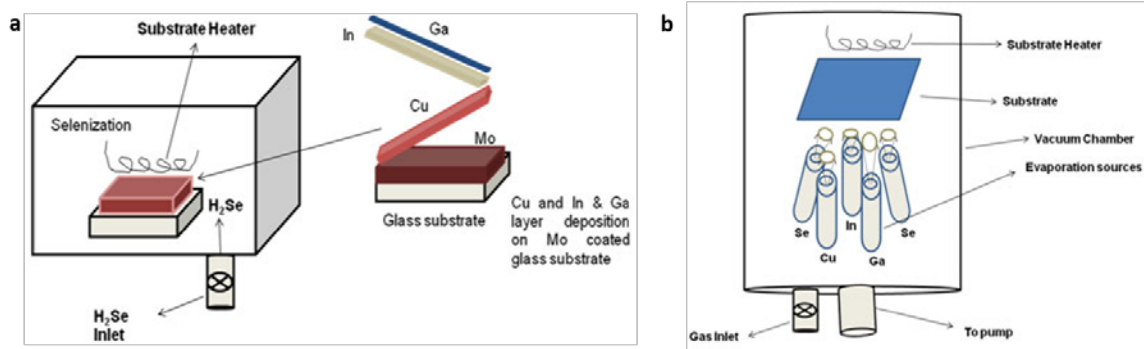
Figure 3.1 Schematics of common deposition processes for CIGS:
(a) sequential selenization, (b) co-evaporation

This chapter presents microstructural and mechanical characterization of the 1.5 μm -thick CIGS films deposited by co-evaporation and selenization techniques with the goal of developing a better fundamental understanding of the CIGS material and to gain insight into the effects of material processing on device performance.

3.2 Methods

CIGS sample fabrication: Multilayered stacks of CIGS samples were provided by National Nano Device Laboratories (NDL) of Taiwan. Two separate batches were created, one using

selenization and the other co-evaporation processes. In both processes CI(G)S was deposited on top of a 700 nm molybdenum back contact layer sputtered on SLG substrate in a two-steps process. During the first step, a 70 nm-thick Mo layer was sputtered at a pressure of 10 mTorr; with additional 630nm sputter-deposited during the second step at 3.6 mTorr. Cu and In metal precursors were sputtered onto the Mo contact at 2.8 mTorr and 150 $^{\circ}$C, followed by selenization with Se vapor with N_2/H_2 carrier gas at 550 $^{\circ}$C. The total thickness of the CIGS absorber layer was measured via SEM to be 1.6 ± 0.2 μm. For the co-evaporated CIGS, the absorber layer was deposited onto 0.46 cm^2 Mo coated SLG substrates using a 3-step homogeneous thermal evaporation of elemental Cu, In, Ga and Se at 550 $^{\circ}$C. The overall thickness of the co-evaporated absorber layer was 1.7 ± 0.1 μm. A schematic of the sample stack is shown in Figure 3.2.
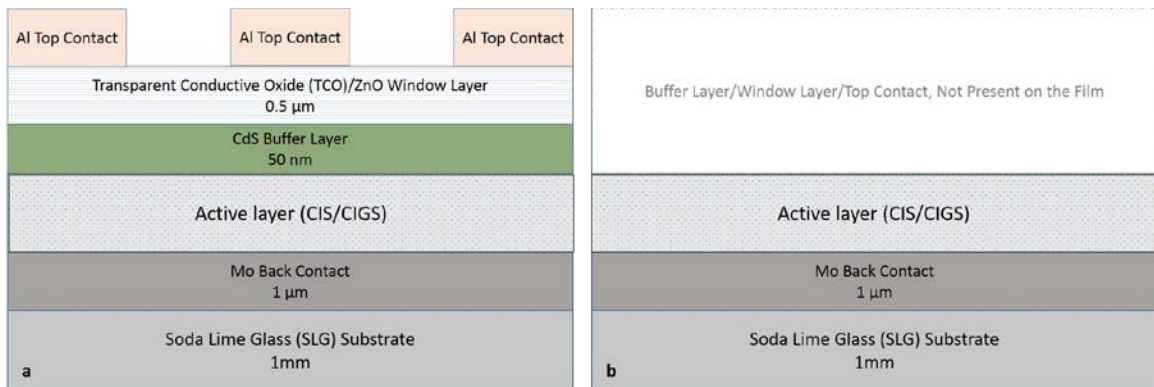
Figure 3.2 Schematics of the CI(G) sample used in this study with thickness measurements of each layer. (a) full cell, (b) films on substrates. In both cases two different absorber materials are tested: selenized CIS and co-evaporated CIGS

Imaging and characterization: SEM images were taken using FEI Nova Nanolab 200 FIB/SEM, and EDS within the same instrument was used to ascertain the chemical composition of the sample. Samples were cut into 1 cm × 1 cm pieces for SEM imaging. All SEM images were acquired at a tilt angle of 52 °. Grain sizes were estimated based on the SEM and TEM images in the following manor: (1) multiple lines of the same length were drawn across the image in both horizontal and vertical directions emanating from different, randomly chosen points; (2) number of intersections of the lines with the grain boundaries were recorded; (3) the average grain size is taken to be the total length of the lines divided by the total number of intersections. A micromanipulator (Omniprobe) within the FIB (FEI, Nova200) was used to create nano-pillars for uniaxial micro-compression experiments and to extract site-specific locales within the films. Bright-field images and EELS maps were generated from both samples using Tecnai TF-30 TEM (FEI). The curvature induced in the substrate after the deposition of films was measured using KLA Tencor Laser Interferometer for the neat SLG substrates, SLG/Mo and SLG/Mo/CIGS samples.

Mechanical experiments: Nano-indentation into selenized films was conducted using a standard Berkovich tip in Hysitron TI-950 Nanoindenter with the tip effective radius of curvature of ~150 nm. Indentation depth was kept at 100 nm to avoid the effects of the substrate; experiments were conducted under a constant displacement rate of 1 nm s^{-1}. Nano-pillars were compressed in a different nanoindenter (Agilent G200) using a custom-milled diamond flat punch with 8 μm diameter in the Continuous Stiffness Measurement (CSM)

mode. Cylindrical nano-pillars were milled out from the co-evaporated films using a Ga FIB and compressed with a custom-fabricated 8 μm-diameter diamond flat punch in the nanoindenter (G200, Agilent). A total of five tests were conducted, with the top pillar diameters of 431 ± 15 nm, bottom diameters of 639 ± 32 nm, and heights of 1.7 ± 0.2 nm. A maximum strain of 0.3 and a strain rate of $5 \times 10^{-3} /s$ was prescribed for all tests. Load-displacement data was collected in the continuous stiffness measurement mode (CSM) of the instrument. For each test, the pillar of interest was located using a top-view 150X optical microscope; the distance between the indenter head and the microscope objective was then calibrated on the surface of the sample away from the pillar following a standard methodology.[195] The indenter head would subsequently locate the sample surface near the pillar and descend to 5 μm above it. After a 300-second hold, the indenter tip would approach the pillar at a rate of 5 nm/s until establishing contact, after which the compression experiment commenced at the set strain rate. During each test, real-time load on the pillar, displacement from the point of contact, and the harmonic contact stiffness were measured and recorded. The load-displacement data was then converted to stresses and strains following Greer et al.[196] and Lee et al.[197].

3.3 Results

3.3.1 CI(G)S Samples and Device Measurements

While the selenized samples in this work did not contain gallium, it is reasonable to assume that the mechanical and structural properties of CIS should be similar to those of CIGS because of the similarities in the crystal structure and in the atomic sizes of $CuInSe_2$(CIS) and $CuGaSe_2$ (CIGS)[198.] The chemical composition of each sample is provided in Table 3.1. The current density-voltage (J-V) characteristics were measured on functional cells made from CIS and CIGS films deposited using both methods, as shown in Figure 3.3.

Table 3.1 Electrical measurements of the samples used in this
study, including selenized (S-) and co-evaporated (C-) samples

	J_{sc} (mA cm^{-2})	V_{oc} (V)	FF (%)	Efficiency (%)
S-CIS	30.88	0.42	64.6	9.31
S-CIGS	30.08	0.56	63.9	11.96
C-CIGS	34.804	0.64	72.1	16.06
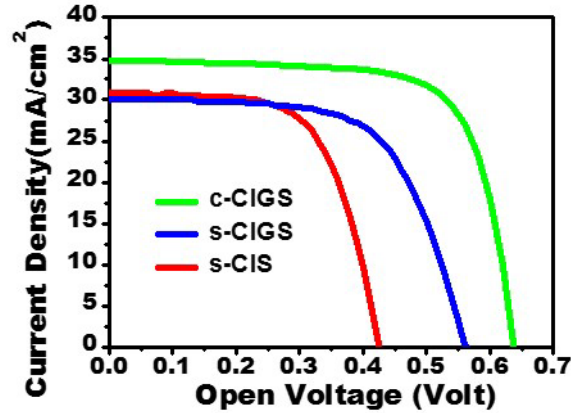
Figure 3.3 Measured current-voltage characteristics of selenized
and co-evaporated CI(G)S solar cells. c-CIGS: co-evaporated
CIGS films; s-CIGS: selenized CIGS films; s-CIS: selenized CIS
films

3.3.2 Morphology and Microstructure

Figure 3.4 shows representative SEM images from top and cross-sectional views and the topology of the top surface of the selenized (Figure 3.4(a,c,e)) and the co-evaporated (Figure 3.4(b,d,f)) films as revealed by SPM. The selenized film appears to have a faceted grain structure, which contributes to the surface roughness. Cross-sectional images (Figure 3.4(c,d)) suggest that the selenized films did not adhere well to the underlying Mo and contained multiple voids and buckle-like gaps between the film and the substrate. Figure 3.4(e,f) shows SPM images of both films' surfaces obtained using the cantilever in the Hysitron TI-950 nanoindenter with a standard Berkovich tip. Average roughness was

recorded at 173.5 ± 17.1 nm for the selenized film, a value almost an order of magnitude rougher than the 33.5 ± 4.3 nm in the co-evaporated film. Grain sizes were measured to be similar, 114.6 ± 23.1 nm for selenized films and 147.7 ± 84.9 nm for co-evaporated films based on the SEM images. The large variation in the grain sizes of the co-evaporated films stems from the grains being slender and anisotropic, in contrast to the selenized films, which appear faceted and isotropic. Electron Back Scatter Diffraction (EBSD) analysis was attempted to better quantify the orientation and sizes of the grains but the substantial surface roughness rendered EBSD patterns impractical.
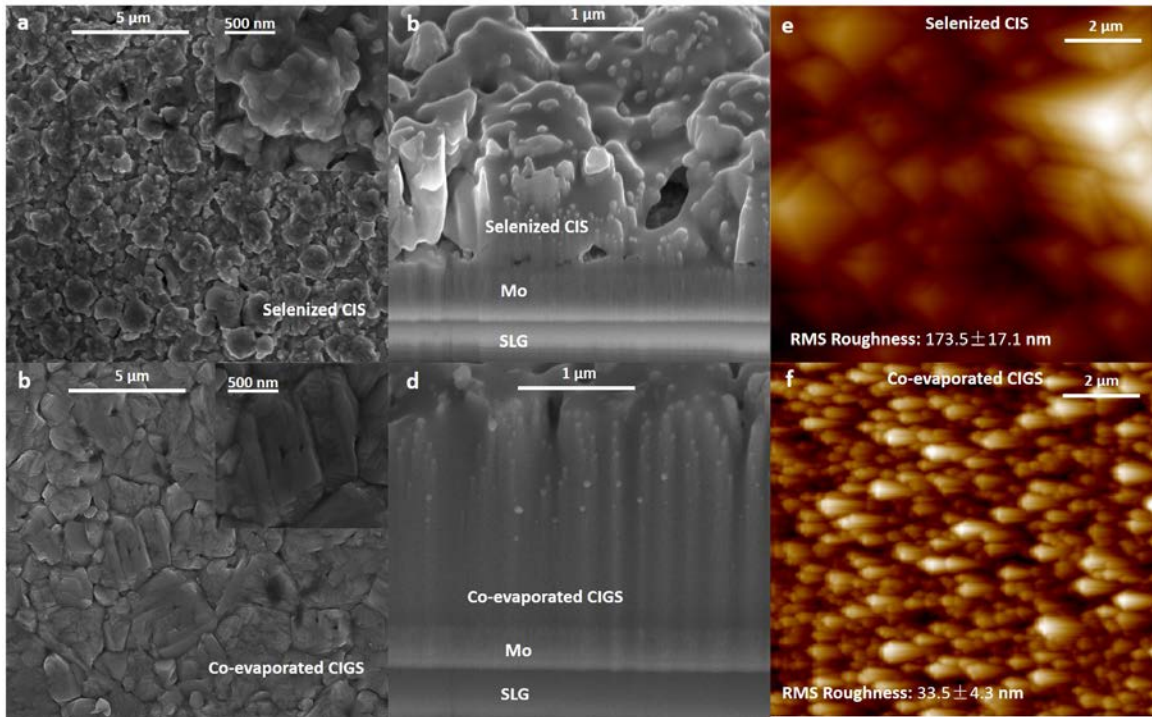
Figure 3.4 SEM and SPM characterization of surface microstructure of selenized and co-evaporated CI(G)S films.

Representative SEM images of (a) selenized CIS and (b) co-evaporated CIGS films taken top down with the zoomed-in view of the center location shown in the inset in the top right corner; and cross-section views of (c) selenized CIS and (d) co-evaporated CIGS films taken at 52º. SPM images in (e) and (f) correspond to the same films. For the RMS roughness values, measurements over 10 different regions on the same film were used for each type of films

Figure 3.5 shows the bright field TEM images of the cross-sections and the EELS concentration maps for Se and Na for both sets of films. TEM images reveal that the grain sizes in the co-evaporated film were uniformly distributed around 1 μm, while the distribution of grain sizes in the selenized film was broad, ranging from 50 nm to 2 μm. Multiple ~200nm-diameter voids were observed in the selenized film close to the interface with the underlying Mo layer. Concentration profiles of Se and Na revealed a depletion region in the selenized film at ~100 nm above the interface, which coincides with the location of the voids. In the co-evaporated samples, Se and Na were homogeneously distributed throughout the thickness of the film. SEM and TEM images also revealed that the grains within the Mo films were columnar and visibly bent in the co-evaporated films, while those in the selenized films were relatively straight.
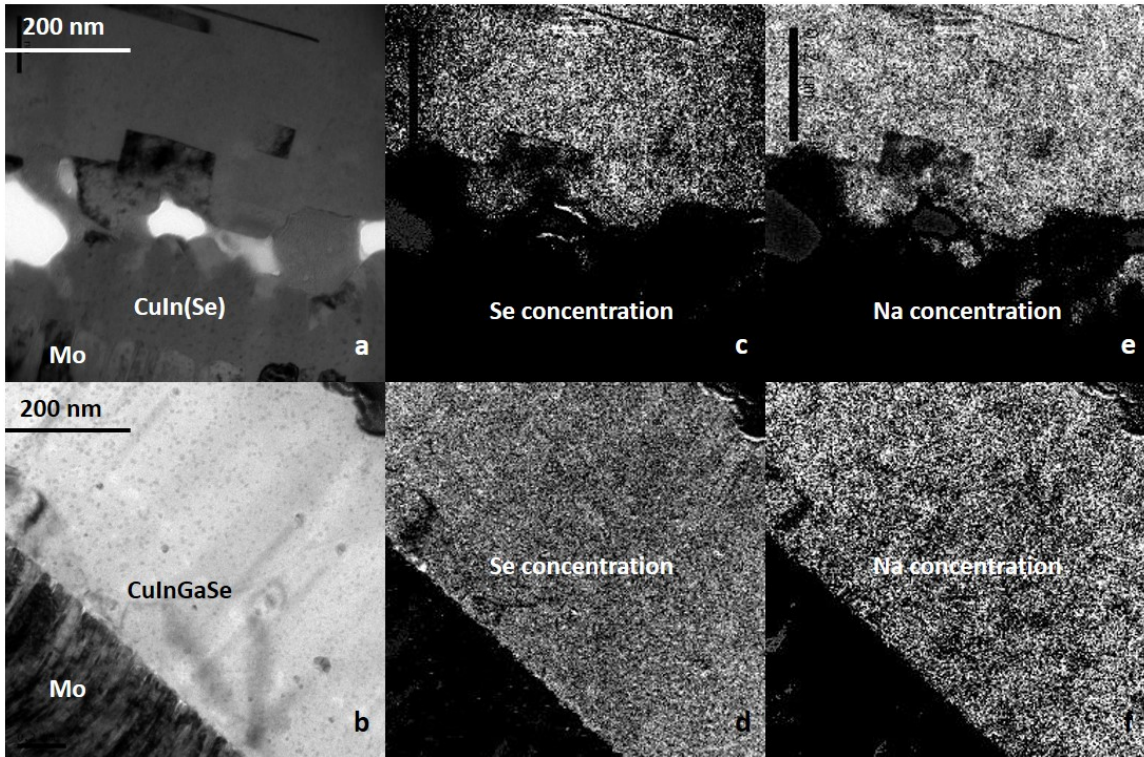
Figure 3.5 TEM and EELS analysis of selenized and co-evaporated CI(G)S films. Bright field TEM image of (a) selenized and (b) co-evaporated films; Se concentration of (c) selenized and (d) co-evaporated films; and Na concentration of (e) selenized and (f) co-evaporated films. Note that in (a) the CuIn(Se) region does not contain Se, hence the different notation.

3.3.3 Stresses in the Co-evaporated CIGS Films

Substrate curvature induced in the co-evaporated samples when cooling down to room temperature was measured to estimate the residual stress in the film. This technique uses laser interferometry to measure the deflection of the substrate from its original state and then

estimates the residual stress in the film from the measured curvature through Stoney's Formula:[199]

$$\sigma_f = \left(\frac{E_s}{1-\nu_s}\right)\frac{t_s^2}{6t_f}K \tag{3.1}$$

The average bending radii of the substrate were measured on 3 sets of samples: (1) the as-fabricated SLG substrates which had the dimensions of $2\text{cm} \times 2\text{cm} \times 2\text{mm}$, (2) SLG substrates produced from the same batch as in Equation. 1 with 700 nm thick Mo films deposited via a two-step sputtering process, first at 150 °C, and second – at 550 °C, and (3) the same SLG substrates with the 700 nm thick Mo and 1.5 µm-thick CIGS film evaporated on top of the stack at 550 °C. The stress state in the films is likely more complex than biaxial so this approach is used as an estimate, which has been shown to be robust for many material systems in thin film on a substrate form[200]. Thin film deposition parameters, as well as the measured radii of curvature of the substrate and the calculated biaxial thin film stresses σ_f in each film, calculated by Equation 3.1, are shown in Table 3.2. The high stress predicted by Stoney's relation after the CIGS deposition step is consistent with the bending of the Mo layer observed in SEM and TEM images. (Figures 3.4 and 3.5)

Table 3.2 Sample deposition conditions, measured radius of curvature and residual stress calculated using Stoney's relation

Layer	Thickness [nm]	Process temperature [°C]	Radius of curvature [m]	Residual Stress [MPa]

Glass substrate	1×10^6	N/A	228	N/A
Molybdenum	800	<150	237.3	14.7 (tensile)
CIS (selenized)	1300	Max. 550 (three step process)	N/A	N/A
CIGS (co-evaporated)	2000	550	7.43	1230 (Compressive)

3.3.4 Elastic Properties of the Selenized CIGS Films

The substantial surface roughness of the selenized films prevented conducting similar curvature measurements on these samples. To determine the Young's modulus and stiffness of the selenized films we used nanoindentation and analyzed the elastic loading data via Hertzian contact model,[201] with the deforming grain and the tip of the indenter approximated as elastically-contacting spheres. Indentation was conducted in a Hysitron TI-950 Triboindenter with a Berkovich tip that has an effective radius of curvature R_1 of 150 nm;[202] the radius of the contacting grains R_2 was measured in the SEM to be 500 ± 42 nm by methods outlined in 3.2. Note that larger grains were selected under the optical microscope for contact to better approximate spherical contact, hence the grain radius listed here is significantly larger than the average grain size of the film. An effective radius R was then calculated using Equation. 3.2, and inserted into the Hertzian contact model (Equation. 3.3) along with the measured load-displacement data, F and d, to calculate the isotropic reduced modulus of the film, E_r.

$$\frac{1}{R} = \frac{1}{R_1} + \frac{1}{R_2} \tag{3.2}$$

$$d = \left(\frac{9F^2}{16RE_r^2}\right)^{\frac{1}{3}} \tag{3.3}$$

All tests were performed under displacement-rate control using a feedback algorithm, to an indentation depth of 100 nm at a prescribed displacement rate of 1 nm/s, and then fully unloaded at a rate of 4 nm/s, where a slower loading rate was used compared to unloading since the initial loading part is of major interest in this analysis. A 300 seconds-long hold was set up before each indentation to ensure that the thermal drift rate was less than 0.1 nm/s. The nanoindentation data along with the Hertzian model fit are shown in Figure 3.6. A reduced modulus of 68.9 ± 12.4 GPa was obtained from 9 data sets, which agrees with the previously reported value of 73.4 GPa by Lin et al.[203] and with the bulk modulus for single crystalline CIGS measured by X-ray Absorption Spectroscopy to be 72±2 GPa.[204] Cautions should be taken towards the Hertzian treatment however because it assumes isotropic elasticity, whereas the CIGS film is polycrystalline and non-isotropic. In addition, considerable margin of error could be introduced in the approximation of grains as perfect spheres.
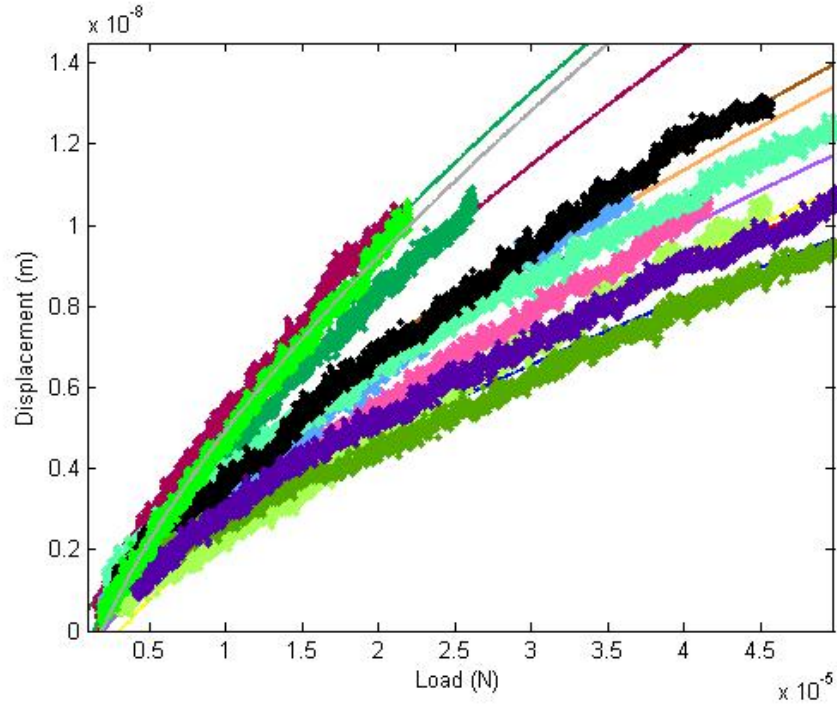
Figure 3.6 Nanoindentation results for selenized CIS films. Displacement (*d*, y-axis) and load (*F*, x-axis) data from indentation of selenized film overlaid with curve-fitting results from Hertzian contact theory. For each data set, up to 1% of total displacement was considered to be in the linear regime and showed in the graph. The smeared curves are the actual data while the thin curves are the polynomial fit according to Equation 3. The standard Berkovich tip used and the individual grains on the film were approximated as spheres. R square values of above 9.87 were reached for all data sets

3.3.5 Mechanical Properties and Deformation of Co-Evaporated Films

The analysis of compressive response of the CIGS nanopillars was conducted following the methodology of Greer et al..[196] We assumed perfectly cylindrical pillars and uniaxial compression to estimate global stresses and strains from the load-displacement data. Conservation of volume during plastic deformation allows us to calculate the instantaneous compression area A_p and pillar length L_p and initial pillar height L_0 and area A_0, with the latter being an average of top and bottom area of an individual pillar. The total measured displacement, d_{tot}, can be expressed in terms of the elastic component d_{el} and plastic component d_p, while d_{el} can be expressed in terms of measured stiffness $k_{measured}$ and load on pillar F, which were continuously recorded by CSM; d_p would then give us instantaneous pillar length L_p, and the stress σ.

$$A_0 L_0 = A_p L_p \tag{3.4}$$

$$L_p = L_0 - d_p = L_0 - (d_{tot} - d_{el}) = L_0 - \left(d_{tot} - \frac{F}{k_{measured}} \right) \tag{3.5}$$

$$\sigma = \frac{P}{A_p} = \frac{P L_p}{A_0 L_0} \tag{3.6}$$

The true strain ε consists of the elastic part ε_{el}, given by Hooke's Law, and plastic part ε_p, related to L_p:[196]

$$\varepsilon = \varepsilon_{el} + \varepsilon_p = \frac{F}{E_{CIGS} A_p} + ln\left(\frac{L_0}{L_p} \right) \tag{3.7}$$

Where E_{CIGS} is Young's Modulus for CIGS, obtained from the stiffness k_{CIGS}:[197]

$$E_{CIGS} = k_{CIGS} \frac{L_p}{A_p} \tag{3.8}$$

Which was in turn obtained from $k_{measured}$ and taking into account the substrate effect using the formula proposed by Sneddon:[205]

$$k_{CIGS} = \left(\frac{1}{k_{measured}} - \frac{1}{k_{Sneddon}} \right)^{-1} \tag{3.9}$$

$$k_{Sneddon} = \frac{2E_{Mo}}{1 - V_{Mo}^2} \sqrt{\frac{A_{Mo}}{\pi}} \tag{3.10}$$

Where Young's Modulus and Poisson's Ratio for Molybdenum, E_{Mo} and ν_{Mo} were used instead of those for the SLG substrate because the displacement at the bottom of the pillar is likely on the order of 10 nm,[197] well within the thickness of the Mo film. Area at the bottom of the pillars was used as the contact area between CIGS pillars and Mo layer A_{Mo}. E_{Mo} was measured by nanoindentation into the as-deposited Mo film as 329 GPa, and ν_{Mo} was taken to be 0.3. Young's modulus of co-evaporated CIGS E_{CIGS} was obtained as 70.4 ± 6.5 GPa. Yield stresses were calculated using the traditional 2% offset method, and will be discussed in detail in Section 4.3. Stress vs. strain data are shown in Figure 3.7 (b,e) with representative SEM images of nanopillars before (3.7(a,d)) and after (3.7(c,f)) deformation.
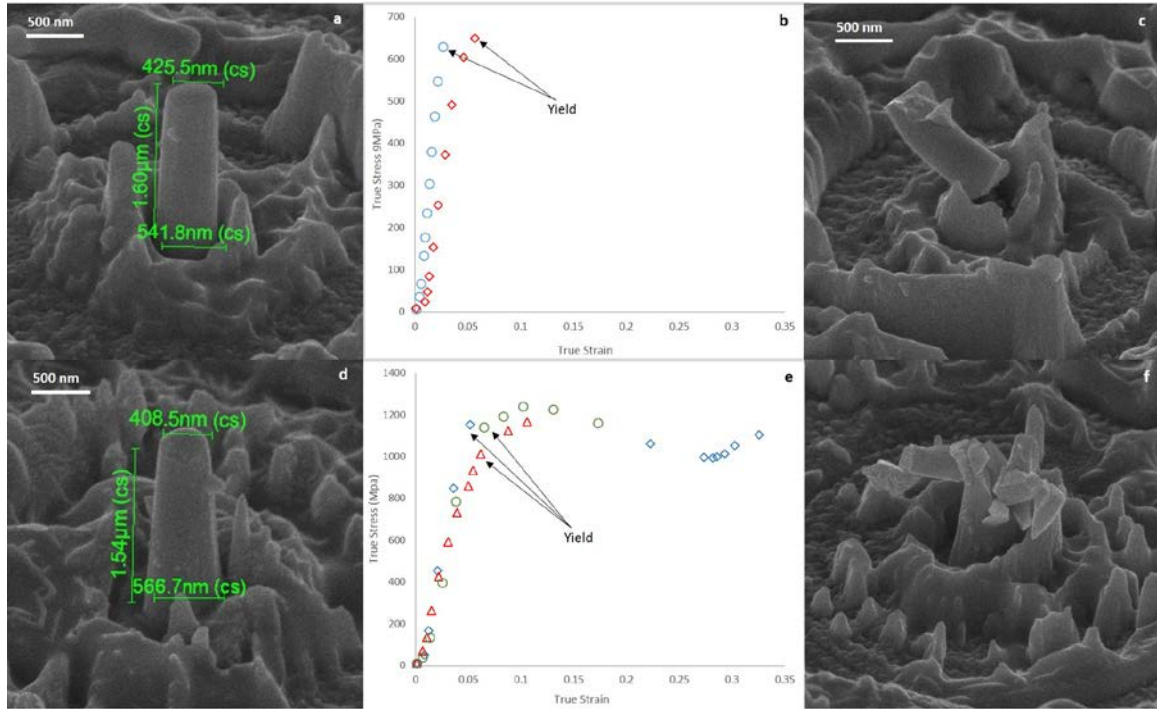
Figure 3.7 Uniaxial compression experiments of nanopillars from co-evaporated CIGS. SEM images of 500 nm diameter nanopillars before (a,d) and after (c,f) compression. (b,e) show the two representative types of stress strain behavior in terms of loading portions of true stress-strain curves, where in (b) the pillars failed plastically near the bottom, and in (e) they shattered during compression. The identified yield points are shown on individual curves.

3.4 Discussion

3.4.1 Morphology and Microstructure

Several morphological and micro-structural factors might be contributing to the electrical performance disparity between devices made with selenized and co-evaporated films as shown in Figure. 3.3. SEM and SPM surface profiles shown in Figure 3.4 convey that the surface roughness in selenized films is an order of magnitude higher than that in the co-evaporated ones. This roughness in the CIGS absorber layer would affect the chemical bath deposition of the CdS buffer layer and cause a poor contact at the CIGS/CdS interface.[133] The associated effect on the boundary carrier exchange may potentially result in inferior device performance. The region near the interface with Mo shows partial delamination and voids within the CIGS film. Similar voids have been observed and were associated with the low Se flow rate during selenization process[133]. They could also be mechanical in origin, for example as a result of buckling from high compressive stress in the CIGS film[206]. Voids and delamination would have an adverse effect on the mechanical integrity of the film and would eventually affect the device operational reliability.[178]

Figure. 3.5 shows a compositional analysis within the cross-section of the sputtered CIGS film along its height obtained via EELS. This image shows that the film is depleted in the Se and Na in the vicinity of the Mo layer and around the voids; this region appears to consist entirely of Cu and In with no trace of Se or Na. A similar absence of Se has been explained

by the micro-structural defects in the film, in this case the voids, which hinder the selenization process.[207] The absence of Na is likely a result of its fast diffusion rate since the source of Na in the film is the SLG substrate, unlike the Se that enters the film from the top. In contrast, both Se and Na were homogeneously distributed in the co-evaporated film, with no observable depletion region.

The effect of the depletion region on device performance may be significant. While the Cu/In mixture without Se won't be able to function properly and will hinder carrier movement, the lack of Se near the Mo layer also results in the absence of the $MoSe_2$ intermediate layer. The $MoSe_2$ usually located near the CIGS/Mo interface has been reported to be responsible for a significant efficiency increase by creating a quasi-Ohmic contact between CIGS and Mo layer.[185] Na has been identified as a critical constituent for the functionality and efficiency of CIGS operation because it creates a higher net carrier concentration which leads to improved open circuit voltages and fill factors[155]. Na incorporation has also been reported to be crucial in governing absorber morphology and grain growth,[208] although a quantified optimal amount of Na does not exist, with contradictory observations reported.[151,153,165] It has been proposed that Na mainly exists in CIGS as substitutional point defect at Cu and In vacancy sites and alter the dopant concentration and bandgap by introducing acceptor-type defect complex such as Na_{In}[209]. Other reports show Na has a strong preference for the charge-neutral Cu substitution and affects the electronic properties indirectly by means such as introducing new diffusion pathways.[157] Despite inconsistent reports, the conclusion can nonetheless be

drawn that the observed Se/Na/MoSe$_2$ depletion region will affect the carrier transport near the Mo back contact in selenized CIGS films, and possibly contribute the inferior electronic properties observed in devices made with the selenized cells. These observations of the depletion region near the voids suggest that the diffusion process during selenization step was affected by structural defects in selenized film, which establishes a link between device performance and film microstructure.

Grain size has also been shown to be closely related to device performance of CIGS. For example, it has been reported that more uniform grains lead to better device efficiency[98]. Yet no quantifiable correlation between grain size and device performance because increasing[150] and decreasing[210] grain sizes within a certain range have both been reported to improve device performance. Nonetheless, it is generally agreed that larger grain sizes lead to greater diffusion lengths of the photo-generated carriers and reduce recombination at grain boundaries.[211] While the measured grain size in the co-evaporated films has considerably larger variation with respect to orientation, the mean value is significantly higher than that measured for the selenized films, which could also be a factor in the device performance.

3.4.2 Thin Film Stress Analysis

To estimate the residual stresses in thin CIGS films we measured the substrate curvature. Excessive surface roughness rendered the selenized films unsuitable for such measurements. The results for the co-evaporated film reveal nearly 100-fold increase in compressive stress

after the deposition of CIGS onto the Mo layer. Prior to depositing CIGS the stress in Mo layer was tensile, at 14.7 MPa, on the same order as previously reported[206]. The stress increased by several orders of magnitude, to -1.23 GPa after the co-evaporation, with negative values indicating a compressive stress. While similar experiment for the selenized film was not possible, it is reasonable to assume that it would also have a high residual compressive stress because the material properties and the deposition temperature are similar between the two films. The different curvatures in the substrate before and after the deposition of CIGS suggests that the residual stress must arise from the co-evaporation process of CIGS, likely because of the mismatch in their thermal expansion coefficients (CTE) (9×10^{-6} C^{-1} for SLG substrate, 4.8-5.9 $\times10^{-6}$ C^{-1} for Mo contact and 11.2-11.4$\times10^{-6}$ C^{-1} for CIGS layer[119]) or structural change from deposition and forming of $MoSe_2$ intermediate layer[111,212]. Vertical bending of the columnar grains in the Mo layer visible in the TEM images of the co-evaporated films is consistent with the high residual stress in the Mo film. Images of the as-deposited Mo layer without CIGS and Mo layer in the selenized films don't show significant grain bending, which is likely a result of the difference between deposition conditions for selenized and co-evaporated films: Cu and In in the selenized films were sputtered onto the Mo layer at a relatively low temperature of 150 $^{\circ}$C, while for co-evaporated film Cu-In-Ga-Se were deposited onto the film at a higher temperature of 550 $^{\circ}$C, as indicated in Table 3.2. Mo layers in both samples were deposited under the same conditions and at 500 $^{\circ}$C and then cooled down to room temperature at similar rates. Cu-In-

Ga-Se mixture came in contact with the Mo layer at 550 $^\circ$C during the co-evaporation process, and subsequent cooling down to room temperature caused a significant thermal mismatch between the two films, which resulted in the development of misfit strains and greater residual stresses in the co-evaporated CIGS films. This is consistent with the observation of Mo thin film bending only in the co-evaporated films.

Excessive residual stress in the CIGS films will likely adversely affect the film micro-stricture, as evidenced by the voids, delamination and bending of Mo layer as revealed by the SEM and TEM images. This would in turn impact the cell performance by affecting distribution of Se and Na across the film and would also lead to reliability concerns for commercial applications. The current focus of manufacturing CIGS cells is on reducing the thickness of SLG substrate[119] for SLG-based films and using flexible foil/polymer substrates in place of SLG for a wider range of applications. Excessive residual stresses may also lead to premature mechanical failure in devices fabricated on the thinner and flexible substrates. It has also been reported that high residual stresses in the Mo would change the orientation of selenized CIGS film deposited on top of it from the original preferred orientation (112) to (220) / (204) and thus change its crystallinity and affect device performance[206]. One possible solution to alleviate the high residual stress would be to reduce the deposition temperature but it has been reported that decreasing the deposition temperature would have a concomitant adverse effect on grain growth and film quality[98,133]. The residual stress appears to be a trade-off between better film quality and the associated performance improvement, and a more

efficient production process. Further understanding on the origin of the stress is needed in order to develop effective means of reducing the stress level in the films.

3.4.3 Pillar Compression

Elastic properties are important in calculating the effects of temperature and pressure on the structure of chalcopyrite family of semiconductors such as CIGS. Such calculations are of particular importance as CIGS has been shown to go through phase transformation to cubic under high temperature and working pressure[204]. Here mechanical properties of CIGS were obtained from compression experiments on the 500 nm-diameter nanopillars milled from co-evaporated films using focused Ga ion beam. Compared to traditional nanoindentation, nanopillars compression can provide us with more information on the films by screening out the substrate effect[196]. The stress-strain curves with SEM images before and after deformation are shown in Figure 3.7. The modulus was calculated to be 70.4 ± 6.5 GPa based on Equation 3.8, which is close to that obtained from selenized films using Hertzian contact theory. From SEM images of pillars before and after compression (Figure 3.7), two distinct failure modes can be identified. Two out of five pillars failed by shearing near the bottom, while the other three shattered during compression. The stress strain curves are plotted accordingly to these two categories and shown in Figure 3.7 (b,d). Only the loading part is shown as all pillars failed plastically, making it undesirable to try to extract information from the unloading part. All pillars show distinctive compression response for plastic materials

such as large strain bursts. For pillars that failed near the bottom, the stress strain curve show typical brittle plastic failure, with a yield stress of 640.9 ± 13.7 MPa; for pillars that shattered, plastic deformation was observed after yielding happened at 1100.8 ± 77.8 MPa. The largest amount of plastic strain observed was 5%, and the corresponding yield stress is the highest of all pillars, reaching 1165.4 MPa. Non-perfect alignment between pillar and flat punch could result in the pillars shearing near the bottom, and also explain the lower yield stress observed. The significant plastic deformation and hardening and the resulting increase in yield stress observed in some of the tests also suggests CIGS processes some degree of ductility.

3.5 Summary

Micro-structural and mechanical properties of $Cu(In,Ga)Se_2$ thin films deposited on top of molybdenum back contact and soda lime glass substrate by two different techniques: selenization of Cu-In mixture, and co-evaporation, were investigated. We found that selenized films have coarser and irregularly sized grains and suffer from voids and partial delamination from the Mo layer. Their surface roughness is also an order of magnitude higher compared to co-evaporated films. Multiple voids of diameter were observed near the Mo contact in selenized films. The region around these voids are depleted of Se and Na, and would lead to the disparity in device performance between selenized and co-evaporated films. High compressive stress was discovered in the co-evaporated films, which is in

accordance with the bending of Mo layer observed in SEM and TEM images. A reduced

modulus value of 68.9 ± 12.4 GPa was extracted using nanoindentation and Hertzian elastic

contact model for selenized films. Compression of nanopillars 500 nm in diameter milled

from co-evaporated films revealed an elastic modulus value of 70.4 ± 6.5 GPa and show

good agreement with nanoindentation results for selenized films. All pillars show distinctive

response of plastic material, and two failure modes (1) shearing near the bottom of the pillar

and (2) shattering, were observed. Yield stress for sheared pillars was measured as $640.9 \pm$

13.7 MPa, while plastic deformation and hardening was observed in shattered pillars, and a

yield stress of 1100.8 ± 77.8 MPa was measured.

Chapter 4 : Effects on Na Diffusion and Surface Microstructure from TOP:S Passivation of CIGS Thin Films

One key limitation in the performance of CIGS solar cells is surface recombination at the interface between different thin film layers. As a common practice with photovoltaic materials, surface treatment and passivation has been shown in various cases to drastically change surface microstructure, eliminate surface defects, and reduce recombination[213]. The following chapter is adapted from Luo et al[214], and demonstrate that passivating CIS films with Trioctylphosphine Sulfide (TOP:S) solution increases photoluminescence (PL) intensity by a factor of ~30, which suggests that this passivation significantly reduces surface recombination. X-ray photoelectron spectroscopy (XPS) reveals that TOP:S forms both –S and –P bonds on the CIS film surface, which leads to a ~4-fold increase in the surface Na peak intensity. This value is significantly higher than what would be expected from high temperature annealing alone, which has been linked to improvements in surface morphology and device efficiency in CIGS solar cells. We use EDS to measure the solid-state transport of Na within CIS films with and without passivation. EDS spectra on CIS film cross-sections reveals a saddle-shaped Na profile in the as-fabricated films and a concentration gradient towards the film surface in the passivated films, with 20% higher surface Na content

compared with the unpassivated films. We employ hybrid (B3PW91) Density Functional Theory (DFT) to gain insight into energetics of Na defects, which demonstrate a driving force for Na diffusion from bulk towards the surface. DFT Calculations with TOP:S-like molecules on the same surfaces reveal a ~ 1eV lower formation energy for the Na_{Cu} defect. The experiments and computations in this work suggest that TOP:S passivation promotes Na diffusion towards CIS film surfaces and stabilizes sur-face Na defects, which leads to the observed substantial decrease in surface recombination.

4.1 Introduction

One key factor that has been shown to improve the efficiency of compound semiconductor devices like CIGS is passivating the top and bottom film surfaces. These passivation processes, which can take the form of solution, vapor or coating, has been shown to suppress minority carrier recombination near the surface[110,215,216]. An Improved open circuit voltage (V_{oc}) and an efficiency of up to 30% have been reported for Al_2O_3 passivated CIGS thin film solar cells.[215,217]

We demonstrate that passivating the CIS surface with Trioctylphosphine Sulfide (TOP:S) ($SP(C_8H_{17})_3$) provides dramatic improvement in the minority carrier surface recombination. TOP:S has been previously shown to be a viable material for passivating surface flaws in nano-crystals[218], and TOP:S passivation has been reported to protect scribed CIGS thin films from surface and edge defects, which leads to up to 40× enhancement in PL intensity and

~25% improved device efficiency[219]. XPS analysis on passivated CIGS films revealed a greater than 3x increase in the Na peak, which suggests higher Na content in the surfaces of TOP:S-coated films.[219]

Na plays an important role in the operation and performance of CI(G)S solar cells, where incorporating less than 1.0 at.% Na can increase both the V_{oc} and the short circuit current density (J_{sc}) of CI(G)S solar cells by up to 30%, improve device efficiency by up to 20%, govern grain growth during CI(G)S film deposition, and lead to smoother surface morphology[150,153,208,220,221]. It is common for Na to diffuse into the CI(G)S films from the SLG substrate, after which it resides primarily within the grain boundaries. The mechanism for Na incorporation into CI(G)S is not fully understood; reports on Na distribution and its effect in CIS and CIGS films have been inconsistent[112,153,155]. For example, the higher Na concentration at the film surface and at grain boundaries in CIGS revealed by EDS and atom probe tomography measurements has been attributed to grain structure improvements and efficiency enhancement by up to 25%[150,164,222,223]; while other studies using secondary ion mass spectroscopy (SIMS) showed a negligible presence of Na within the CIS films and associated excess surface Na content leading to deteriorating surface morphology.[168]

We combine experiments and theory to explore the effect of TOP:S passivation on CIS thin films and on the incorporation and diffusion of Na within the CIS system. We focus on CIS as a model system in the experiments and in the DFT computational analysis. The similarities

in the microstructure and lattices of CIS and CIGS lead to their nearly-equivalent material properties[98]. Conventional Density Functional Theory is often thought to predict inaccurate band gaps and band offsets for semiconductors such as CIS[224], however we showed previously that using the B3PW91 hybrid functionals predicts a band gap of 1.05 eV for CIS and systematically leads to band offsets within 0.09 eV of experiment[224,225], rendering this type of DFT most useful in studying the surface passivation effects and Na diffusion.

4.2 Method

Sample Preparation: 1200 nm-thick CIS films were deposited at National Nano Device Laboratories (NDL) of Taiwan by the following procedure: (1) 500 nm molybdenum back electrodes were sputtered on soda lime glass substrate by a two-steps process (high working pressure followed by low pressure) at room temperature. (2) Cu and In metal precursors were multi-layered sequentially onto the Mo layer and annealed without Se vapor at annealing temperature of 330 °C. (3) The annealed Cu/In mixture was processed via hydrogen assisted solid Se vapor selenization (HASVS) with $N_2(85\%)/H_2(15\%)$ carrier gas at 550 °C[31,226]. This fabrication method was chosen over other methods that yield higher efficiencies, such as three-stage co-evaporation of CIGS thin films for its better scalability. The total thickness of the CIS absorber layer was measured via SEM to be 1.2 ± 0.1 μm. At this point the finished CIS wafer was cut in half, with one half immersed in TOP:S solution for 24 hours at 120 °C and the other left as-is.

For passivation of CIS thin films, the samples were immersed in TOP:S solution in a glove box (O_2 and H_2O ~200 ppm) for up to 48 hours under different temperatures (RT, 80 °C and 120 °C), followed by a 10 minutes toluene rinse to remove the excess TOP:S.[110]

TEM samples of CIS film cross-sections were created by mechanical polishing followed by low-angle Ar ion milling using Fischione Model 1050 TEM mill. TEM sample thickness was measured in an SEM (FEI VERSA Dual-beam) to be 50 ~ 80 nm.

Experimental: SEM and TEM images are taken in FEI VERSA Dual-beam SEM/FIB and FEI Tecnai TF-30 TEM respectively. Grain sizes were estimated based on the SEM and TEM images in the following manner: (1) multiple lines of the same length were drawn across the image in both horizontal and vertical directions emanating from different, randomly chosen points; (2) number of intersections of the lines with the grain boundaries were recorded; (3) the average grain size is taken to be the total length of the lines divided by the total number of intersections. For PL measurements, the CIS samples were excited by a 671 nm pumping laser and the photoluminescence signal was collected by a monochromator and InGaAs photodetector connected to a lock-in amplifier. XPS measurements were conducted with a Kratos surface-science instrument and an Al Kα (1486.7 eV) x-ray source under high vacuum (1×10^{-9} torr). The ionization potential of CIS thin films under air was measured by a photoelectron spectrometer (AC-2, Riken Keiki). EDS analysis was conducted using FEI Tecnai TF-30 transmission electron microscope in scanning transmission electron

microscopy (STEM) mode, using an acceleration voltage of 300 kV and live acquiring time of 300 seconds for each measurement. Quantitative atomic percentage (at.%) analysis was carried out using Oxford INCA Energy EDS X-ray Microanalysis System. Density of CIS films was taken as stoichiometric $CuInSe_2$ as 5.77g/cm.[227] Five measurements were taken at each location: one measurement from a rectangular area of~70nm $\times$ 70 nm, followed by point measurements at the four corners of the rectangle. The size of the measured area is chosen to minimize the effect of local inhomogeneity such as grain boundaries.

Computations: The DFT calculations used the hybrid functional B3PW91[228] that have been shown by Hai et al to provides accurate bandgaps[224] and band offsets[225] (average mean error of 0.09 eV) for chalcopyrite semiconductors. Thus B3PW91 leads to a band gap of 1.05 eV for CIS compared to 1.04 eV from experiment and < 1 eV from typical DFT methods (Perdew-Burke-Ernzerhof, PBE).[224] To Accurately represent the small Na contents, we used periodic unit cells with 64 atoms. Hybrid B3PW91 calculations are not practical for DFT codes (such as VASP and Quantum Expresso) that use standard plane wave basis sets (1000s of times slower than PBE). Consequently we use local atomic Gaussian-type basis sets that enables fast evaluation of the Hartree-Fock exchange terms.[229] As implemented in the CRYSTAL09[229] software package, B3PW91 is only 1.7 times the cost of PBE, while about 2 orders of magnitudes faster than PBE in VASP.[224]

Optimized Cu, In, Se and Na basis sets and pseudopotentials were taken from our previous work[225]. For each system we relaxed the structure until the forces on each atom dropped below 4.5×10^{-4} Hartree/Bohr. For Cu, In and Se, we used the SBKJ relativistic angular momentum projected effective core potentials[230,231] and associated basis set[232], while for Na atoms and the $SP(CH_3)_3$ molecule we used a complete all-electron basis set. Following Xiao et al.[225], we did not include Spin-orbit Coupling (SOC) since all the systems considered here are closed-shell (no unpaired spins). We used an extra-large k space grid to ensure accurate integration, and we used the Γ-centered Monkhorst-Pack scheme[233] to sample reciprocal space with a resolution of $\sim 2\pi \times 1/40 \text{ Å}^{-1}$.

We kept the number of Se atoms per periodic cell constant at 32 for all bulk ($CuInSe_2$) and surface ($CuInSe_2$ and $Cu_5In_9Se_{16}$) calculations.

For surface calculations, free surfaces of $CuInSe_2$ and $Cu_5In_9Se_{16}$ were cleaved from respective bulk unit cells and relaxed prior to introduction of Na defects.

Calculations with $SP(CH_3)_3$ molecules were started by placing the molecule at 2 Å above the free surface with S atom adjacent to the Cu substitution site, and S=P bond parallel to the surface normal. The system was then fully relaxed before the atom on the Cu site was replaced with Na, at which point the system was allowed to relax again.

4.3 Results

4.3.1 Surface Measurements of TOP:S Passivated CIS Films

Figure 4.1 shows the PL intensity of CIS films with different passivation times (Figure 4.1(a)) and different passivation temperatures (Figure 4.1(b)), each normalized by the PL intensity of as-fabricated films. All PL peaks were found to be at ~0.96 eV without any obvious spectral shifts. For the passivation temperature of 120 °C, the normalized intensity increased with passivation time and peaked after 24 hours at ~29 times higher than the baseline. The intensity remained relatively the same for longer passivation times, reaching a 32.7 times increase over the baseline after 48 hours. For the fixed passivation time of 24 hours, varying the passivation temperature from room temperature (RT) to 80°C and 120°C led to factors of 2.5, 6.2, and 29 times enhancements in PL intensity respectively, which demonstrates that PL response is a strong function of solution treatment temperature.
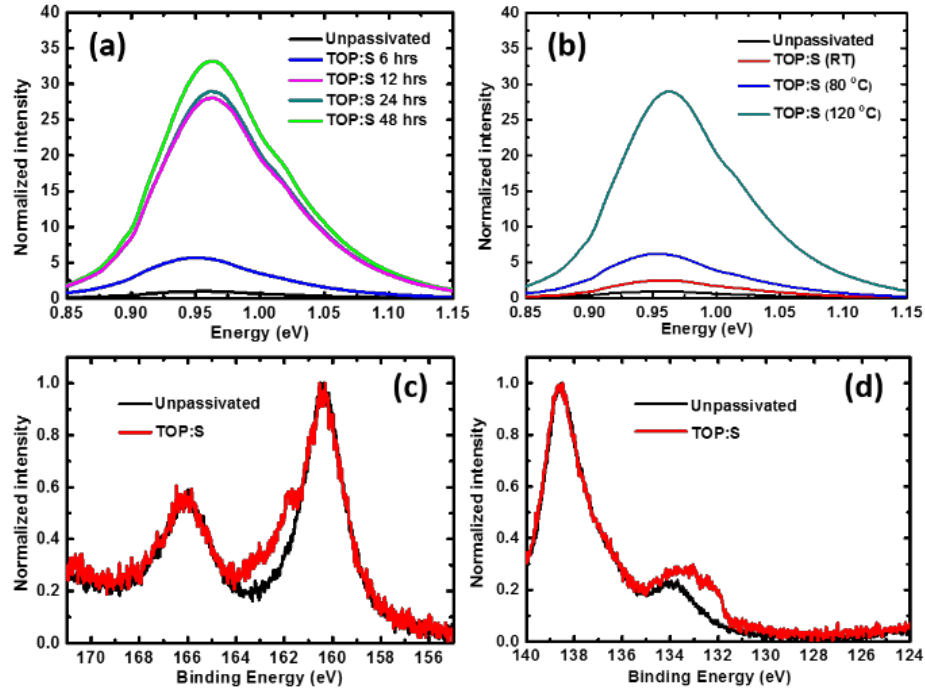
Figure 4.1 XPS and PL measurements on CIS films before and after TOP:S passivation. (a) Normalized PL intensity for unpassivated (baseline) CIS films, and films with passivation times up to 48 hours. (b) Normalized PL intensity for unpassivated (baseline) CIS films, and films for passivation temperature up to 120 °C. (c,d) Surface XPS spectra of (c) S 2s and (d) P 2p peaks for CIS thin films with (red) and without (black) TOP:S treatment (120 °C, 24 hours)

XPS measurements were conducted on CIS films with and without the TOP:S passivation at room temperature to understand the binding state of TOP:S on passivated film surfaces. Figure 4.1(c) shows the XPS peaks of S $2p$ (161.8 eV) , Se $3p_{1/2}$ (166.1 eV), and $3p_{3/2}$ (160.5 eV); Figure 4.1(d) shows the XPS peak of P $2p_{3/2}$ (133.1 eV) and the Auger peak of Se. These

spectra reveal the emergence of a small S $2p$ peak after passivation, which indicates that the sulfur from TOP:S binds to the film surface, presumably by forming Cu_2S and In_2S_3. Figure 4.1(d) shows an increase in the P $2p$ peak as a result of the P atom in the TOP ligand interacting with dangling bonds on the film surface. In contrast to the increases in PL intensity, the increases in the intensity of S and P XPS peaks were independent of TOP:S passivation temperature, as shown in Figure 4.2, which suggests that binding of TOP:S molecules to the film surface did not cause the increase in PL.
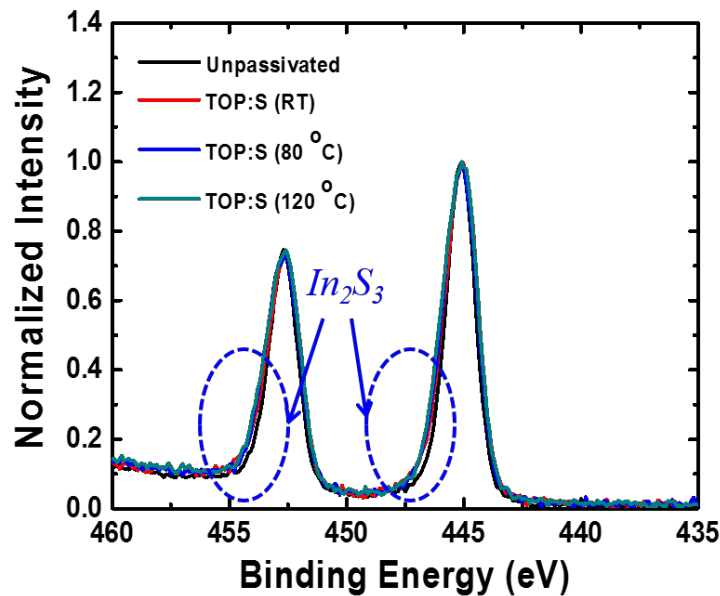
Figure 4.2 XPS measurements showing the formation of In_2S_3 after TOP:S passivation. XPS spectra of In $3d$ without and with TOP:S treatment for 24 hours under different temperatures (RT, 80 °C, and

120 $^{\circ}$C), showing the binding of TOP:S to CIS surfaces is invariant
of temperature

Figure 4.3(a) shows surface XPS measurements of the Na *1s* peak (1074 eV) intensity of the

samples that were passivated for different durations, normalized by intensity of as-fabricated

films. It shows a ~4.5x increase in the Na *1s* peak intensity for samples that were passivated

in TOP:S solution for 24 and 48 hours, which indicates a significantly higher surface Na

content in passivated films. This correlates well with the observed increase in the PL peak

intensity over the same passivation times; with the system reaching full saturation after 24

hours (Figure 4.1(a)). Varying the processing temperatures of the TOP:S treatment for the

fixed time of 24 hours led to a monotonic increase in the same Na peak, which also correlates

with the trends in PL enhancement (Figure 4.1(b)). We treated some of the samples with

TOP:S and trioctylphosphine (TOP) at 120 °C for 24 hours in addition to annealing in Se

free atmosphere at 600 °C for 12 hours to determine whether the surface Na content increase

might have been caused solely by the high-temperature annealing of the film on the SLG

substrate. The 600 °C annealing temperature mimic typical high temperature selenization

processes and was selected to amplify potential temperature effect on surface Na content, as

no noticeable change was observed in reference samples annealed at 120 °C. Figure 4.3(c)

shows that the ~2.5x- and 3.5x-higher Na concentration in the TOP and TOP:S-treated

samples was significantly higher than that in the annealed samples, ~1.3x. It has been

proposed that Na concentration at CIS surface leads to shifts in surface energy levels. Figure

4.3(d) shows a schematic of this mechanism, in which Na congregates at CIS film surface in TOP:S solution and lead to a change in surface ionization potential.
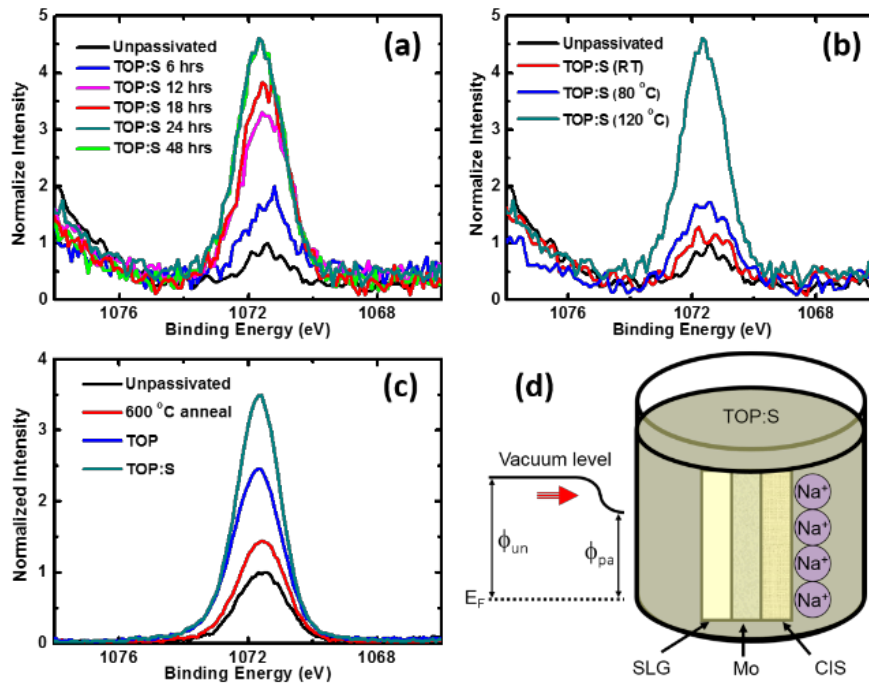
Figure 4.3 XPS measurements before and after TOP:S passivation showing the increase in surface Na content. Surface XPS spectra of Na *1s* peak for unpassivated CIS film (baseline) and (a) films with passivation times up to 48 hours, (b) films with passivation temperatures up to 120 °C, and (c) SLG substrates treated with TOP and TOP:S at 120 °C for 24 hours and annealed at 600 °C for 12 hours. (d) Schematic of increased surface Na concentration from TOP:S passivation, and the alteration of energy levels

4.3.2 Analysis of Through-thickness Na Concentration Profile

Figure 4.4 shows two scanning transmission electron microscopy (STEM) images of (a) as-fabricated and (b) passivated CIS films overlaid with quantitative EDS measurements of Na content at each location. These images show that the TOP:S passivation did not introduce visible changes to surface morphology of the films. Parts of the passivated film (Figure 4.4(b)) near the surface delaminated and adhered to the epoxy layer applied during TEM sample preparation. This is likely a result of residual stress introduced into the underlying film by the passivation process, a common side effect of thin film passivation[110]. The STEM images show a non-uniform grain size distribution in both films; bright field TEM analysis revealed that the grain size in both films ranged from 50 to 800 nm, with an average of 305 nm and a standard deviation of 210 nm. Multiple voids were observed in both films at a distance of ~100 nm above the Mo layer, consistent with previous work on a similar material system.[191] EDS analysis indicates that the average surface content of Na increased from 0.99±0.20 at.% in the as-fabricated films to 1.11±0.11 at.% in the passivated films. These concentrations are consistent with reports on atomic probe tomography measurements of Na at grain boundaries within CIS films[222,223], and are higher than some previously reported surface measurements[112,153]. This discrepancy can be attributed to the limited resolution of most surface techniques like EDS and secondary ion mass spectrometry (SIMS), and the high temperature deposition steps such as the selenization process at 550 °C and the annealing process at 330 °C, which have been shown to increase surface concentration of Na.[31] We

found a distinct concentration gradient present in passivated films, with Na content of 0.41±0.09 at.% at the Mo/CIS film interface and 1.11±0.11 at.% at the surface of the film. In the as-fabricated films (Figure 4.4(a)), the Na content of the film is higher at (0.78±0.10 at.%) near the Mo interface, then decreases to 0.20±0.06 at.% midway through the film, and increases to 0.99±0.20 at.% at the film surface. EDS area maps of Cu, In, Na and Se for passivated and as-fabricated films can be found in Figure 4.5 and 4.6. The low overall concentration of Na and the increased background noise from large area map measurements render these concentration profile maps less useful for quantitative analysis compared to point measurements.
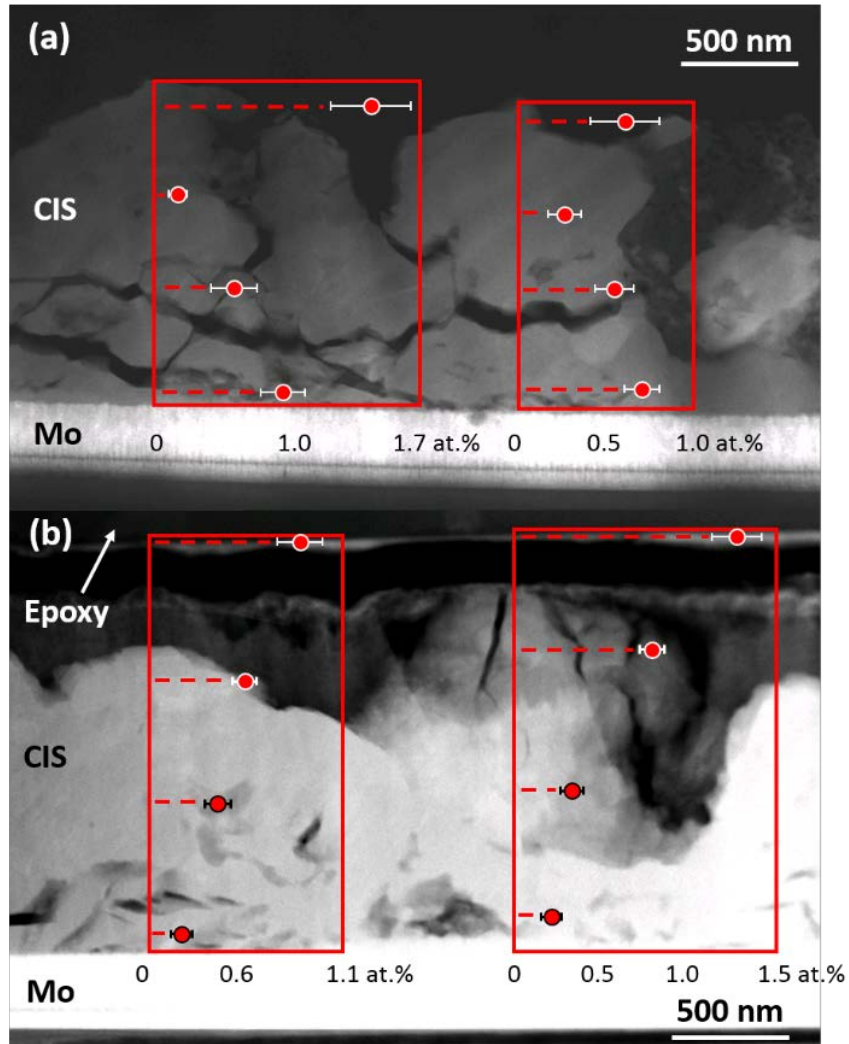
Figure 4.4 Na concentration profile in TOP:S passivated and as-fabricated CIS films. Representative cross-sectional STEM images with Na concentration profiles overlaid over the images for (a) as-fabricated and (b) TOP:S passivated CIS films. The intercepts between the dashed lines with boxed regions show the actual location of the measurements. The x-axis shows the average Na content (at.%) based on 5 different measurements at each location
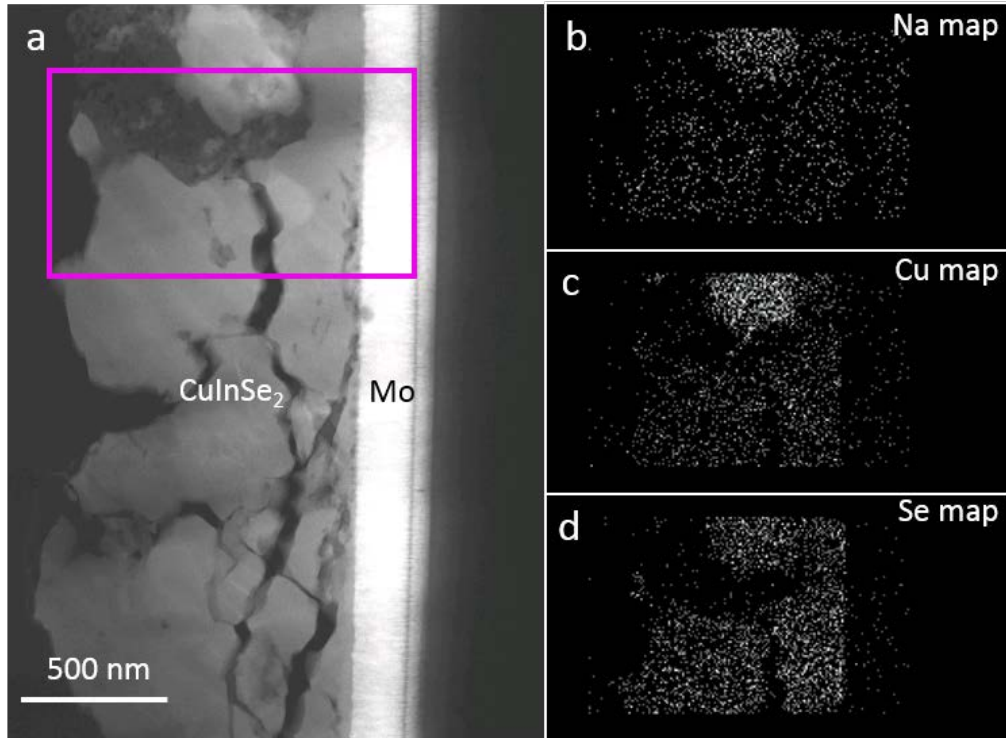
Figure 4.5 Species concentration in as-fabricated CIS films. (a) Representative STEM image of as-fabricated CIS film. Highlighted region shows the area used for concentration mapping. (b,c,d) Concentration maps for Na, Cu and Se measured in region highlighted in (a)
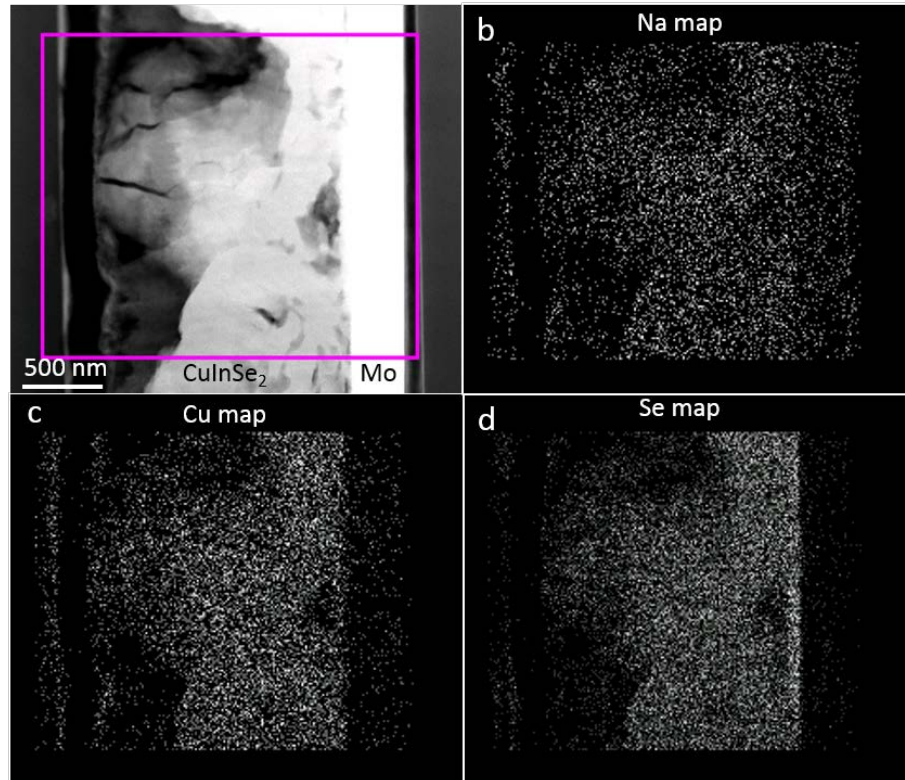
Figure 4.6 Species concentration in passivated CIS films (a) Representative STEM image of passivated CIS film. Highlighted region shows the area used for concentration mapping. (b,c,d) Concentration maps for Na, Cu and Se measured in region highlighted in (a)

4.3.3 Energetics of Na Defect Formation in Bulk CIS

We conducted DFT calculations to investigate the energetics of Na defects in CIS films. Figure 4.7(a) shows a schematic of 4 different types of Na defects in bulk CIS analyzed: (1) substitutional Na on a Cu lattice site (Na_{Cu}), (2) substitutional Na on an In lattice site (Na_{In}),

(3) Na in a tetrahedral interstitial site within the CIS lattice (Na_{tet}), and (4) Na in an octahedral interstitial site within the CIS lattice (Na_{oct}). In the simulations, a single Na atom was introduced into a 64-atom $CuInSe_2$ unit cell, which corresponds to a Na defect density of 1.3 at.%, a magnitude similar to the surface concentration measured by EDS. All calculations in bulk CIS crystals are performed in stoichiometric $CuInSe_2$ systems. We did not consider Na-Na "dumbbells", where two Na atoms reside on the same lattice site, in these simulations because their formation energy at various sites has been reported to follow the same trend as their single-atom counterparts.[157]
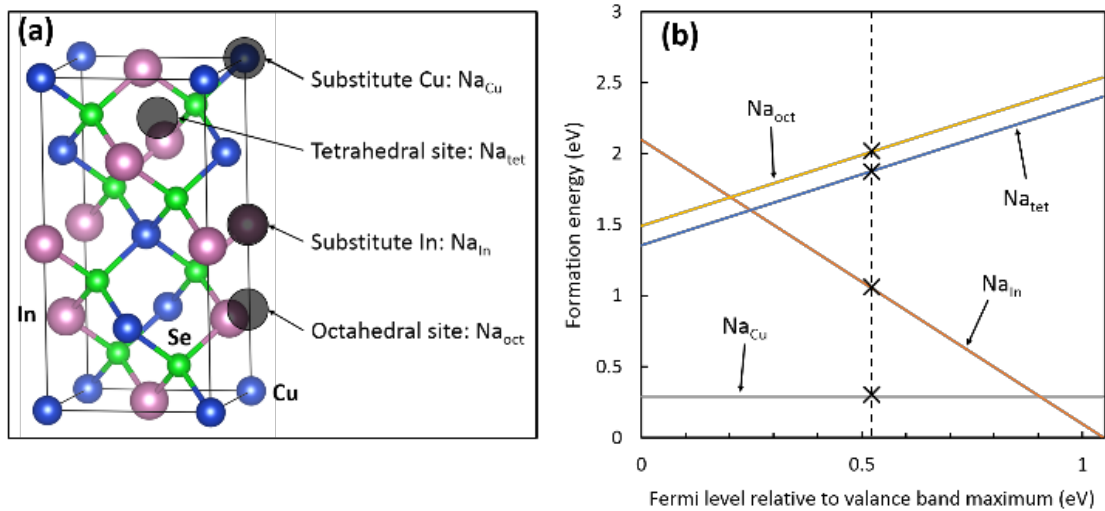
Figure 4.7 DFT model and results of Na defects in bulk CIS. (a): Schematic showing various Na defects in the CIS unit cell, Na atoms are shown in black, Cu in blue, In in red, and Se in green. (b): Formation energy (eV) of various Na defects as a function of Fermi energy (eV) relative to VBM. Intercepts with the dashed line marks formation energies at intrinsic Fermi level

We represent and compute the total defect formation energy E_F by:

$$E_F = E_{defect} - E_{bulk} \pm \sum \bar{n}_i \mu_i + q E_{Fermi} \qquad (4.1)$$

where E_{bulk} is the total energy of the bulk unit cell, E_{defect} is the total energy of the unit cell that contains the specific defect, μ_i and $\bar{n}_i$ are the chemical potential and the concentration of species i, q is the defect charge state derived from the differences in charge states for individual species (+1 for Cu and Na, +3 for In), and E_{Fermi} is the system Fermi level relative to the valence band maximum (VBM). We calculated the product $\bar{n}_i \mu_i$ for Cu and In as the energy of removing one Cu or In atom from the bulk unit cell, respectively. This product, $\bar{n}_i \mu_i$ for Na as a point defect in the CIS system is not as readily available because Na is extrinsic to the system. Previously, Wei et al. and Oikkonen et al.[157,221] approximated this potential by extrapolating the potential for bulk body-centered cubic (BCC) Na and Na-In-Se compounds. We chose not to use this approach because it is not able to capture the changes in the Na potential with respect to Cu content, which is critical to our investigation of Na_{Cu} defects. Instead, we calculated the total energy of different CIS systems with variable Na contents, where Na atoms were introduced into the systems as Na_{Cu} substitution. We investigated CIS systems with varying unit cell sizes: (1) 32-atoms, (2) 64 atoms, (3) 128 atoms, and (4) 256 atoms; in each case 1 Cu atom on the lattice was replaced with a Na atom.

The systems were relaxed in similar a fashion to the bulk calculations detailed above. The $\bar{n}_{Na}\mu_{Na}$ term in Equation. 4.1 that represents the energy difference of Na_{Cu} substitution defect at various Na concentrations can now be extrapolated from the plot of total system energy vs. Na-Cu substitution content in shown in Figure 4.8. It is reasonable to assume that within the same concentration range for Na, its potential in a Cu-lattice site is comparable to that in an In-lattice or in an interstitial site. The difference in energy for other forms of Na point defects can be obtained by modifying the energy difference for Na_{Cu} with chemical potentials of Cu and In in CIS system.
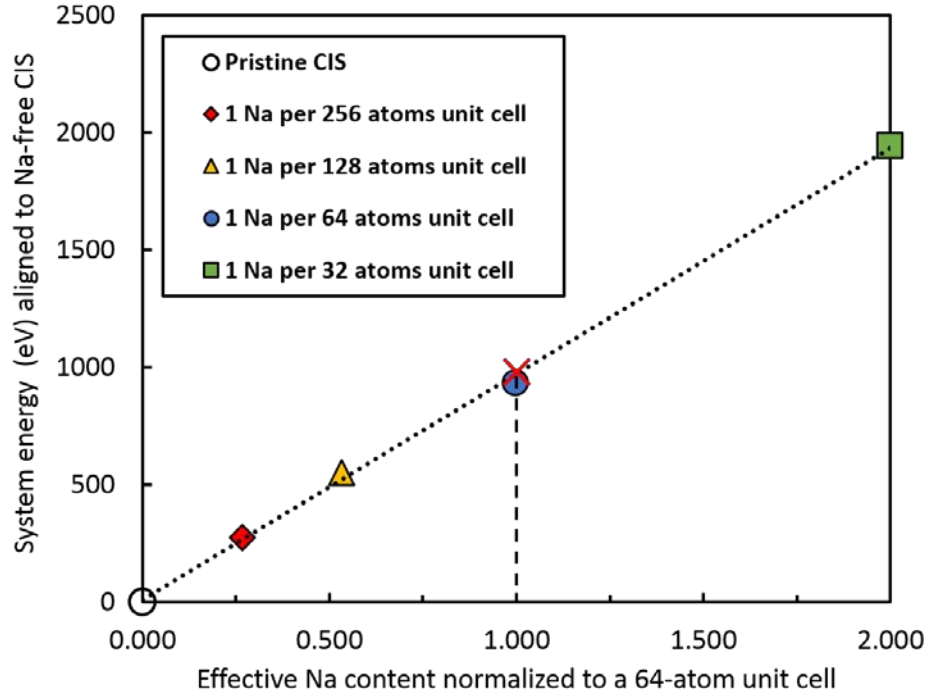
Figure 4.8 Total energy for systems with various levels of Na_{Cu} substitution, aligned to pristine CIS. The Dotted line shows a linear fit of total energy vs. number of Na atoms per 64-atoms unit cell. The Cross with a dashed line represents the energy change due to one NaCu substitution in a CIS unit cell with 64 atoms

To account for different doping conditions in CIS films, the Fermi level of the system was allowed to vary across the calculated bandgap of 1.05 eV[225], which is consistent with experiments[234,235] and simulations[157,236]. The calculated bandgap value is used here to benchmark against previous calculations such as Oikkonen et al who reported Na_{Cu} formation energy ~-1eV, because absolute values for formation energy often significantly

depend on alignment of system Fermi level, whereas system bandgap is a better representation of accuracy of calculation. Defect formation energies as a function of Fermi level are plotted in Figure 4.7(b), where the intercepts with the solid vertical line marks the mid-bandgap formation energy (0.52 eV from VBM). These results indicate that Na at a Cu lattice site, $Na_{Cu,}$ has the lowest formation energy among all the defects types considered under most doping conditions; Na at an In lattice site, $Na_{In,}$ becomes favorable under extreme n-type doping, where the Fermi level shifts to 0.9 eV above VBM.

4.3.4 Calculation of Na_{Cu} Energetics at the Film Surface

We used DFT to calculate the formation energies of Na defects in the CIS film surfaces. It has been reported that CIS surfaces could facet into polar [112] orientations from the non-polar [110] orientation to minimize the surface free energy[237]. This is consistent with experimental observations of faceted surfaces in CIS and CIGS films in our previous work[191]. Surface Cu content has significant effect on device performance of CIS thin film solar cells. An artificial Cu-deficient surface condition is often enforced as it has been reported to improve device efficiency and open circuit voltage by up to 25%[31,98]; while a higher surface Cu content has also been shown to reduce surface defect and improve uniformity[238,239]. Here we investigated surfaces with both stoichiometric and deficient Cu content. Similar to our previous DFT studies on CIGS[225], we simulated the Cu-deficient condition with the $Cu_5In_9Se_{16}$ unit cells (Cu content 17 at.%, designated by Cu-poor) obtained by removing

some of the Cu atoms from the stoichiometric $Cu_1In_1Se_2$ unit cells (Cu content 25 at.%, designated by Cu-rich) and inserting additional In atoms in their place if needed to balance the charge, while maintaining the total number of Se atoms constant. We constructed all unit cells consistent with these compositions and chose the geometry with the lowest DFT energy as the optimal structure. We considered Cu rich and Cu-poor conditions for both surface orientations, a total of 4 cases: (1) Cu-rich (110), (2) Cu-rich (112), (3) Cu-poor (110) and (4) Cu-poor (112). Our calculations demonstrate that of all possible defect occupancy sites, the sodium-copper substitution, Na_{Cu} is the most energetically favorable defect in bulk CIS (Figure 4.7(b)). We postulate that it is also the preferred type of defect at the CIS surface because the vicinity of the free surface is unlikely to change the electron configuration of substitutional point defects in the case of Na_{Cu} and sodium-indium substitution Na_{In}[225], while interstitial Na defects are significantly higher in formation energy compared to substitutional cases. Based on these findings, we restrict surface calculations to Na_{Cu} only; and the defect charge state q in Equation. 4.1 becomes 0 because Na and Cu are monovalent, and the term qE_{Fermi} vanishes.

To investigate the interactions between TOP:S passivation and the surface Na defects, we conducted additional DFT simulations: (1) A small organic molecule $SP(CH_3)_3$, used to represent the TOP:S, was placed on top of the cleaved CIS surfaces with various Cu contents and orientations (Figure 4.9). The sulfur-phosphorus double bonds (S=P) in the $SP(CH_3)_3$ molecules were aligned along the surface normal, with the S atom adjacent to the surface.

The molecule was placed 2 Å away from a Cu atom closest to the surface. The model molecule, $SP(CH_3)_3$, has shorter carbon chains than TOP:S ($SP(C_8H_{17})_3$), the additional carbon atoms in TOP:S have a negligible effect on the electron distribution of S and P atoms, and it is unlikely that the carbon chains interact directly with the CIS surface. It is reasonable to consider $SP(CH_3)_3$ and TOP:S as equivalent in their effects on surface defect energetics and will be referred to them interchangeably from now on. (2) The system was then fully relaxed, and some of the Cu atoms were replaced with Na to form the Na_{Cu} substitution. (3) The Na-containing, "passivated" films were then fully relaxed using DFT similar to bulk calculations, and the formation energy of Na_{Cu} was calculated using Equation. 4.1. Figure 4.10 shows a schematic for calculating the formation energy of Na_{Cu} in the presence of $SP(CH_3)_3$ for stoichiometric (110)-oriented CIS films.
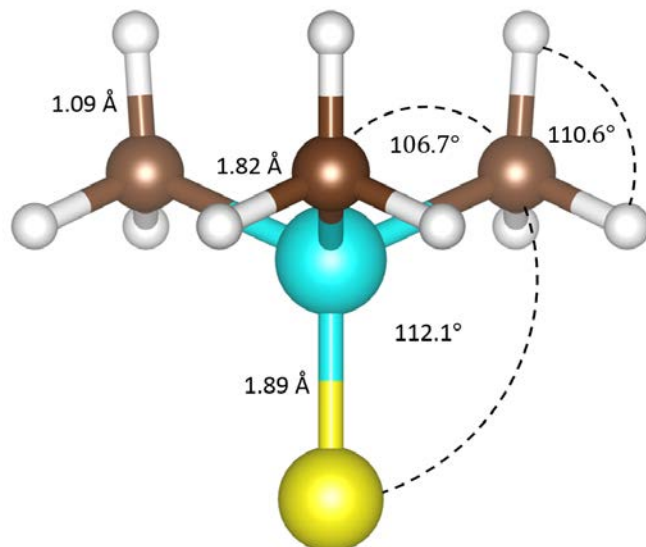
Figure 4.9 Optimized structure of the SP(CH$_3$)$_3$ molecule used in DFT calculations to simulate the effect of TOP:S passivation on film surface. S atom is shown in yellow, P in cyan, C in brown, and H in white
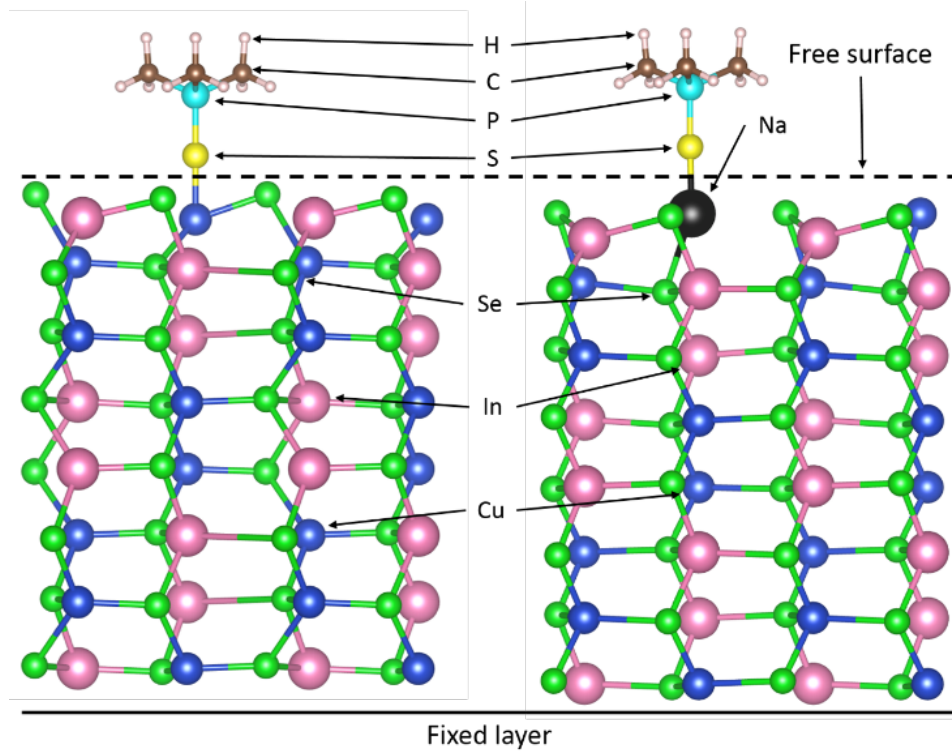
Figure 4.10 The effect of Na substitution on optimized geometry of CIS free surface. Left: Optimized CIS unit cell with one $SP(CH_3)_3$ placed on top. Cu atoms are shown in blue, In in red, Se in green, S in yellow, P in cyan, C in brown, and H in white. Right: Optimized CIS unit cell with one Na_{Cu} substitution and one $SP(CH_3)_3$ placed on top of the Na atom. The Na atom is shown in black. In both schematics dashed line shows the direction of the free surface, and the solid line shows the direction of fixed atomic layer

Figure 4.11 shows the formation energies of Na_{Cu} for each of the 4 surface cases, with and without passivation. This plot reveals that the formation energies of all unpassivated surfaces (blue bar) are lower (more stable) compared to those energies in the bulk, with distinct

differences among different surface conditions. Cu-poor (110) surfaces have the lowest (most favorable) formation energy at -0.05 eV, compared to 0.29 eV in the bulk. A comparison with passivated surfaces (red bar) reveals that the formation energies decrease for all surface configurations after passivation. Here significant decreases up to ~1 eV were reached for Cu-rich (110) and Cu-poor (112) cases. In all cases, the surface formation energies of Na_{Cu} are lower compared to those in the bulk, suggesting the presence of a driving force for Na diffusion towards film surfaces, which is further enhanced by TOP:S passivation. Figure 4.12 shows the atomic-level configurations of the Na defect within each CIS film surface studied, as well as the passivation molecule after surface relaxation.
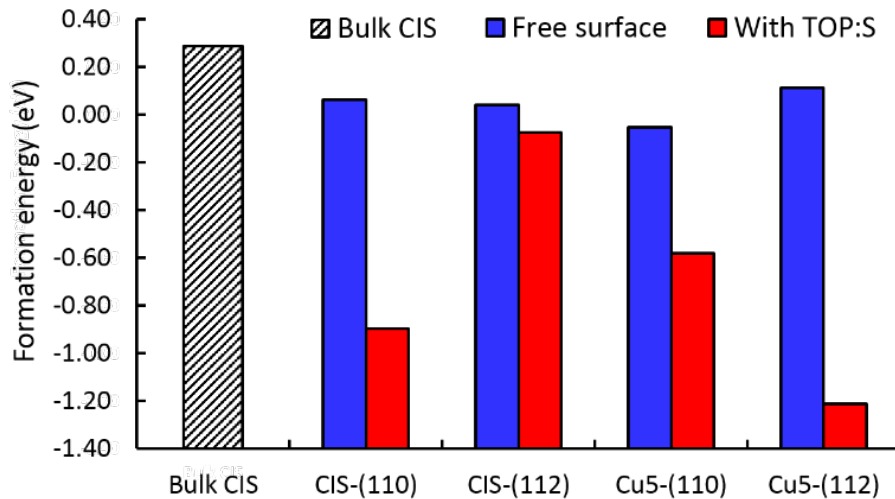
Figure 4.11 Formation energy of Na_{Cu} at film surfaces with and without TOP:S. Shaded: Formation energy (eV) of Na_{Cu} substitution in bulk CIS taken from Figure 3(c). Blue: Formation energy (eV) of Na_{Cu} substitution on different surfaces (Cu-poor

$Cu_5In_9Se_{16}$, Cu-rich $Cu_1In_1Se_2$, (110) and (112) orientations). Red: Formation energy (eV) of Na_{Cu} substitution on the same surfaces with one $SP(CH_3)_3$ placed on top
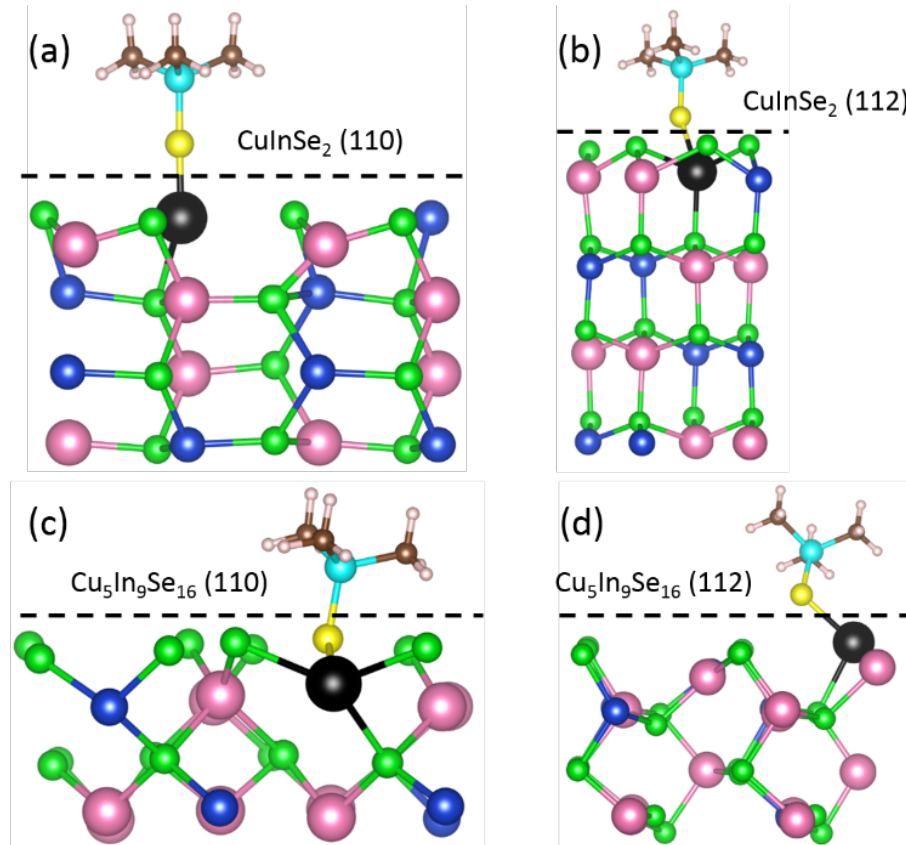
Figure 4.12 Optimized surface geometry with $SP(CH_3)_3$ molecule. (a): Cu-rich (110), (b): Cu-rich (112), (c): Cu-poor (110) and (d): Cu-poor (112). Each case show parts of the surfaces containing the Na_{Cu} substitution. Color scheme follows that of Figure 4.9. Dashed lines show direction of the free surface

4.4 Discussion

4.4.1 Na Distribution in the Presence of TOP:S Passivation

Surface passivation in semiconductors is commonly used to eliminate surface defects and flaws, such as vacancies and interstitials, which is often manifested by higher carrier density and surface PL intensity[215,217,219,240]. Figure 4.1(a) shows that the PL intensity increases by ~29 times with passivation time up to 24 hours and remains relatively constant with longer passivation duration, which suggests that the surface is fully saturated with the TOP:S molecule. Such an increase is in accordance to previous reports on passivation of CI(G)S samples from similar deposition conditions[219], and can be attributed to the relatively poor surface uniformity and morphology of the CIS samples tested. It shows that the TOP:S solution treatment passivates the existing surface defects and leads to a reduction in surface recombination, reaching full saturation after 24 hours. Figure 4.1(b) shows that the enhancement in PL increases monotonically with higher treatment temperatures, which suggests that the passivation effect may involve a temperature-limiting process, such as solid-state diffusion[110]. XPS surface analysis of the same samples (Figure 4.1(c), 4.1(d)) reveals higher S and P peaks on the film surfaces, likely caused by the formation of Cu_2S and In_2S_3 and the interaction between the phosphorus atoms and dangling bonds near the film surface. Additional measurements at various passivation temperatures reveal that these peaks and the binding state of TOP:S on film surfaces are independent of passivation

temperature (Figure 4.2), which implies that the adsorption of TOP:S is not temperature-limited and is unlikely to fully account for the increase in PL response after passivation.

XPS measurements of surface Na *1s* peak follow trends similar to the PL response after TOP:S passivation. Figure 4.3(a) shows a ~4.5 times increase in the passivated films compared with the as-fabricated ones after immersion in the TOP:S solution for 24 hours, which remained relatively unchanged for longer passivation duration. Changes in the Na peaks appear to depend on the passivation temperature, with the enhancement from passivation at 120 °C over twice than that from passivation at RT (Figure 4.3(b)). Those films that underwent only high-temperature annealing also show increased surface Na content (Figure 4.3(c)), similar to existing literature reports[168,169]. However, the improvement in Na content from the TOP/TOP:S passivation is over twice compared to just from high temperature annealing, and much higher than reference samples annealed at 120 °C which showed no change in Na content. Films passivated by TOP:S exhibit a higher Na peak compared to the TOP-passivated ones, which can be attributed to the formation of Na_2S, an energetically favorable species that is most notably known to passivate GaAs semiconductor devices[109,241]. Formation of Na_2S would also release the ligands within the TOP, which can in turn adhere to the surface via P bonds (Figure 4.1(d)) to serve as a protective surface layer. This layer can be easily removed by solution rinsing before the deposition of additional layers during solar cell device fabrication[110,219].

Figures 4.1 and 4.3 show that the PL and the XPS Na peak of CIS films follow similar trends after TOP:S passivation; both increasing monotonically with passivation temperature and passivation time, which for the latter reaches full saturation after 24 hours of solution treatment. This suggests that the increase in surface Na content after passivation may contribute to the increased PL response. It has been suggested that Na can create surface dipole on CI(G)S thin films, which will lead to formation of depletion regions and changes in energy levels[217,242]; while recent work using scanning tunneling spectroscopy (STS) showed negative surface dipoles that are independent of surface Na content and attribute the depletion region formation to surface reconstruction[238], though it is generally accepted that increased alkali metal content can significantly alter CIS film surfaces. Our previous DFT calculations show high Na (and K) concentration at CIS film surface leads to energy level shifts[225], here we observed a decrease in the Fermi level of CIS surfaces relative to vacuum from 5.17 to 4.69 eV by measuring the ionization potential of the CIS films that were passivated at 120 °C for 24 hours and the as-fabricated ones using a photoelectron spectrometer, shown in Figure 4.13. Such shifts in energy levels serves to reduce surface recombination and to increase PL intensity, which would also closely follow the increase in surface Na content, as shown in Figure 4.3.
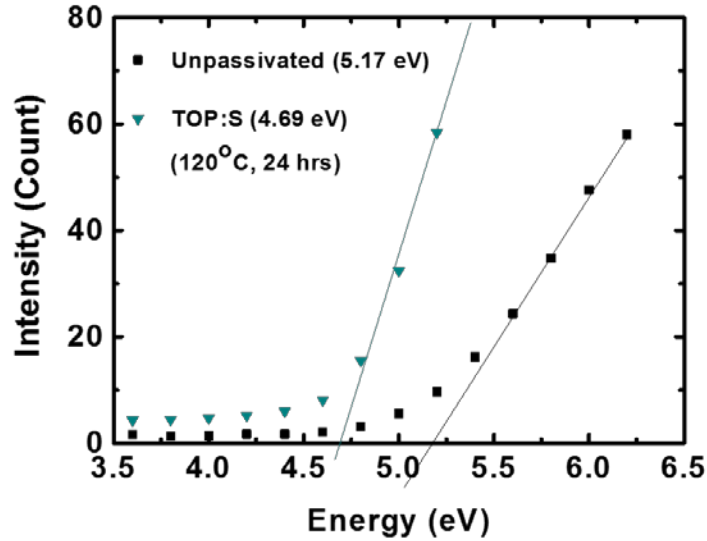
Figure 4.13 Ionization potential via low-energy photoelectron spectra of CIS surface before and after TOP:S (120 $^{\circ}$C, 24 hours) treatment

We propose two potential mechanisms to explain the greater surface concentrations of Na observed in the CIS films: (1) Na within the SLG substrate is dissolved in the TOP:S solution, after which it diffuses in the liquid state to re-deposit onto the film surface; or (2) the TOP:S passivation layer on the film surface provides the driving force for solid state diffusion of Na from the SLG substrate towards film surface. EDS analysis performed on a representative cross-section of each CIS film, shown in Figure 4.4, reveals a "saddle-shaped" Na distribution in the as-fabricated films, and a close to linear bottom-to-top concentration gradient in the passivated films. Each measurement spanned an area of∼70nm × 70 nm,

which is sufficiently large to represent the characteristics of each film, whose morphology is inhomogeneous and has been shown to cause significant variances in localized spectroscopy measurements[153,165]. The overall increase in the surface Na content measured by EDS is ~20%, a substantially lower relative increase than the ~4x increase in XPS measurements. This is likely caused by the fabrication process of TEM samples, which exposes part of the surface Na in the Na_2S form to the atmospheric moisture and removes it. The STEM probe can provide information on the Na distribution along the film thickness that cannot be obtained via surface measurements. The STEM-generated Na concentration profiles before and after passivation are shown in Figure 4.4, their difference can be explained by the non-ideal film morphology as a function of film height. We propose that during the high temperature selenization process (550 °C), the Na enters the CIS films from SLG substrate and migrates towards the film surface via solid-state diffusion, which is impeded by the voids observed in all CIS films ~200 nm above the Mo layer, as shown in the STEM images in Figure 4.4 and in our previous work[191]. It is likely that the transport of Na atoms through the pore-containing region is relatively sluggish and increases back to its original value in the more homogeneous portions of the film. As a result, the Na content is lower in the vicinity of the voids and, possibly, near other microstructural defects within the film. At equilibrium, all Na atoms entering the system are able to diffuse to the surface and through the void regions, which would set up a concentration gradient towards the surface, as shown in Figure 4.4(b). The distinct change in the Na distribution profile after passivation supports the

hypothesis that TOP:S passivation promotes Na diffusion towards film surface. XPS measurements on passivated films revealed a higher surface Na content (Figure 4.3) compared to EDS, it is possible that the diffusion of Na from SLG substrate through TOP:S solution to the film surface also contributes to the increased surface Na concentration. The EDS measurements imply that solution-based Na, potentially in the form if Na_2S, can be easily removed from the film surface before the deposition of additional layers, which could be helpful since excessive Na has been shown to have a detrimental effect on device performance.[155,164]

Altering surface properties via passivation has been shown to have significant impact on the diffusion in CI(G)S thin films[243,244]. Na has high affinity for TOP[245] and easily forms Na_2S[219] by binding with the active sulfur atom in TOP:S, the presence of the TOP:S passivation would likely enhance Na diffusion towards the film surface, providing an additional driving force for the solid state diffusion. During device fabrication, a CdS buffer layer is commonly deposited onto the CIS top surface. Our previous DFT studies showed that Na decreases conduction band offset (CBO) near the contact between CIS and CdS[225], and a higher Na content at the CIS surfaces would reduce the electron transport barrier across the interface. This could lead to better efficiency and improved V_{oc} of devices containing TOP:S passivated CI(G)S films.[140,221]

4.4.2 Formation Energy of Na in Bulk CIS

We performed additional DFT calculations to investigate the effect of TOP:S on solid-state diffusion of Na along CIS film height. We considered the formation energy of different types of Na point defects in bulk CIS. The lower formation energy and greater stability of Na_{Cu} compared to other Na point defects shown in Figure 4.7 agrees with previous calculations on CIS[157,225] and Cu-deficient $CuIn_5Se_8$ systems[149,160], which suggests that at equilibrium Na prefers to occupy Cu lattice sites in bulk CIS. This is corroborated by the experimental observations that the enhancement in CIS device performance from Na is more pronounced in Cu-poor CIS films[164,210]. The charge neutrality of Na_{Cu} formation leads to its insensitivity to the Fermi level. It has been suggested that the charge neutral Na_{Cu} does not introduce deep sites into the bandgap nor facilitates any other major alterations of the band structure[157]. Indeed this is what we find in our previous DFT studies, that it is more likely that populating the Na into Cu lattice sites will change the intrinsic defect mobility[157] while decreasing the CBO near the CIS-CdS interface.[225]

4.4.3 Effects of Surface Condition on Formation Energy of Na_{Cu}

We determined the intrinsic diffusion pathways along CIS film height by calculating the formation energies of Na defects at the film surface. Figure 4.11 shows that for each of the 4 types of surfaces, the formation energy for Na_{Cu} is lower than that in the bulk, with a 0.25 eV difference in the lowest energy Cu-poor (110) case. This will generate a driving force for

Na diffusion from SLG substrate to the film surface, which corroborates the experimentally measured diffusion profile shown in Figure 4.4.

It has been suggested that in CIS, the Na would be more readily incorporated into regions with lower Cu content[98,168], which is supported by bulk calculations[221]. Our results indicate that both the surface concentration of Cu and the crystallographic surface orientation drive the Na_{Cu} defect formation. For example, under Cu-poor condition, the (110)-type surfaces have a 0.16 eV lower formation energy than the (112) surfaces; while under Cu-rich condition the formation energy for (110) surfaces is 0.03 eV higher compared that for (112). As the system moves towards equilibrium, Na will migrate towards the surface regions that have the lowest defect formation energy at the particular surface orientation and Cu content, which would lead to an inhomogeneous distribution of Na within the non-uniform film surface characteristic of sputtered CIS films[98,191,217]. This proposed mechanism agrees with previous reports[153] and is corroborated by the variations in measured surface Na content (Figure 4.4).

4.4.1 Effect of TOP:S on Surface Formation Energy of Na_{Cu}

Figure 4.11 shows changes in the Na_{Cu} formation energy near the film surfaces in the vicinity of TOP:S molecules. We observed an overall decrease in the Na_{Cu} formation energy for all four surface cases; the formation energy decreased by 0.53 eV for Cu-poor (110) surface, by 0.96 for the Cu-rich (110) surface, and by 1.33 eV for the Cu-poor (112) surface with TOP:S

treatment. This consistent lowering of the defect formation energy in the presence of TOP:S suggests that TOP:S passivation stabilizes Na defects in the vicinity of the surface, including the Na that diffuses from SLG substrate towards the surface through the film and the those that are dissolved in TOP:S solution from the SLG substrate and re-deposited onto the film surface. An important finding is that the reduction in Na_{Cu} formation energy in the presence of TOP:S passivation depends on the surface conditions with no clear preference for a particular surface orientation or Cu content. We found the largest drop in the formation energy of 1.35eV to occur in the Cu-poor (112) surfaces; and the lowest such drop of 0.12 eV - for Cu-rich (112) surfaces. Figure 4.12 shows the optimized geometries for various surface conditions and reveals a correlation between the defect formation energy and surface conditions. In all four cases, the surfaces were cleaved along [110] or [112] directions, terminating at a minimum energy surface. For the Cu-rich (110) and Cu-poor (112) surfaces, the Na_{Cu} site is in the topmost atomic layer within the free surface, which leads to its better positioning for interacting with the TOP:S molecule. For the Cu-rich (112) and Cu-poor (110) surfaces, the Na_{Cu} site is in the second atomic layer, buried by a topmost layer of Se atoms, which inhibits its access to the TOP:S molecule. In the Cu-poor (110) surfaces, the lattice is less densely packed due to the removal of the Cu atoms, which enables the S atom in the TOP:S molecule to penetrate into the surface, whereas in the Cu-rich (112) case, the interactions between a Na defect and the TOP:S molecule is hindered by surface geometry. This implies that Na defects in Cu-rich (112) surfaces are the least stable after passivation

compared to all other studied surface conditions, which explains its lowest formation energy reduction.

4.5 Summary

In this chapter we investigated the effects of TOP:S solution passivation on CIS thin films used in solar devices. The passivated films show a ~30x enhancement in photoluminescence, which increases with passivation temperature to 120 °C and time up to 24 hours. Surface XPS measurements on passivated samples reveal the formation of –S and –P bonds between the TOP:S and CIS and a >3-fold increase in the surface Na concentration. This is significantly higher than the increase from high-temperature annealing alone and follows the same trend with temperature and passivation time as PL. EDS analysis on the film cross-sections reveals a saddle-shaped Na concentration profile along the film height in the as-fabricated films and a bottom-to-top concentration gradient after passivation. We postulate that the higher Na content at the film surface creates a surface dipole that shifts the surface energy level and suppresses surface recombination in passivated films.

Our DFT calculations on stoichiometric and Cu-deficient systems reveal that:

(1) Na_{Cu} substitution is the most energetically favorable defect type in bulk CIS,

(2) Na_{Cu} defect formation energy is lower for the film surface compared with bulk and decreases after passivation,

(3) The defect energetics of Na before and after passivation are related to both the concentration of Cu at the surface and the crystallographic orientation of the surface, with Cu-poor surfaces having the lowest formation energy after passivation. (most favorable).

The experimental and computational results of this work indicate that TOP:S passivation introduces an additional driving force for Na diffusion within the solid CIS films and stabilizes the alkali metal defects, like Na and K, on CIS film surfaces, all of which lead to a greater surface Na content and reduced surface recombination in passivated films. This renders TOP:S a promising and effective passivation material for CIS-based photovoltaics. These studies provide fundamental insight and practical knowledge towards understanding the role and distribution of Na defects within CIS films and the effects of passivation, which will help create better solar cell devices.

Chapter 5 : Microstructure and Hierarchy in Hard Biomaterials

We will now switch gears and look at biomaterials in nature, which often possess highly complex microstructures, and ordered arrangement of these microstructures that are referred to as hierarchy. The microstructure and hierarchy in biomaterials usually arise as a result of a limitation of resources: each species in nature only has access to a (usually limited) subset of materials that it can use as building blocks. This limitation, together with the ever-escalating needs for better performing materials as a result of evolutionary competition, lead to hierarchical biomaterials often display extraordinary properties that surpass the constituent ingredients. Because of this, bio-mimetic, the study and incorporation of design clues from natural materials, has fascinated many researchers. In this chapter, we discuss how nature achieve enhancement of material properties by using hierarchy, and how we can utilize similar hierarchical design to make better manmade structures; in Chapter 6, we look at marine diatoms, and how they use a combination of unique microstructure and efficient hierarchical design to achieve extraordinary mechanical strength; in Chapter 7, we further investigate the material system POSS that allow us to capture the microstructure of diatom frustules, as well as provide us the ability to 1:1 replicate diatoms' hierarchical design.

5.1 Structural hard bio-materials: an overview

Hard biological materials like bones, antlers and shells, have played a major role in the history of humankind. Their high strength, toughness and light weight made them ideal for tools and weapons before the advent of engineering materials like metal composites and ceramics. In recent years, interest in these structural hard bio-materials have been re-ignited following the advances of material characterization techniques, as researchers discover that the reasons behind the often exceptional strength/density/toughness of these materials lie not in their underlying constituent materials, but in complex microstructure and often hierarchical arrangement of these constituents[246]. By combining relatively simple materials like chitin[247] and keratin[248], hydroxyapatite[249] and silica[250], natural bio materials like nacre, bones and diatoms are able to achieve extraordinary light weight and high mechanical strength that surpass their constituent materials by several orders of magnitudes[246], and even surpasses the predictions from the widely-accepted rule of mixture that are used in alloying the designing composite materials[251]. Another exceptional feat of many biomaterials is they often simultaneously possess high strength and high toughness, two properties that have typically been considered mutually exclusive in engineering materials[252,253]. A prime example of this property is the bones in our body, which possesses high strength and stiffness as a result of the mineral reinforcement, but at the same time are highly resistant to fracture and exhibits much higher fracture toughness compared to materials of similar relative density[254]. For these reasons, the scientific community has long been fascinated by hard bio-

materials and their microstructural design. Significant efforts and advances have been made in this field in the past decade, in the following of this chapter we will look at three notable examples of hierarchy in biomaterials: (1) nacre and keratin-based materials, (2) bones and hydroxyapatite-based materials, and (3) diatoms and silica-based materials.

5.2 Nacre and Mollusk Shells: Simple but Effective Brick and Mortar Structure

Mollusk shells are mostly made of minerals (at least 95% by volume), with a small fraction of organic materials[255]. Nacre is the strongest and toughest among the different materials found in the mollusk shell family, possessing high stiffness (70–80 GPa), high tensile strength (70–100 MPa) and high fracture toughness (4–10 MPa m$^{1/2}$)[255–258]. Nacre is able to achieve such extraordinary mechanical properties with a relatively simple brick-and-mortar microstructure, and even simpler ingredient materials. Figure 5.1 which is adapted from Barthelat et al.[252], shows a schematic of the brick-and-mortar layout of nacre, consisting of polygonal mineral tablets and that are made of "mesocrystals" formed by nano-sized grains with the same crystallographic orientation[259]; and organic materials that separates them and serve as "adhesive", hence the "brick-and-mortar" moniker[260]. When subjected to tension, which is the most common stress state of mollusk shells in their natural environment[261], these tablets would slide against each other, while being held together by the organic "adhesive"[256,258,262]. In a fracture event, this sliding mechanism leads to effective toughening

in the form of crack bridging and process-zone toughening[263,264], which increases fracture toughness of nacre to several orders of magnitude above the aragonite that constitute the individual tablets[261,264].
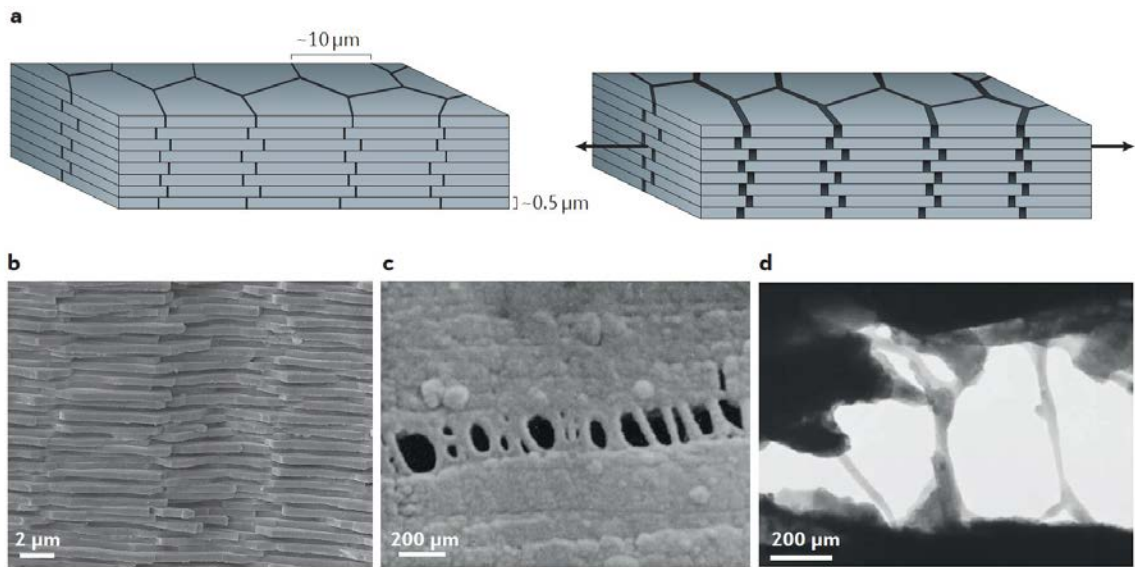
Figure 5.1 The structure, deformation and interfaces of nacre. (a): A schematic of the brick-and-mortar structure of nacre. The deformation of nacre under tension is dominated by the sliding of the mineral tablets on one another. (b): An SEM image of the fracture surface of red abalone nacre. (c): Separating the tablets in the out-of-plane direction reveals a highly deformable matrix. The SEM image shows the formation of cavities and ligaments. (d): The ligaments can elongate to great lengths. In this transmission electron microscopy image, the ligaments are up to 500 nm long, which is more than 10 times the initial thickness of the interface. Adapted from Barthelat et al.[252]

5.3 Bone: Complex Microstructure and Hierarchy Lend to Multiscale Toughening Mechanisms

Bones in human and other animal body serve many different functional purposes, and have highly varied shape and structure depending on their location and type[265]. One of the key functions, especially for highly dense cortical bone, is providing mechanical support. In order to achieve that, bone has developed a highly complex hierarchical structure that spans multiple length scales, with features ranging from the nanometer to macroscopic[249,266]. Figure 5.2 (adapted from Tertuliano and Greer[77]) shows a schematic of these different features. At the lowest end of the spectrum, individual collagen molecules form ordered structures called fibrils through hydrogen bonding[267]. Within each fibril, covalent crosslinks at the ends of collagen molecules provide additional adhesion, as well as complex unravelling mechanisms as they stretch[268]. At the nanometer scale, each fibril is reinforced by hydroxyapatite nanocrystals following a mineralization process that are controlled by the collagen molecules, which make them highly stiff and strong[269,270]. Individual fibrils then bundle into fibres, which in turn arrange into cross plies at the micrometer scale. Finally, the plies and lamellae are arranged in a concentric pattern to form osteons, millimeter scale building blocks of cortical bones[249,271].
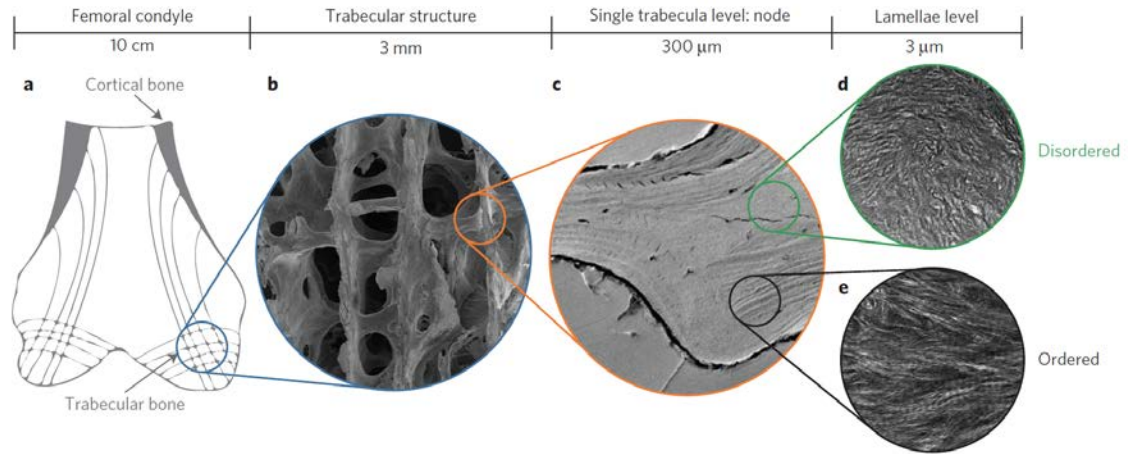
Figure 5.2 Microstructures and hierarchy of trabecular bone. (a) A cross-sectional schematic of the lower femoral condyle shows that the trabecular structure is confined in spaces not occupied by cortical bone. (b-e) At the millimeter scale it is composed of beams and plates (b), while at the microstructural level (c) there is a combination of an ordered lamellar structure (e) in the beams and a disordered structure (d) at the center of the nodes, where the beams intersect. Adapted from Tertuliano et al.[77]

While the stiffness and strength of bone mostly come from the stiffness and strength of the individual component such as hydroxyapatite-reinforced fibrils[272], their impressive fracture toughness is a result of the complex microstructures and hierarchy at different length scales[265,273]. These microstructures provide a number of toughening mechanisms such as fibril sliding at nanometer scale[274], sacrificial bonds between the fibres at micron scale[275], and various crack-bridging mechanisms between 10 and 100 microns[276,277]. These different mechanisms work in conjunction to make bones highly resistant to fracture without

sacrificing stiffness and strength, surpassing the predictions from the rule of mixtures[251], and serve as a prime example of enhancing mechanical property using hierarchical design.
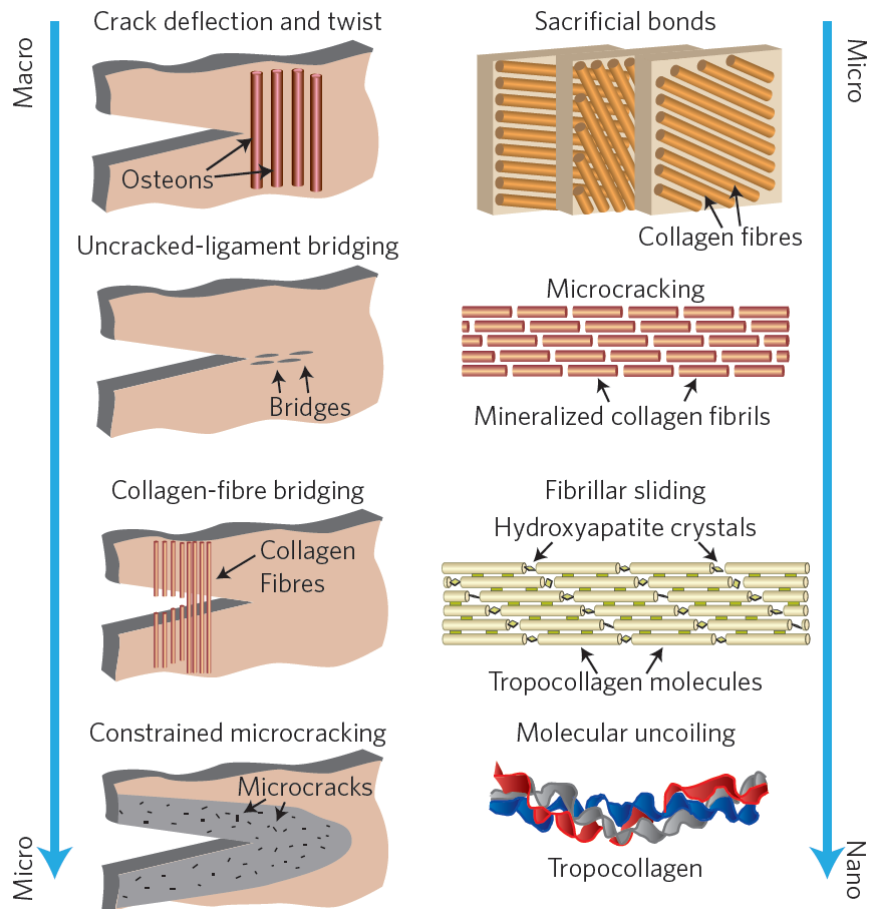
Figure 5.3 Fracture-resisting mechanisms in cortical bones. Intrinsically, collagen fibrillar sliding is the prime plasticity mechanism in bone, and as such has the largest impact on the inherent resistance of the hydroxyapatite/collagen composite. Other mechanisms include molecular uncoiling, microcracking and sacrificial bonding, all of which operate at sub-micrometer length scales. Conversely, extrinsic mechanisms, such as

uncracked-ligament bridging and crack deflection, occur at micrometer
length scales once the crack begins to grow so as to shield the crack tip.
Adapted from Wegst et al.[246]

5.3 Diatoms: Simple Organism with Intricate Hierarchical Design

Diatoms are single-cell algae that form a hard cell wall made of a silica/organic composite. The ability to produce a functional biosilica shell presents several natural precedents that fascinate and inspire scientists and engineers. One fascinating aspect of such silica glass shells is their intricate, varied and detailed architecture, which has served as an inspiration for various hierarchical man-made structures[1]. Diatoms are generally classified based on the symmetry of their shells: centric diatoms display radial symmetry while pennate diatoms have bilateral symmetry[278]. Figure 5.4 shows images of several marine and fresh water diatom species[279]. A diatom frustule usually consists of two halves that are connected around the mid-plane of the diatom cell. While their design and architecture vary between species, the frustules commonly incorporate (1) highly porous walls that sometimes contain hollow chambers, (2) varying thickness among different parts based on structural importance[280], and (3) hierarchical arrangement of the pores in complex, often radial patterns[281]. The cross-section of frustule walls can also contain of multiple layers and hollow cells in between them, as observed in many larger marine diatoms[250,278,281].
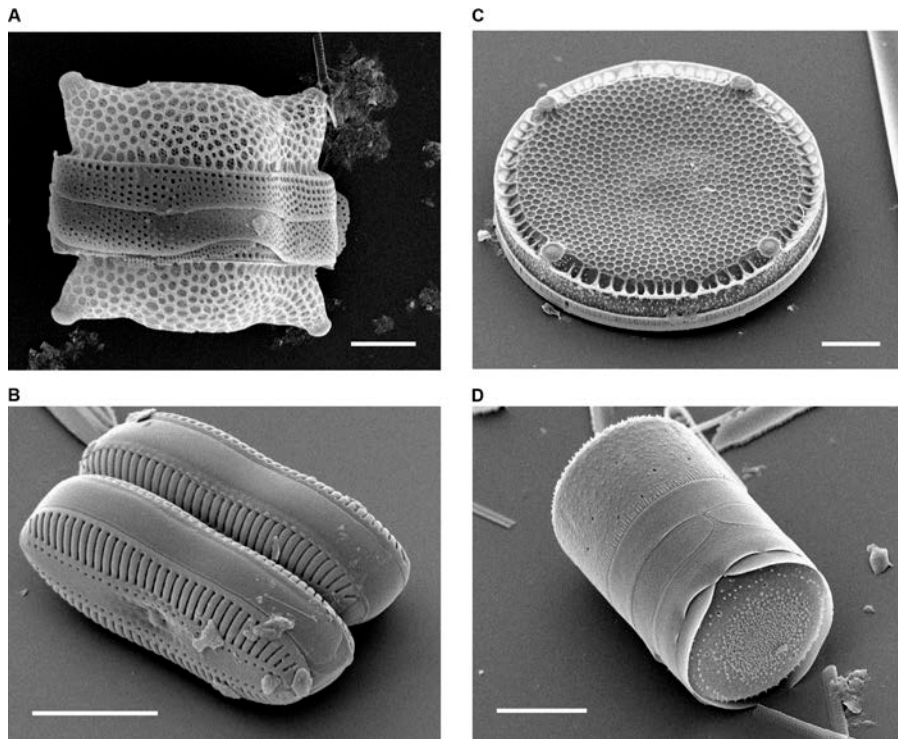
Figure 5.4 SEM images of different diatom species. (A) Biddulphia reticulata. The whole frustule of a centric diatom showing valves and girdle bands (scale bar = 10 micrometers). B) Diploneis sp. This picture shows two whole pennate diatom frustules in which raphes or slits, valves, and girdle bands can be seen (scale bar = 10 micrometers). (C) Eupodiscus radiatus. View of a single valve of a centric diatom (scale bar = 20 micrometers) (D) Melosira varians. The frustule of a centric diatom, showing both valves and some girdle bands (scale bar = 10 micrometers). Adapted from Bradbury et al.[279]

The proposed evolutionary functions for these intricate shell designs include nutrient acquisition, control of diatom sinking rate, control of turbulent flow around the cell, and protection from grazing and viral attack [282]. Evidence in favor of a protective function is that

the degree of shell silification depends on the environment, with greater amounts of silica found in shells grown in a predatory environment [280]. As a deterrent to predation, the frustule makes use of an inherently brittle glass as a structurally protective material while balancing other evolutionary pressures. A denser shell may provide greater protection, but will cause the diatom to sink beyond depths suitable for photosynthesis. A solid shell might also prevent exchange of resources and waste between the diatom cell and its environment. This requires adaption through control of the frustule micromorphology or modification of the constituent silica/organic composite material [250].

Several research groups have conducted different mechanical experiments to extract properties of diatom frustules. Almqvist, et al. performed AFM indentation on the pennate diatom *Navicula pelliculosa* that had been rinsed in ethanol and dried [283]. They reported hardness values up to 4.5-12 GPa in the homogeneous central regions of the frustule, which are expected to act as load-bearing features. Reported elastic moduli varied from 7 up to hundreds of GPa from the outer to central regions and was sensitive to the method used to determine the indentation depth.

Subhash, et al. performed similar experiments on the centric diatom *Coscinodiscus concinnus* using nanoindentation and reported the elastic modulus to range from 0.35 to 2.8 GPa and the hardness – from 0.08 to 0.12 GPa, both of which varied from the outer frustule edge to the center of the frustule and within local regions [284]. The authors noted that the

porosity and the nonplanar nature of the frustule made accurate extraction of the mechanical properties difficult. Hamm, et al. measured the force required to break the frustule of a living diatom for two centric diatom species (*Thalassiosira punctigera, Coscinodiscus granii*) and one pennate species (*Fragilariopsis kerguelensis*) [285]. Compression tests were performed using a glass microneedle mounted on a micromanipulator. They observed an inverse relationship between the diameter of the diatom frustule and the force required to break it, 129±33 µN being the breaking force for a 100-µm diameter sample when loading across the girdle band and 171±70 µN for a 50-µm one. 3D finite element method (FEM) simulations of the same pennate diatom revealed that the ribs of the frustule acted as load-bearing structures that shielded porous regions from high stress concentrations. Losic, et al. built upon the previous AFM indentation studies to probe the mechanical properties of different components within the frustule for the centric *Coscinodiscus* sp. diatoms and performed nanoindentation on the individual frustules and on full diatoms[286]. The authors reported elastic modulus to vary from 1.7 GPa for the outer cribrum layer, 15.6 GPa for the inner basal plate, and 4.0 GPa for the girdle band. Hardness was reported at 0.13, 0.53, and 0.06 GPa for the same regions. The authors attributed this variance to differences in the local pore structure and possible differences in the biomineralization process.

Bjørnøy, et al. performed *ex situ* three-point bending tests on beams 20-22 µm in length and 3-3.5 µm in width that were extracted from the frustule of a *Coscinodiscus* sp. and reported their failure strengths to be 336±73 MPa [287]. The data analysis in this work was challenging

because of the un-quantified effects of the deposited platinum used to anchor the ends of the beam, as well as of the sharp conical indenter tip that the author noted could locally penetrate the frustule beam. FEM simulations on the elastic response of this material revealed that a frustule beam that contained pores deformed close to 50% more compared with a non-porous frustule beam. Vebner, et al. expanded the work of Bjørnøy, et al. using *Coscinodiscus centralis* diatoms to perform *in-situ* nano-indentation and cantilever bending experiments and demonstrated tilting of the frustule during testing, with no material properties reported[288].

Despite the body of literature on mechanical properties of diatom frustules, there are no conclusive results yet on either the effect of their material microstructure, or the effect of the frustule hierarchy, as the reported results often show significant variation between different species, as well as on the same species using different testing methods. Thus, to really understand the roles and inter-play between the microstructure and hierarchical design, more systematic studies on diatoms' mechanical properties is required.

5.5 Man-Made Hierarchical Materials: Inspired by Nature and Leveraging Size Effect

Using hierarchy and architecture to enhance mechanical performance is not uncommon in man-made structures. For example, Eiffel Tower is able to maintain mechanical integrity despite weighing significantly less than traditional "bulk" buildings like the Great Pyramid[1], thanks to its carefully arranged beam design. Recently, there has been growing interest in the

field of materials science and mechanics to adopt hierarchical design cues from nature to make man-made structures and meta-materials. For example, micro- and nano-lattices take inspiration from hollow silica shells of marine diatoms[10,289]; periodicities in surface patterning in photonic crystals are inspired by the unique microstructures found on wings of butterflies that allow them to change color under different lighting conditions[290,291], and the mixing of dense- and porous- phases that provides additional toughness found in the stomatopod dactyl club inspired damage-tolerant structural coatings[292,293]. Just as biomaterials achieve extraordinary properties by incorporating microstructure and hierarchical design optimized by evolution, these bio-mimetic materials and designs are also able to achieve materials properties that are otherwise un-obtainable by simply mixing the constituent materials[246].

In addition to leveraging hierarchical microstructure, many of these man-made structures and meta-materials also take advantage of the material size effect discussed in 1.3. The idea being by introducing hierarchical design, we are able to reduce the smallest length scale in the material, where the "smaller is stronger" or "smaller is more ductile" effect begin to take place[11]. A prominent example of this is the series of studies spearheaded by the Greer group on nanometer-scale architected lattice materials[10–12,294]. These so called "nano-lattices" can (1) create stiff, strong and lightweight scaffolding as battery electrodes[295], for bio-medical devices[296], or piezo-electric applications; (2) achieve almost full recoverability with stiff and brittle ceramic materials[12], (3) serve as backbone for photonic crystals with variable bandgap

as a function of applied load[297]. Figure 5.5 shows polymer nanolattices of different geometries, all incorporating multiple levels of hierarchy[11]. In many instances, these applications are fueled by the "smaller is stronger" size effect, which made the lattice structures stronger than its component beams[294]. With the rapid progress in lattice-type and other bio-mimetic materials, we need a better understanding of the interaction between the hierarchical design and intrinsic materials microstructure in these structures. And to that end, a better understanding of the "success stories" in nature.
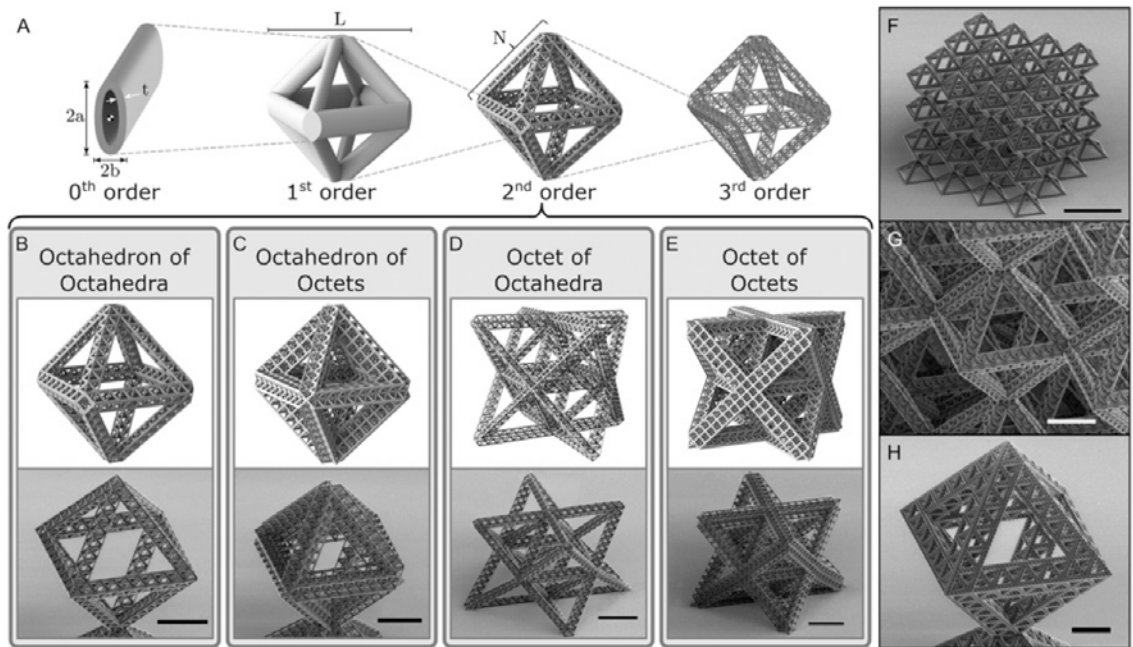
Figure 5.5 Schematics and SEM images of nanolattices that incorporate hierarchical design. (A) CAD images illustrating the process of making a third-order hierarchical nanolattice. (B, Upper,

C, Upper, D, Upper, and E, Upper) CAD and (B, Lower, C, Lower, D, Lower, and E, Lower) SEM images of the various second-order samples. (Scale bars: 20 μm.) (F) SEM image of a second order octahedron of octahedral lattice. (Scale bar: 50 μm.) (G) A zoomed-in image of the second-order octahedron of octahedral lattice showing the first-order repeating units that make up the structure. (Scale bar: 10 μm.) (H) SEM image of a third-order octahedron of octahedral of octahedral. (Scale bar: 25 μm.). Adapted from Meza et al.[11]

Chapter 6 : Microstructures and Mechanical Properties of Diatom Frustules

As we move into more complex, hierarchical materials, the interaction between material microstructures and structure hierarchy becomes increasingly important to the overall mechanical response. It is crucial that we understand microstructures and hierarchy each contribute to the overall mechanical property of a material, in order to design materials that can surpass the rule of mixture to reach untapped property space[246]. In this chapter, adapted from Aitken et al.[298], we take a deep dive into nature's inspiration to hierarchical structures: marine diatom frustules, which use hierarchical design to overcome a primitive microstructure and achieve extraordinary mechanical strength. The insight that can be gained from studying microstructures and mechanical properties of diatoms will serve as important foundation for designing various bio-mimetic structural materials.

6.1 Introduction

Diatoms are single-cell algae that are often recognized by their hard bio-composite outer shells[278]. These shells, also called frustules, are made with a silica (SiO_2) like material, and serve multiple purposes including buoyancy, nutrient exchange, and mechanical protection[282,285]. In recent years, with the advances in small scale mechanical testing

techniques, there has been a growing interest in the mechanical properties of diatom frustules. Hamm et al. pioneered small scale mechanical study of diatom frustules, and found that they have impressive mechanical strength and ductility, despite being mostly made of stiff and brittle silica[285]. Following their discovery, several groups have conducted various experiments on different types of diatom frustules. A detailed review of these studies can be found in Section 5.3.

Despite the growing interest and efforts, mechanical experiments on diatom frustules prove rather difficult. The size of most diatom species ranges from 2 to 200 µm [278,299], which renders most of the traditional mechanical testing methods inadequate to characterize such complex materials; a few mechanical studies on diatoms have been reported [283–288]. The majority of studies perform AFM indentation[283–286] on a full frustule of centric or pennate diatoms. Reported values of hardness ranged from 0.06 - 12 GPa and values of elastic modulus from 0.35 – 22.4 GPa. Differences in local pore structure and the nonplanar geometry of the frustule were often cited for the variance in mechanical properties. Three-point bending tests on beams that were extracted from the diatom frustule reported failure strengths of 336±73 MPa, but were complicated by local penetration of the indenter tip and tilting of the frustule during testing[287,288].

This overview demonstrates a wide range in the reported hardness and elastic moduli for biosilica shells. Most of these experiments were performed on full diatom shells, which in

some instances contained organic cellular material; it is unclear whether the measured mechanical data represents the deformation of the constituent biosilica or the overall deformation of the shell through bending, local twisting, pivoting, etc. Indentation using AFM can introduce inaccuracies such as tip-sliding, and the resulting uncertainty in compliance within a single set of experiments, as well as among the data obtained with different instruments, makes it challenging to compare mechanical properties of the diatoms across the reported experiments. Within a single species, these mechanical data may provide qualitative trends in the structural response of the diatom shells; it is difficult to make any conclusions on the mechanical properties of the constituent biosilica. The mechanisms of silica biogenesis likely varies among the species [300], but it is unclear to what extent these differences reflect the variation in elastic modulus and hardness between species and within an individual frustule.

We conducted *in-situ* three-point bending experiments on beams with roughly 3.5 µm square cross-sections fabricated from the frustule of *Coscinodiscus* sp. performed in a scanning electron microscope (SEM) equipped with a nanoindenter, as well as *ex-situ* nanoindentation on an individual basal plate that had been isolated from a frustule and the girdle band. We determined the elastic modulus to be 36.4±8.3 GPa and the failure strength to be 1.1±0.3 GPa. We discuss these results, as well as deformation and failure mode of the diatoms, in the context of their atomic-level microstructure obtained from TEM analysis and finite element method (FEM) simulations of the three-point bending tests.

6.2 Methods

Diatom sample preparation: *Coscinodiscus* sp. used in this study were obtained from the Biological Institute at Norwegian University of Science and Technology and had been previously collected from the Trondheimsfjord inlet of the Norwegian Sea. These samples were washed in MQ water, centrifuged in a solution of 3 mL H_2O_2 and 1 mL HCl, and finally rinsed with MQ water and ethanol. This treatment was intended to remove the cellular organic material and to separate the frustule half-shells and girdle band from one another; this type of treatment also unintentionally fractured many of the components. Samples were stored in methanol prior to nanomechanical experiments. SEM samples were prepared by applying a drop of this methanol solution containing the cleaned diatoms onto a silicon chip that was coated with 100 nm of gold and then allowing the methanol to evaporate in air. Despite the absence of a conductive coating, we found that the diatoms could be successfully imaged in SEM with no excessive charge accumulation. Figure 6.1 show SEM images of frustule samples after cleaning and mounting.
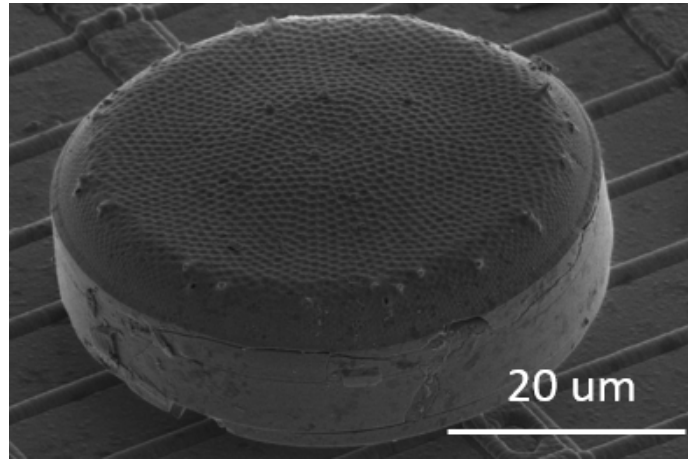
Figure 6.1 SEM image of a *coscinodiscus sp.* frustule after the cleaning process

Three Point Bending Experiments: Samples for bending experiments, TEM analysis, and ex-situ nanoindentation were fabricated using the FIB lift-out technique in a dual-beam SEM (FEI, Versa 3D) [301]. Once an intact frustule was identified, a cantilever beam with plane dimensions of 3.5 x 24 µm was milled out of the center of the frustule at 16 kV and 0.25 nA. The depth of the beam was set by the thickness of the frustule shell and was approximately 3.5 µm. A site-specific, platinum deposition needle and tungsten micromanipulator (FEI, EZLift) were used to extract the sample. The micromanipulator was welded to the free end of the cantilever beam using Pt deposition and the opposite end of the cantilever was milled away from the parent frustule. Figure 6.2 shows SEM images of this lift-out procedure. The beam was then transferred onto a stainless steel substrate and placed over pre-fabricated 20x20x40 µm wells. The same micromanipulator was then used to position the beam such

that its gauge section was parallel to the short edge of the well and spanned it entirely, ensuring that the shell plane normal was perpendicular to the loading direction, as shown in Figure 6.2(d). This type of parallel loading allows us to deform all frustule layers simultaneously and removes the complications caused by the compliance differences between layers and the possibility of localized deformation that emerges when the frustule layers are loaded in series [287,288]. This orientation also limits the influence of the areolae walls and simplifies the calculation of stresses within the beam.
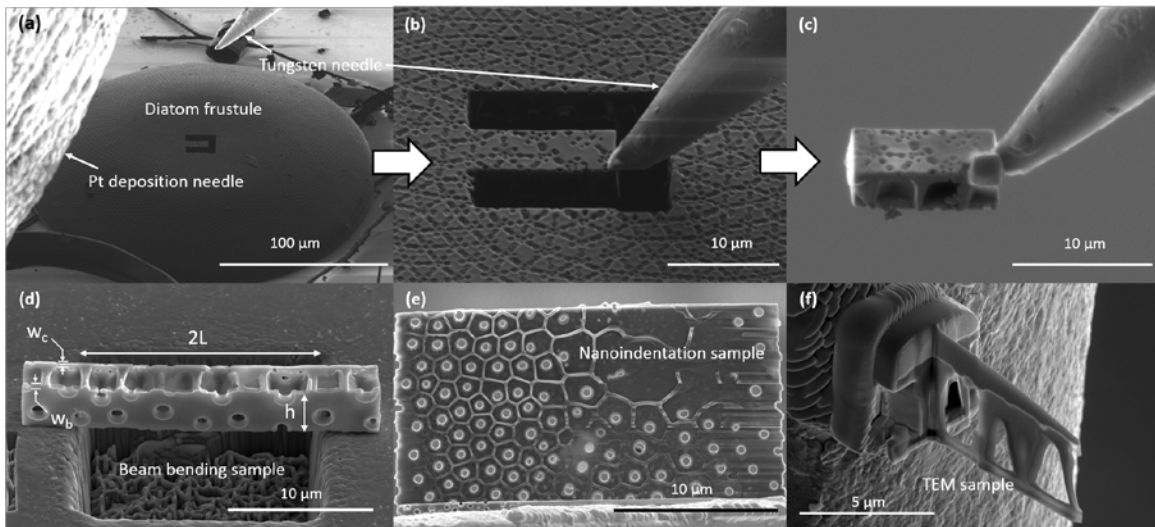
Figure 6.2 The FIB lift-out process and different samples. (a-c) SEM snapshots demonstrating the focused ion beam lift-out method. The FIB is used to mill out a rectangular sample and a Pt deposition needle is used to attach to the tungsten micromanipulator for lift-out. This technique can be used to prepare (d) bending samples, (e) nanoindentation samples, and (f) TEM lamella from the frustule shell. Dimensions of the beam sample are shown in (d). The gauge length of the beam is *2L* and the height of

beam is h. Thickness of the cribrum layer, w_c, and basal layer, w_b,
are also shown.

Bending tests were performed in a custom-made *in-situ* SEM (FEI, Quanta) with a nanomechanical module, InSEM™ (Nanomechanics, Inc.). A wedge-shaped diamond tip with a radius of 5 µm was used to indent the beam at a constant nominal displacement rate of 5 nm/s to failure. Load and displacement were continuously measured at a rate of 500 Hz with a simultaneous video capture of the deformation process. Stresses and strains were calculated along the bottom edge of the beam directly under the point of applied load, which corresponds to the point of maximum tensile stress:

$$\sigma = -\frac{My}{I} \tag{6.1}$$

$$\varepsilon = -\frac{y}{\rho} \tag{6.2}$$

where M is the bending moment, y is the perpendicular distance away from the neutral axis of the beam, I is the cross-sectional moment of inertia, and ρ is the radius of curvature. At the point of maximum tensile stress, the moment $M = \frac{PL}{2}$ and $= -\frac{h}{2}$, P is the applied load, L is half the span of the gauge section, and h is the height of the beam. The contribution from the cribrum and basal plate to the moment of inertia are $I_{cribrum} = \frac{1}{12}h_c^3 w_c$ and $I_{basal} = \frac{1}{12}h_b^3 w_b$, respectively, where w is the thickness of the layer and subscripts c and b refer to the cribrum and basal plate. As shown in Figure 6.2(d), the gauge section, $2L$, and the beam

height, h, are dimensions that lie within the shell plane, the width w, is perpendicular to the shell plane. Estimation of the contribution to the moment of inertia from the areola lattice can be difficult due to the directionality of the hexagonal cell array. Under this loading configuration, an individual areolae wall has a thickness, $h_{aerola} = 300\ nm$ and a width, $w_{aerola} = 2.5\ \mu m$, so that $\frac{h_{aerola}}{h_{cribcrum}} \sim 0.1$ and $\frac{w_{aerola}}{w_{cribcrum}} \sim 10$. The predicted contributions to the area moment of inertia from the areolae walls with these dimensions are at least 2 orders of magnitude less than the individual contribution from the cribrum and from the basal plate, which makes it reasonable to exclude the contribution of areolae from the analysis. We observed a small, <3° bi-axial curvatures in the as-fabricated frustule beam, possibly due to relaxation of residual stresses after its extraction from the frustule plate. To account for this curvature, the height of the beam was calculated as the average of the two layers measured after sample extraction, $\frac{h_c + h_b}{2}$. This results in the following expression for the uniaxial tensile bending stress in the bottom edge of the beam:

$$\sigma_{beam} = \frac{3PL(h_c + h_b)}{2(h_c^3 w_c + h_b^3 w_b)} \tag{6.3}$$

The beams tested in this work were not fixed to the substrate to avoid generating boundary constraints, so any initial misorientation of the beam or misorientation of the indenter tip with respect to the beam resulted in "settling" events during testing manifested by marginal tilting and translation of the beam prior to attaining full contact. As a result, the measured

indenter displacement could not be used to calculate strain in the sample. Using the acquired video frames, we analyzed 450 still images taken between incipient sample loading up to failure, to track the position of 7 points along the bottom edge of the bending sample. The position of these points were fit to a circle with radius ρ and used to determine the tensile strain as

$$\varepsilon_{beam} = \frac{(h_c + h_b)}{4\rho} \qquad (6.4)$$

TEM Analysis: Samples for TEM analysis were fabricated using the described lift-out procedure; with the extracted lamella transferred and attached to the Cu TEM grid using the Pt deposition needle in the FIB. The attached TEM samples were then thinned using FIB to a thickness of less than 100 nm using a voltage of 16 kV and progressively decreasing currents from 50, 11, 4 pA to ensure electron transparency. A thinned TEM lamella is shown in Extended Data Figure 1f. Microstructural analysis was performed via transmission electron microscopy (FEI, Tecnai F30) at an accelerating voltage of 300 kV. Standard-less energy dispersive spectroscopy (Oxford Instruments, INCA EDX) was used to investigate the local elemental composition of the sample.

Nanoindentation: Fabrication of a basal plate for nanoindentation was prepared using the described lift-out technique to extract a 25 x 25 µm plate from the basal diatom plate. The removed plate was then transferred to a copper TEM grid for thinning. The plane of the frustule shell was oriented parallel to the ion beam, and the cribellum, cribrum and areolae

walls were removed using milling conditions of 16 kV and 50 pA, leaving only the basal

plate (Figure 6.2(e)). Using the tungsten micromanipulator, the basal plate was transferred

from the TEM grid to a stainless steel substrate and secured by depositing Pt along the edges

of the plate. Decomposition and fracture of the diatom shell during cleaning resulted in

several girdle bands suitably oriented for nanoindentation on the substrate, which was

performed with no modification to the structure. Nanoindentation was performed *ex-situ* in

a Hysitron nanoindenter using a diamond Berkovich tip under a constant nominal

displacement rate. The thickness of the basal plate and girdle used here was observed to vary

between 600 to 700 nm, so indentation was performed up to a total displacement between 50

to 300 nm. Elastic moduli were calculated using the method of Oliver and Pharr [302].

FEM Simulations: A CAD model of one of the bending samples was meshed using 729,000

tetragonal elements in ABAQUS simulation package 6.14 (SIMULIA). To emulate three-

point bending, the beam was modeled in contact with steel supports on both ends and

displacement was applied via a diamond roller from the top. The beam was assumed to have

an elastic modulus of 35 GPa, closely matching the experimental value obtained here. The

steel supports and diamond roller were assumed to have elastic moduli of 200 GPa and 1000

GPa, respectively. Nodes on the bottom face of the steel supports were specified to have no

displacement and hard, impenetrable contact via penalty enforcement was assumed between

the beam and steel supports and between the beam and diamond roller. A friction coefficient

of 0.1 was applied between the steel supports and the beam to prevent lateral sliding during

bending. Displacement of the diamond roller was chosen such that the resulting maximum tensile beam strain was similar to experimental values calculated from the captured video. For comparison, bending simulations were also performed on a solid beam of similar dimensions and elastic modulus.

6.3 Results

6.3.1 Frustule Morphology and Microstructure

Figure 6.3 shows schematics and SEM images of the frustule of a *Coscinodiscus* sp. The cribrum and cribellum constitute the distal surface of the shell, and the basal plate composes the proximal surface. Areolae walls span these two layers and approximate a honeycomb lattice configuration. Figure 6.3(c) shows the hexagonal arrangement of pores of the cribrum and cribellum. The cribrum is composed of clusters of hexagonally-arranged, elliptical pores with average dimensions of 364 nm for the major axis, 283 nm for the minor axis, and the clusters are arranged in a hexagonal pattern. The cribellum layer is composed of 50 nm diameter pores that are hexagonally arranged across the entirety of the surface, and is laid atop the cribrum. Figure 6.3(d) shows the basal plate and areolae cells. Each areolae cell has 5-6 side walls and contains a single foramen with an average inner diameter of 822 nm.
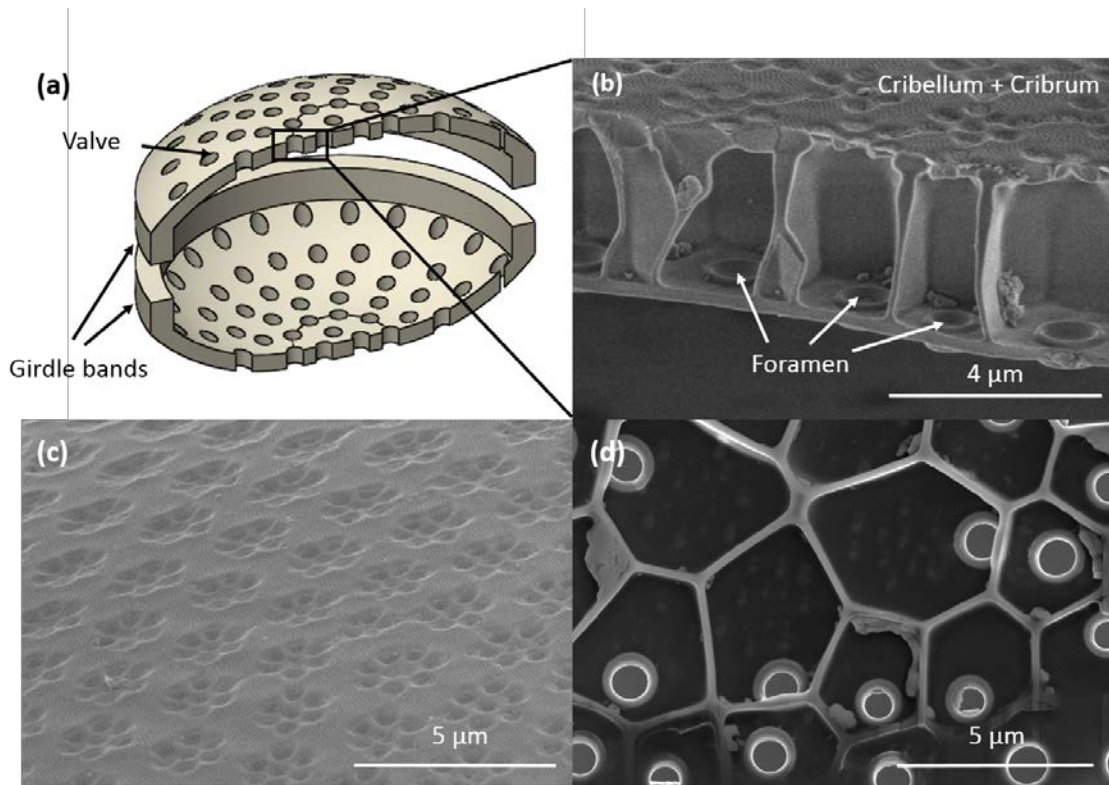
Figure 6.3 Schematics and SEM images of *coscinodiscus sp.* frustules. (a) Schematic showing diatom frustule shell. (b) Cross-section of shell demonstrating the honeycomb sandwich plate configure of the silica shell. (c) Cribrum, the outer layer of the frustule shell, displays hexagonal arrangements of pores. (d) The basal plate, the inner layer of the frustule shell, is punctuated by reinforced pores called foramina.

Figure 6.4(a) shows a TEM micrograph of the frustule of *Coscinodiscus* sp. Figures 6.4(b-d) provide site-specific EDS data with diffraction patterns in the insets and convey that the material in the areolae wall is made nearly exclusively of silicon. Smaller copper peaks correspond to signal contamination from the copper TEM grid. The inset diffraction pattern

indicates that the region is entirely amorphous. Figure 6.4(b) shows nearby regions that correspond to the interior surfaces of the areolae cell; the amorphous/nanocrystalline Pt peaks come from the Pt needle that was used during ion-beam assisted deposition and not from the biological sample. Figure 6.4(c) provides EDS data for a 275 nm-thick region of the basal plate and shows strong Si and Ga peaks, with the latter caused by the Ga^+-ion milling during thinning. It appears that Ga was localized within this basal plate region even though the entire sample was exposed to ion milling. We believe that the porosity observed within the nanocrystalline region (inset in Figure 6.4(c)) facilitated Ga sequestration into it; Ga content is lower in the amorphous regions (insets in Figure 6.4(d)). The difference in the microstructure between the nanocrystalline and amorphous silica is reflected in the difference in the diffraction contrast between the two regions (inset in Figure 6.3(a)) and shows that a sharp interface exists between the two microstructures.
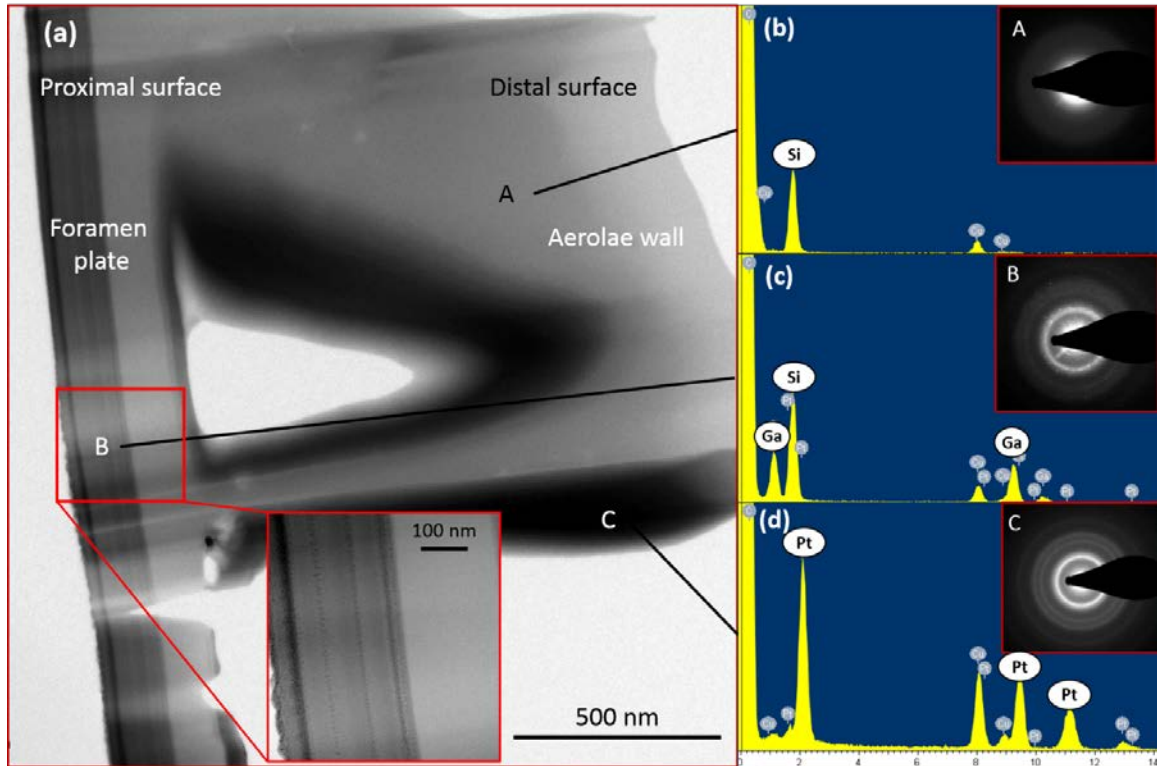
Figure 6.4 TEM analysis of the microstructures of diatom frustules. (a) TEM micrographs of the frustule shell. The inset gives a zoomed in view of the basal plate. EDS data and spot patterns taken from (b) region A, (c) region B, and (d) region C show that the majority of the frustule shell is amorphous silica.

6.3.2 Mechanical Experiments

Figure 6.5 shows the stress strain data for representative three-point bending tests. The data indicates linear elastic loading with no plastic deformation up to failure. Failure stress varied between 850-1460 MPa and failure strain varied between 2.2-4.0%. The average elastic modulus was calculated to be 36.4±8.3 GPa based on a linear fit to the slope. The experiments

were performed in displacement-controlled mode and if a settling event resulted in a displacement rate greater than the prescribed one, the instrument controller adjusted the indenter head to maintain the prescribed rate. This feedback response occasionally manifested itself as a drop in stress when the feedback loop adjustment caused a short local unloading. Figure 3e gives the calculated modulus against the contact depth acquired during nanoindentation of the basal plate and the girdle band. In both materials, the modulus decreased with contact depth. The modulus calculated from indentation on the basal plate varied from 21.0±7.7 GPa at 28 nm to 39.7±8.3 GPa at 217 nm and in the girdle band, from 19.9±2.1 GPa at 53 nm to 40.2±4.0 GPa at 267 nm.

Nanoindentation response of the isolated basal plate and the girdle band shows remarkable similarity. Average elastic moduli varied with increasing contact depth from 21.0±7.7 at 28 nm to 39.7±8.3 GPa at 217 nm in the basal plate, and from 19.9±2.1 at 53 nm to 40.2±4.0 GPa at 267 nm in the girdle band. The sub-micron thickness of the samples and the nanomechanical experiments in general render it challenging to eliminate all sources of experimental error. For shallow contact depths, some measurement error likely stems from the non-ideal geometry of the tip, and at greater contact depths, we encounter effects from the stiff substrate. Despite the uncertainty, these extreme cases set a range that matches well with the modulus calculated from bending tests.
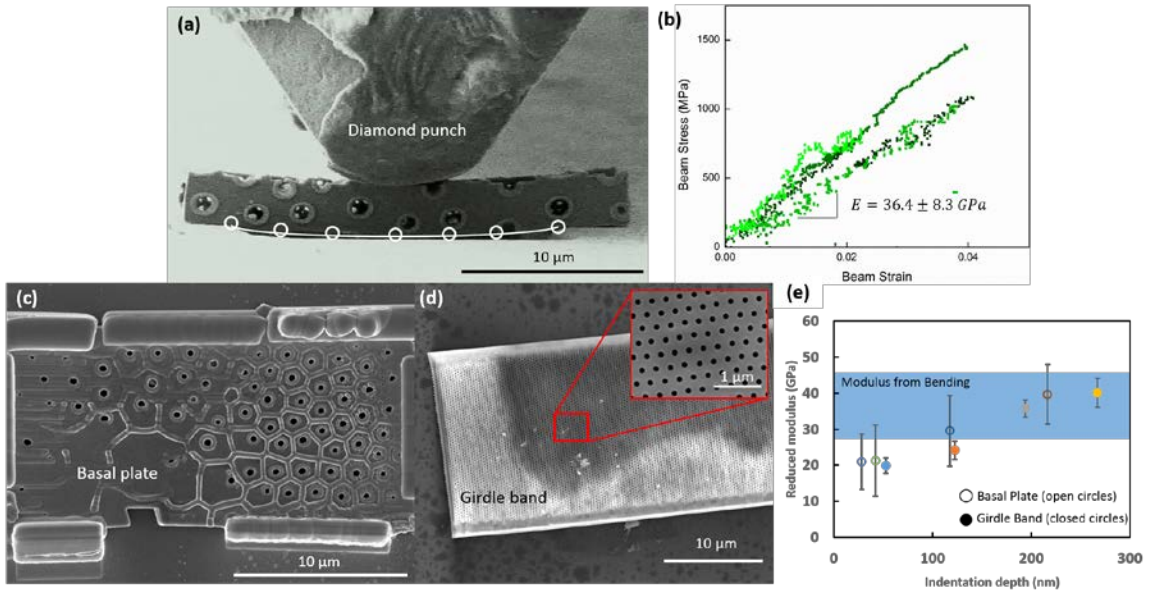
Figure 6.5 Mechanical experiments of diatom frustules. (a) Snapshot from a video of three-point bending of the frustule shell. Circles show the locations that were used to fit a circle for strain calculation. (b) Stress-strain data collected from bending experiments that has been corrected for rigid-body displacements. Nanoindentation was performed on (c) an isolated basal plate and (d) girdle band. (e) Shows the reduced modulus as measured from nanoindentation on both an isolated basal plate and girdle band plot against indentation depth. For comparison the elastic modulus as determined from bending experiments is also shown.

In all samples tested, failure was catastrophic and occurred faster than the imaging scan rate of the SEM. Upon failure, most samples released the accumulated strain energy by launching from the substrate and could not be recovered. Figure 6.6 shows one half of such a bending

sample that was recovered and shows that failure occurred by propagation of a crack through the center of the beam.
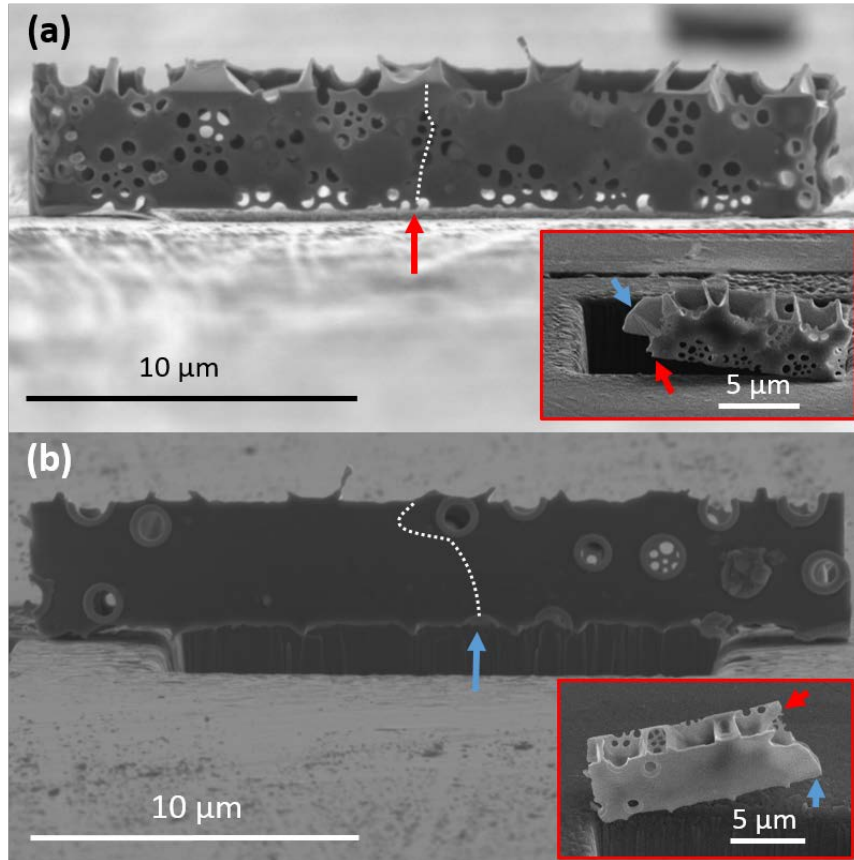
Figure 6.6 Crack propagation and the effect of pores in diatom frustules. (a) displays the path of crack propagation through the cribrum. The crack follows the stress concentrations surrounding the cribrum pores. (b) shows the path of crack propagation through the basal plate. The crack is deflected by the reinforced foramen. Insets show the fractured beam. The red arrow corresponds to the location where the crack intersects the bottom edge of the cribrum layer and the blue arrow corresponds to the location where the crack intersects the bottom of the basal layer.

6.4 Discussion

6.4.1 Microstructure and Silicification in Diatoms

The vast majority of the frustule, including the areolae walls, shows a smooth, amorphous microstructure (labeled Region A in Figure 6.4(a)). The only place where microstructure deviated from amorphous was within the basal plate, which shows several bands between 50-80 nm in thickness, oriented parallel to the frustule surface, and separated by striated patterns of darker contrast (Region B in Figure 6.4(a)). There is a 10 nm thick band that displays rough contrast that is adjacent to the smooth material in Region A. The nanocrystalline diffraction pattern in Figure 6.4(c) confirms the presence of these regions of local order. Region B has a total thickness of 275 nm, about 47% of the thickness of the basal plate and displays a darker contrast than the material in Region A, which suggests that it is either more densely-packed or contains a higher silica/organics ratio than material in Region A.

Previous work has uncovered that the microstructure of the frustule silica can vary between species and across stages of frustule development. Reported microstructures include compacted spheres, networks of fused spheres, silica microfibrils and smooth homogeneous silica [303,304]. Schmid, et al. and Rogerson, et al. investigated wall morphogenesis in centric diatoms *Thalassiosira eccentrica* and *Coscinodiscus asteromphalus* and identified "growing zones" that are loose aggregates of 12 nm-diameter silica spheres, where new frustule growth

occurred, and "compacting zones" that display a homogenous morphology where more mature growth had occurred [250,305]. In the centric diatoms studied by these authors, the frustule growth occurred in a distal direction such that the growing zones were oriented outward relative to the compacting zones. This orientation suggests that the differences in microstructure observed here likely do not correspond to growing and compacting zones. Observations of wall morphogenesis by Schmid et al. and Hildebrand, et al. reported the presence of clustered spheres in *Coscinodiscus wailesii* and *Thalassiosira pseudonana* [306,307]. These authors reported that frustule growth began in the center and extended compacted silica sphere strings radially to the margin. Later growth stages of the basal plate occurred by cross extensions and compaction, forming an 85-100 nm thick template for subsequent distal growth. The proximal nanocrystalline microstructures observed in this work may correspond to this initial basal template. It has been suggested that following radial growth, sintering plays an important part in the morphogenesis of the frustule by filling in the spaces of the compacted spheres with monomeric silica, flattening the deposition surface, increasing its radius of curvature and promoting adherence [304,308]. This type of sintering would result in the amorphous material observed in Region A shown in Figure 6.4(a-b).

6.4.2 Elastic Properties of Diatom Shell Components

The elastic moduli obtained in this work are in contrast to previously reported elastic moduli for *Coscinodiscus* sp. between 0.06-0.53 GPa [286] obtained from AFM indentation as well as

results reporting differences in mechanical properties between different components of the diatom shell. The low values and variance reported in previous studies are most likely due to movement or deflection of the frustule during testing and differences in compliance between loading the diatom axially and radially.

The similarity in the elastic properties between the basal plate and the girdle band observed in this study suggests that they are mechanically equivalent composite materials. Swift and Wheeler estimated that 20-40% of the dry weight inside the diatom silica valves is protein and carbohydrate. Kröger, et al. reported that the silica precipitated from *in vitro* studies of silica-depositing long-chain polyamines extracted from a diatom frustule had 1.25 g of SiO_2 per 1 g of polyamine[300]. Using the density of 2 g/cm^3 for silica and 0.8 g/cm^3 for the organic material in the diatoms studied here[309], we estimate the volumetric fraction of silica to be between 37.45 and 66.67%.

The rule of mixtures can provide an upper bound for the elastic modulus of the composite material. The expression for the composite modulus is given by:

$$E_c = fE_s + (1 - f)E_o \tag{6.5}$$

where f is the volume fraction of silica and E_s and E_o are the elastic moduli of the silica and organic component, respectively. It is reasonable to assume that the elastic modulus of the organic component is significantly lower than that of the silica; applying Equation 6.5 to the estimated range of volume fractions predicts the composite modulus to be between 26.2-46.7

GPa, consistent with the values reported here and similar to synthetic bio-silica composites such as Bioglass®45S5 (45% SiO_2 by weight) at 35 GPa [310].

6.4.3 Differentiation of frustules layers in mechanical response

Figure 6.6 shows the fractured surface of a representative bending test sample. Figures 6.6(a-b) show the path of crack propagation across the basal plate and the cribrum. Bending induces a compressive stress along the inner edge of the beam, abutting the indenter head, and a tensile stress along the outer edge, which is likely where the crack initiated. It appears that a central pore present in the basal plate (indicated by the blue arrow) and the cribrum (indicated by the red arrow) served as a stress concentrator and the crack nucleation site because it is close to the location of maximum bending moment. Within the cribrum, the crack traveled upward towards a cluster of pores beneath the applied load, and its trajectory continued through a series of these pores upward, tracing a path between stress concentrations (Figure 6.6(a)). The post-deformation crack surface shown in the inset of Figure 6.6(a) illustrates that the pores acted as perforations for the crack propagation. In the basal plate (Figure 6.6(b)) the crack propagated upward, bending slightly to follow the path of the crack within the cribrum. These paths diverge when the crack propagating through the basal plate encounters a foramen near the top edge of the beam. Instead of traveling through the pore, the crack is deflected around the pore. The foramina differ from the cribrum pores in that they have a raised rim around the circumference of the pore. Our experiments revealed that the pores in

the cribrum act as stress concentrators and fail by crack propagation while the rim reinforcements in the foramina appear to shield them against failure. This may shed light on the differentiation in function between the basal plate and the cribrum: the resilient pores in the basal plate may have a primarily structural function, while the pores of the cribrum and cribellum may serve more in the capacity of resource acquisition.

6.4.4 Strength vs. Relative Density

The average failure stress was 1.1 ± 0.3 GPa at a strain of $3.5\pm0.7\%$; with variations up to 250 MPa, which appear to be partly related to the distribution of pores in the beam. The highest stresses occurred in samples that lacked foramen segments along the bottom edge of the testing beam. Samples that failed at lower stresses had foramen segments, which suggests that their role in strengthening the diatom against stress concentration does not prevent them from serving as the weak points for failure along the free edge when the beam is subjected to bending. The average relative density of the beam samples used in this study, as calculated from direct volume measurements taken in the SEM, is 30.1%. Expanded discussion of the calculation of relative density is provided in the supplemental material. Using the density of bulk silica at 2210 kg/m^3, which provides the upper bound for the constituent material density, gives the frustule material a specific strength of 1702 kN-m/kg, a value well above those of other natural cellular, composite and silk materials including bamboo (693 kN-m/kg), mollusk shell (127 kN-m/kg) [311,312] and spider silk (1000 kN-m/kg) [313].

Figure 6.7 shows an Ashby plot of strength vs. density for several natural biomaterials [312]. We find that the diatom frustule occupies a previously-untapped space above the upper limit of natural cellular materials and has strengths comparable to the strongest natural polymers but at a lower density [312]. We attribute this high specific strength to the honeycomb architecture combined with a low density of flaws in the constituent material. The TEM image in Figure 6.4(a) shows no visible defects or flaws down to the estimated contrast roughness of ~2 nm in the nanocrystalline layer within the basal plate.
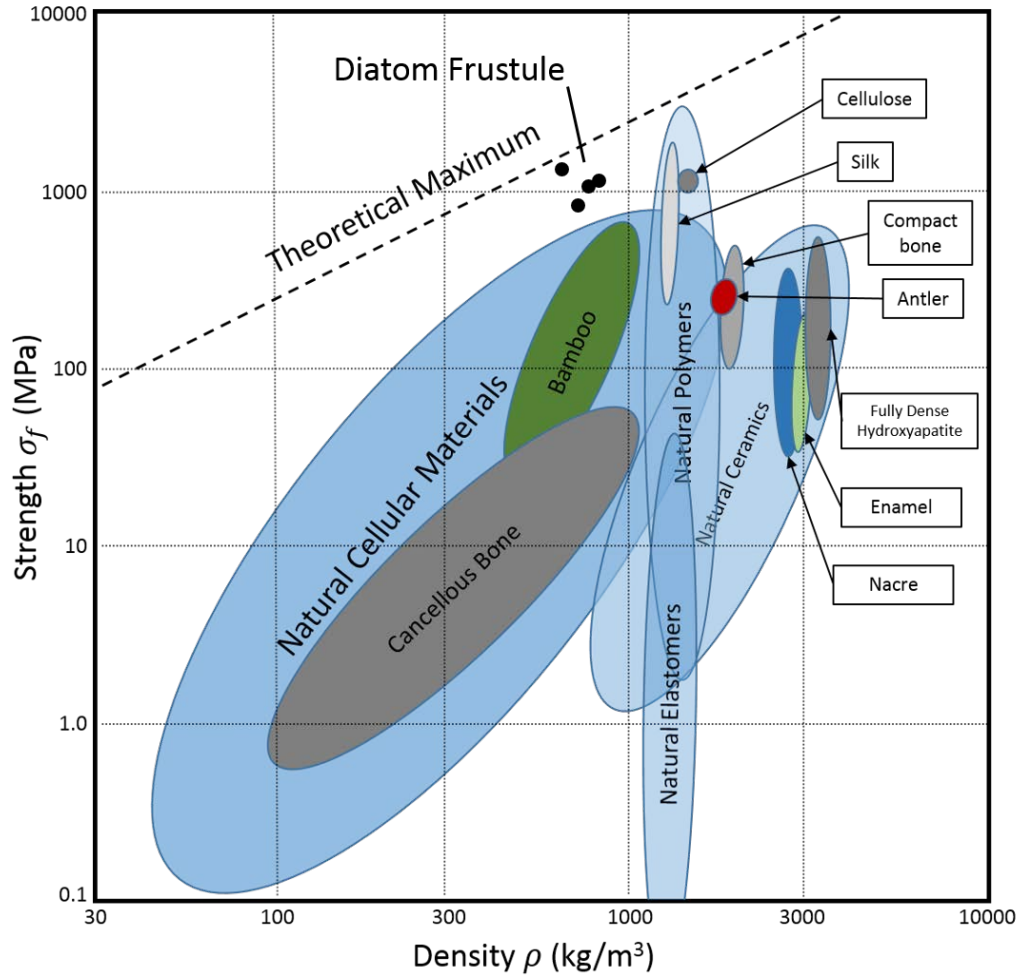
Figure 6.7 Ashby plot of strength versus density for naturally-occurring biological materials[21]. Diatom frustule samples show specific strengths above other reported cellular materials and are comparable to the strongest natural polymers. The theoretical maximum is determined by extrapolation of the strength and density of diamond.

This strength is still well below theoretical, in contrast to the strengths of synthesized high-purity silica nanowires that attain near-theoretical tensile strengths between 10-25 GPa [314]. This is likely because the frustule is a silica composite rather than pure silica. Within the last decade, much research has been dedicated to elucidate the composite nature of the frustule, with some studies revealing the presence and function of species-specific biopolymers within the frustule [315]. *In vitro* studies have shown that these biopolymers aid in polymerization and flocculation of silica particles [316]. Among the studied biopolymers, *Coscinodiscus* appears to exclusively contain long-chain polyamines (LCPAs) with reported molecular masses ranging between 600-1500 Da [300,315]. The exact distribution of silica and organic material within the frustule has not been experimentally verified, in the samples studied here, it appears to be tightly bound to the silica within the frustule because it survived the cleaning process to remove the organic cellular material. Further evidence for these tight, likely chemical bonds is that active LCPAs were recovered from fossilized diatomaceous material [309,317]. A proposed mechanism for the promotion of silica precipitation by LCPAs is the presence of alternating protonated and non-protonated tertiary amine groups in the polyamine chains, which form strong hydrogen bonds to silicic acid and facilitate the Si-O bond formation [318]. Such a mechanism suggests that interactions in the composite material are through hydrogen bonding between silica and organic phases and through covalent bonding within the silica. Failure in the biosilica composite most likely occurs at the weaker hydrogen bonds between the silica and organic material.

6.4.5 Stress Distribution Within Frustule Layers

The presence of an architecture within the diatom design results in a heterogeneous stress distribution within the frustule. Figure 6.8 shows the Mises stress distribution at the maximum bending strain of the simulated FEM beam (b and e) along the bottom edge of the cribrum and basal plates (c and f). The Mises stress of a solid beam at similar strain is shown as a black line for comparison. Within the cribrum, some thin sections surrounding the pores show local stress concentrations, manifested as two symmetric peaks ~±0.12 away from the center and one peak -2.2 away from the center. In the rest of the sample, the stresses remain below those in the solid beam. This is likely because the multiple pores present along the bottom edge are unable to sustain high stresses along this edge. Within the basal plate, the stress distribution closely follows that in the solid beam and increases towards the center of the beam. Near the center, the presence of a reinforced foramen results in a local reduction of stress. Local fluctuations in the stress distribution within both layers likely stem from the presence of pores or locations where the areolae walls intersect the cribrum or the basal plate.

Figure 6.9(a-b) show the Mises stress distribution within the areolae layer. This distribution shows that the stresses attained in the areola walls are less than those in the cribrum and in the basal plate. Within the center of the areolae walls, stresses are up to an order of magnitude lower than those in the cribrum and in the basal plate, and near the intersection with either outer layer, the stresses in the areolae are approximately half of the maximum stresses

observed in the cribrum and in the basal plate. At the locations where the areolae walls intersect the outer layers, the major contribution to Mises stress comes from the shear stresses, which suggests that under bending, the areolae is not contributing significantly to the mechanical response, and maximum Mises stresses occur around the pores in the cribrum and the foramen within the basal plate.
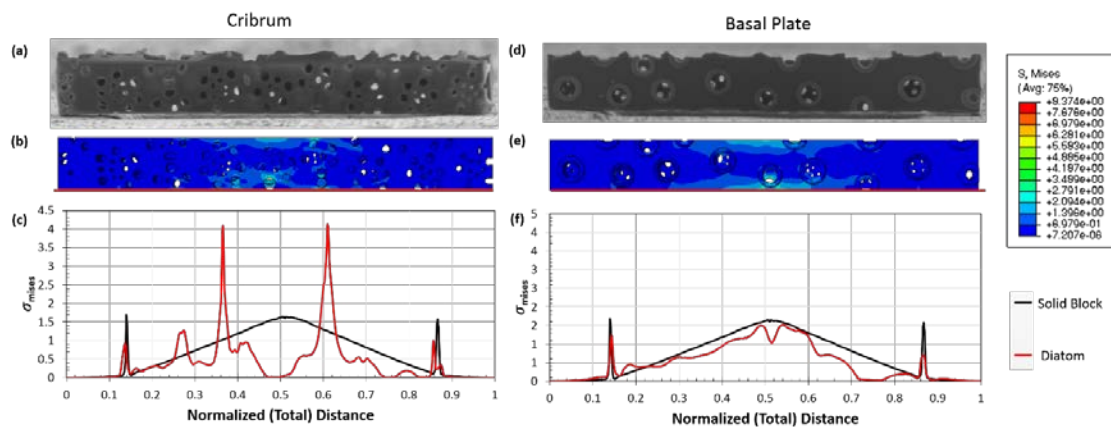
Figure 6.8 FEA simulation of the von Mises stress in diatom frustule samples during the bending experiments. (a,d) SEM imaged of the cribrum layer and the basal plate of a bending sample. (b,e) The corresponding von Mises stress distribution from FEM simulations. (c,f) Variation in stress along the bottom edge, with the stress of a solid beam at equivalent strain shown in black for comparison. It appears that the variation in stress in the basal plate follows that of the solid beam more closely than in the cribrum
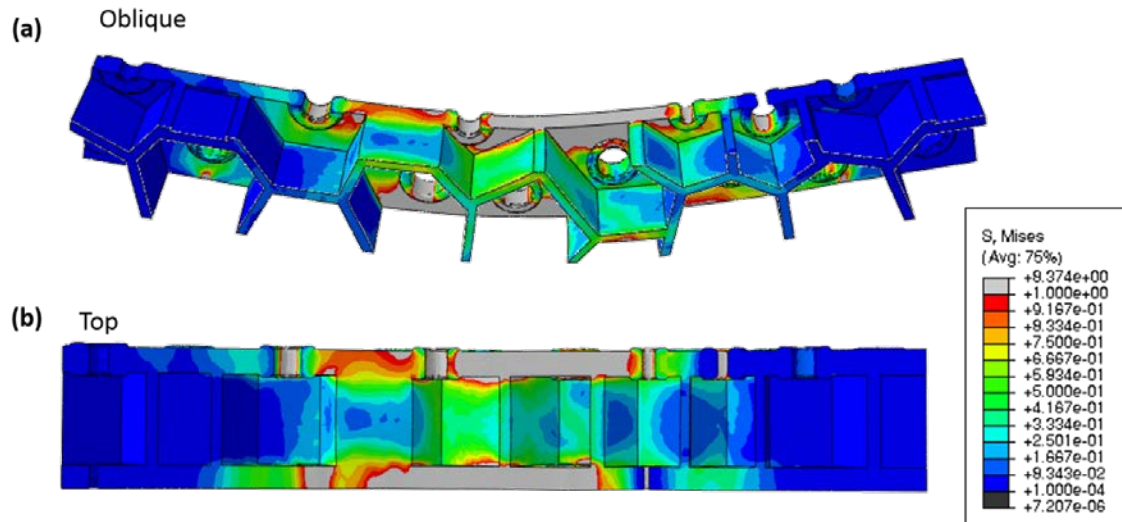
Figure 6.9 Stress distribution inside the diatom frustule and the correlation with microstructural features. von Mises stress distribution throughout the bending beam in an (a) oblique view to highlight the stress distribution in the areolae walls and (b) top down view

6.4 Summary

We used *in-situ* three-point bending and nanoindentation experiments to investigate the mechanical properties and fracture behavior of the diatom *Coscinodiscus* sp. frustule. These experiments disclosed similarities in the elastic properties of the biosilica found in the frustule and in the girdle band, with average modulus from three-point bending tests of 36.4±8.3 GPa. We discovered that the frustule has an unprecedentedly high specific strength, exceeding that of all other reported natural biomaterials, which we attribute to the

combination of the honeycomb sandwich plate architecture and extremely low flaw density in the constituent biosilica. TEM analysis of the frustule revealed that it is almost entirely an amorphous, solid material, with some local regions displaying a nanocrystalline microstructure. Analysis of crack propagation at failure provides strong evidence for the biofunctional differentiation between the frustule layers, with foramen deflecting crack propagation and cribrum layer seen to fail along its pores. FEM simulations convey that most of the applied stress is supported by the basal plate and that the areolae wall do not contribute significantly to bearing load. These results provide useful insights towards understanding the extreme resilience of hard biological materials to failure and aid in efficient design of new classes of bio-inspired, low-density and high-strength materials.

Chapter 7 : Capturing the Geometry, Microstructure and Mechanical Properties of Marine Diatom Frustules Using Nanoscale 3-D Silica Structures

In Chapter 6 we investigated mechanical properties of diatom frustules, and found out that by utilizing a unique combination of microstructure and hierarchical design, diatoms can achieve extraordinary strength-to-density ratio with very simple material building blocks. In this chapter, we explore the possibility to replicate the microstructure and design of diatom frustules using two-photon lithography. We will show that by using cyclohexyl polyhedral oligomeric silsesquioxanes (POSS), it is possible to build 1:1 replicas of diatom frustules that fully capture their microstructure and mechanical properties. The similarity between natural diatom frustules and these POSS structures are then demonstrated in *in situ* fracture experiments on the two, that show very similar results.

7.1 Introduction

As discussed in Chapter 5, diatoms are single-cell algae that have intricate silica/organic composite shells that were formed at mild temperature and pressure conditions[250]; their

evolutionary design has long fascinated the scientific community. Diatoms are generally classified into two groups based on their symmetry: centric diatoms have radial symmetry[281], whereas pennate diatoms have bilateral symmetry[286]. Shells of the centric species consist of a top and a bottom halves called frustules and a narrow connecting part, called a girdle band, in a Petri-dish configuration. Figure 7.1(a) shows an SEM image of a frustule of centric species *coscinodiscus sp.*, with distinct radially-distributed pores around the center. Figure 7.1(b) shows that each frustule shell is composed of two parallel thin wall layers populated with pores of varying sizes and arrangements that are connected to each other by hexagonal, cookie-cutter like walls.
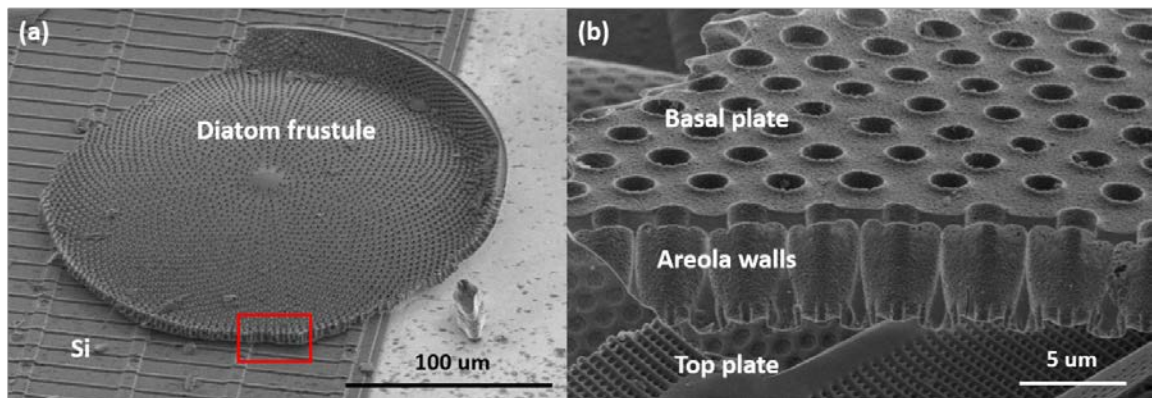
Figure 7.1 SEM images the *coscinodiscus sp.* frustule samples used in this work. (a) one half of *Coscinodiscus sp.* frustule on a Si substrate. (b) a zoomed-in view of the square region depicted in (a) showing the cross-section of the frustule and the double-wall structure

Various theories have been proposed that describe the evolutionary functions of the frustule geometries, including nutrient acquisition, control of diatom sinking rate, control of turbulent flow around the cell, and protection from grazing and viral attack[278,282]. Some of these theories argue that the silica, which comprises the diatoms, is very stiff, which is necessary to protect them against predator attacks, while the pores and the double-wall geometry lowers density and ensures buoyancy[285]. The protective function of the diatom frustules is reflected in the variation in wall thickness observed in the same diatom species living in environments with varying degree of predator presence[280]. Several studies have characterized the mechanical properties of diatom frustules with the aim to understand how they utilize both the hierarchical geometry and the underlying material microstructure in their evolutionary design. Modulus, hardness and failure strength for different diatom species have been reported as gleaned from different experimental techniques such as nanoindentation[284], AFM probing[283,286], and bending by glass micro-needle[285]. The modulus and the hardness reported in these studies vary significantly across different diatom species, from 0.35–22.4 GPa for the modulus and from 0.06–12 GPa for hardness. One potential reason for such variations is the inability to separate material from structural level contributions to the frustules' mechanical properties as limited by the testing methods. In Chapter 7, we isolated the structural and the material contribution to modulus and strength for frustules of coscinodiscus sp. using nanoindentation and 3-point beam bending experiments and

reported a Young's modulus of 36.4 ± 8.3 GPa and a specific strength of 1.1 ± 0.3 GPa, which represents the highest specific strength of all reported hard biological materials at that time[298]. We attributed the exceptional mechanical properties and simultaneous light weight of diatoms to their efficient geometrical design and a lack of flaws in the biosilica that comprises them.[298]

Additional questions remain regarding how much the various features in the diatom frustules, for example pore shape, size, and placement, as well as the wall height/thickness, contribute to their overall mechanical properties. Answers to these questions can provide insights into the origins of evolutionary architectures in hard biomaterials and help provide a pathway to mimic and optimize bio-inspired engineered structures, for example in a new class of hierarchical structural metamaterials[11]. To begin answering these questions, it is necessary to develop a reliable synthetic method to replicate diatoms and other hard biological layers which are capable of simultaneously capturing the material level properties, the dimensions, and the structural topology.

Cyclohexyl polyhedral oligomeric silsesquioxanes (POSS) is seeing increasing use for photonic applications[320]. The structure of POSS consists of silicon-carbon cages surrounded by short carbon chains which can be functionalized by different groups. When heated in O_2, the carbon and organic groups would react with O_2, and the cages would be converted into amorphous silica.[320,321] Such transformation from polymer resin to amorphous silica makes POSS an ideal candidate for the two-photon lithography

(TPL) process, which enables fabrication of 3-D structures at the nanometer-micrometer scale using different functionalized polymer resins.[1,297]

In this work we demonstrate using POSS mixture and TPL direct laser writing to create synthetic diatoms with geometry, dimensions, and materials equivalent to those of the natural species. TEM show that these synthetic samples have an amorphous microstructure like natural diatoms, and *in-situ* beam bending experiments on the excised sections of the overall structure show that the synthetic samples have an elastic modulus of 20.2 ± 2.6 GPa and a strength of 1.70 ± 0.11 mN both of which are virtually equivalent to those of the *coscinodiscus sp.* frustules. We also report fracture toughness K_{1C} of 0.78 ± 0.1 MPa.m$^{1/2}$ and 1.05 ± 0.08 MPa.m$^{1/2}$ for both natural and synthetic samples as determined from single edge notched bending (SENB) fracture experiments, which reveal that the double-wall geometry of diatom frustules arrests crack propagation.

7.2 Methods

Coscinodiscus sp. sample: Live *Coscinodiscus sp.* culture were purchased commercially (Carolina Biological Supply). Samples were washed in Milli-Q (MQ) water, centrifuged in a solution of 3 mL H_2O_2 and 1 mL HCl, and finally rinsed with MQ water and ethanol. This treatment was intended to remove the cellular organic material and to separate the frustule half-shells and girdle band from one another; this type of treatment also unintentionally

fractured many of the components. Samples were stored in methanol before nanomechanical experiments. SEM samples were prepared by applying a drop of this methanol solution containing the cleaned diatoms onto a silicon chip and then allowing the methanol to evaporate in air.

Diatom Sample fabrication: Natural diatom beams of dimension 5 µm x 7 µm x 30 µm (Height x Width x Length) were extracted from intact *coscinodiscus sp.* samples using FIB lift-out technique described by Aitken, et al[298]. They were transferred onto the POSS stages using a micro-manipulator and secured using Ion-assisted Pt deposition. The whole process takes place in one step inside an SEM chamber to avoid contamination.3D renditions of these beams were then used as templates for the design and fabrication of the synthetic samples.

POSS sample fabrication: The POSS photoresist were made by mixing in photo-initiator to commercial Epoxy POSS cage mixture (EP0408, $(C_8H_{13}O)_n(SiO_{1.5})_n$, n=8,10 or 12, FW=1772.73, Hybrid Plastic) and centrifuging. The resulting photoresist was patterned into different 3-D structures using layer-by-layer TPL (Nanoscribe GmbH). The polymer POSS structures were then baked in an O_2 environment at 400 °C for 1 hour as described by Moon, et al.[320] to remove the organic components.

50 µm x 50 µm x 20-µm-thick POSS plates were written on Si substrates to conduct nanoindentation and Fourier transform infrared spectroscopy (FTIR).

For the beam bending experiments, each sample system consisted of a solid pedestal and a beam sample fixed on top. The pedestals were solid rectangular blocks with the dimensions of 50 µm x70 µm 100 µm (Height x Width x Length) and had two smaller posts on top, with dimensions of 10 µm x 10 µm x 10 µm, spaced 30 µm apart. Beams of the same dimension (5 µm x 7 µm x 30 µm (Height x Width x Length)) and geometry of extracted diatom samples were written in the same step on top of the posts.

TEM sample fabrication: Site-specific sections were excised from the baked POSS samples to analyze the atomic-level microstructure. These excised sections had dimensions of 5 µm x 5 µm x 1 µm (Length x Height x Thickness) and were thinned down to a thickness of 100 nm using progressively lower currents in the FIB,

TEM analysis: Microstructural analysis was performed via transmission electron microscopy (FEI Tecnai F30) at an accelerating voltage of 300 kV. Standard-less energy dispersive spectroscopy (INCA EDX; Oxford Instruments) was used to investigate the local elemental composition of the sample.

Nanoindentation: Nanoindentation was performed on 50 µm x 50 µm x 30 µm-thick POSS films on Si substrates in a nanoindenter [G200, Agilent] using a Berkovich diamond tip under a constant nominal displacement rate of 10 nm/s. The indents were positioned in the center of each sample on 3-by-3 grids equally spaced at 5 µm and were 1-µm deep. Elastic moduli were calculated using the method of Oliver and Pharr.[83]

Three-point bending experiments: Bending tests were performed in a custom-made in situ SEM (FEI Quanta) with a nanomechanical module, InSEM (Nanomechanics Inc.). A wedge-shaped diamond tip with a 5 µm tip radius was used to apply the load while maintaining a constant nominal displacement rate of 5 nm/s at the midpoint of each beam until failure. Load and displacement were continuously measured at a rate of 500 Hz with a simultaneous video capture of the deformation process.

Fracture experiments: Fracture experiments for POSS and diatom beams were carried out following the ASTM guidelines for SENB tests. The span of the beams was 30 µm for all samples, with a dimension ratio of 30:5:7 (S:B:W). A single notch was milled into the basal plate in each sample underneath the loading direction using FIB. The notch sizes were 1 µm (L) x 100 nm (W), with slight variations caused by drifting and spreading of the ion beam. Samples were loaded at a nominal displacement rate of 5nm/s to maintain the quasi-static conditions until crack initiation. All experiments were performed *in situ,* inside of a custom-made instrument that is comprised of a nanomechanical module inside of an SEM chamber, to observe the crack initiation and growth.

Fracture toughness values K_{1C} were calculated for each sample following ASTM 1820-15, using the notch length as initial crack length. Since a roller boundary condition was not feasible at such length scale, all beams were fabricated to be 50% longer than the distance

between posts and secured to the them on both ends using Pt (diatom samples) or written over them (POSS samples).

7.3 Results

7.2.1 Characterization and Morphology

Figure 7.2 shows synthetic diatom beams secured on solid POSS supports. The stages and the beam samples were written in the POSS photoresist using a layer-by-layer recipe in the Nanoscribe. These beams were written on top of the twin posts at the center of the pedestals to minimize distortion from any possible residual stress generated from the heating process[320,322]. We observed an up to 40% decrease in sample volume after the carbon groups reacted with O_2 during the baking process. By detaching the samples from the POSS-Si interface, the distortion and delamination from the substrate were virtually non-existent, as shown by SEM images of the same sample as-written (Figure 7.2(b)) and after baking in O_2 for 1 hour (Figure 7.2(c)). The rectangular shadow on the Si substrate shows the original footprint of the support and clearly conveys the amount of shrinking from the baking process.
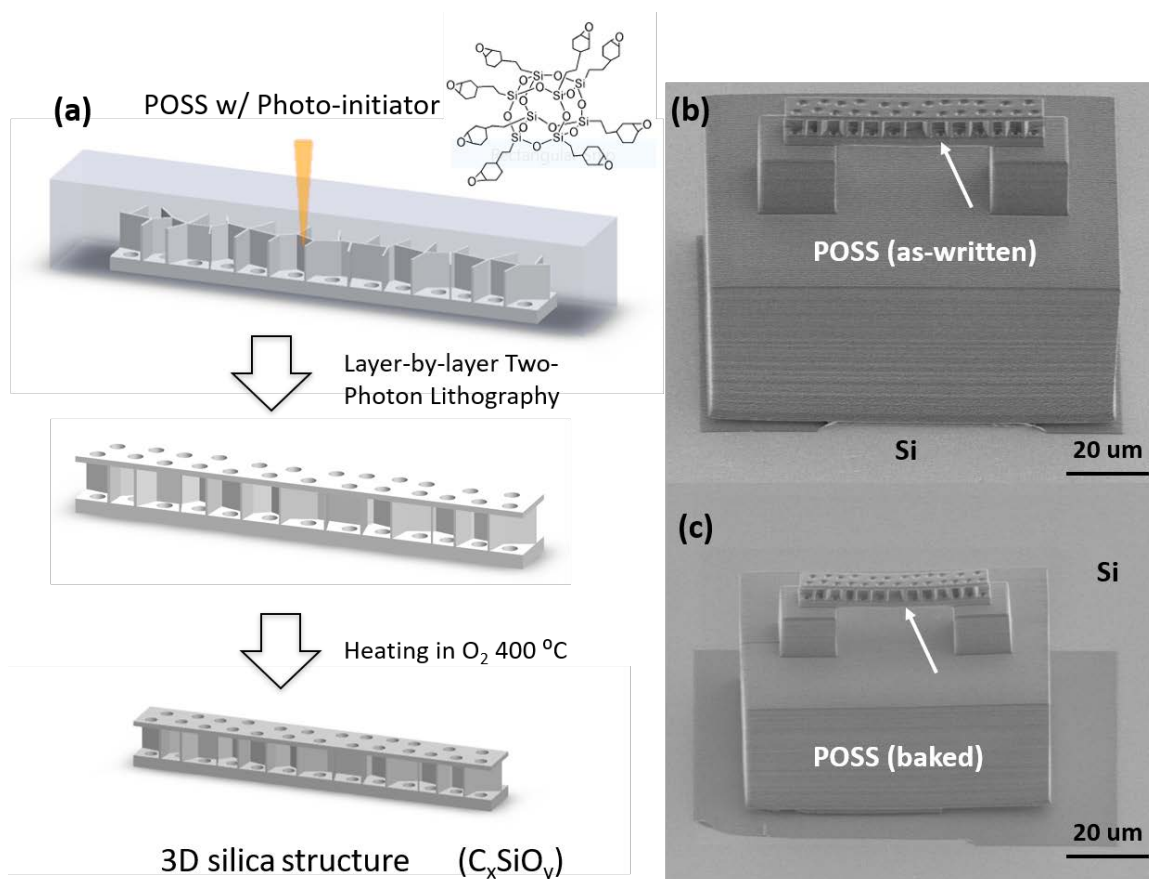
Figure 7.2 Schematics of the sample fabrication process and SEM images of the as-written and baked POSS samples. (a) Schematic of the two-photon lithography process to fabricate the synthetic diatom beams. The change in sample dimensions corresponds to the shrinking of the POSS after being baked in O_2. (b) SEM image of an as-written POSS sample. Each beam sample was written on a solid POSS pedestal (pointed to by an arrow) on a Si substrate. (c) SEM image of the same sample shown in (b) after baking in O_2. The visible rectangular shadow on the Si substrate shows the original footprint of the pedestal.

Figure. 7.3(a) shows representative FTIR spectra of POSS samples as-fabricated and after heating in O_2 at 400 ºC for one hour. Different carbon and -OH peaks were identified across a wavelength range of 600-6000 cm^{-1}. The -C-O-C- peak (1500 cm^{-1}) and -CH_2 peak (3200 cm^{-1}) vanished in baked samples, and the intensity for the -C=O peak (2500 cm^{-1}) was reduced ~8x. This reduction in the carbon peaks indicate that the carbon content was significantly reduced in baked samples as a result of the oxidation process at high temperature. These results are similar to those from previous FTIR analyses on functionalized POSS epoxy, where the samples were baked at 350 ºC and showed a similar reduction in carbon content[321]. A trace amount of carbon remained, as indicated by the residual -C=O peak at 2500 cm^{-1}, although it is difficult to quantify the exact change in carbon content because the carbon peaks overlap with the oxygen ones in most common spectroscopy techniques. This analysis indicates that the baked POSS samples contain mostly SiO_2 with some residual carbon chains. The presence of carbon chains is also reflected in a greater compliance of the POSS samples as revealed by nanoindentation, with a reduced modulus of 20.2 ± 2.6 GPa compared with that reported value for pure silica (70 GPa[323]).
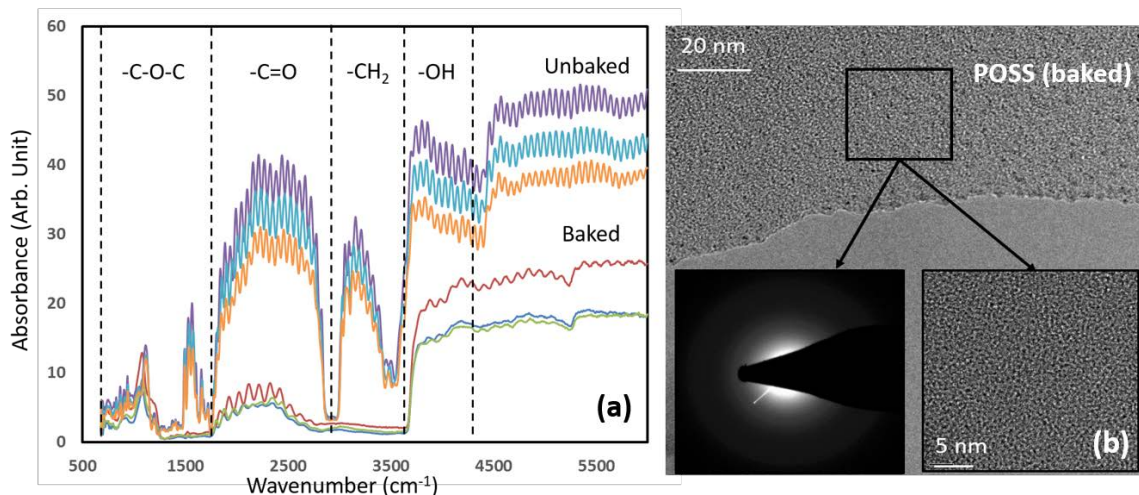
Figure 7.3 Characterization of the POSS microstructure, before and after baking. (a): FTIR spectra of POSS samples, as-written (unbaked) and baked in O_2 for 1 hour (baked). Dashed lines show regions for the corresponding peaks. (b): TEM micrograph of baked POSS. Insert shows high-resolution image and diffraction pattern of the highlighted area.

Figure 7.3(b) shows a bright field TEM micrograph of a representative region in baked POSS. The sample appeared amorphous except for traces of Ga ion damage near the edge from the FIB thinning process[298]. Inserts (Figure. 7.3(b1) and (b2)) show a high-resolution image and a diffraction pattern from the boxed region, which revealed no discernible features or diffraction spots, which suggests a fully amorphous material.

7.3.2 Mechanical Experiments

We conducted nanoindentation on the natural and the synthetic diatom samples to compare their stiffness and strength using a similar procedure reported in our previous work on *coscinodiscus sp.* frustules[298]. Figure 7.4(a) shows some representative load-displacement data from nanoindentation experiments and conveys that the slope of all unloading segments, which is directly related to stiffness, was the same for all samples. Indentation depths differed slightly from sample to sample, likely caused by the variations in establishing initial contact. We calculated the reduced modulus from the load-displacement data for all samples using the Oliver-Pharr method[83] ; these values are presented alongside the load-displacement data in Figure. 7.4(a). This data shows that the synthetic samples have an average modulus of 20.2 ± 2.6 GPa, which is ~30% lower compared with that of *coscinodiscus sp.* frustules[298], and over ~2x stiffer than that of the unbaked acrylic POSS[322]. The variation among tests and across different synthetic samples was relatively low, at ~10%, which is significantly lower than that of ~25% among the natural diatom samples[298]. This suggests the fabrication and baking process to create synthetic diatoms is self-consistent and is able to produce samples that have reproducible silica/organic ratios.
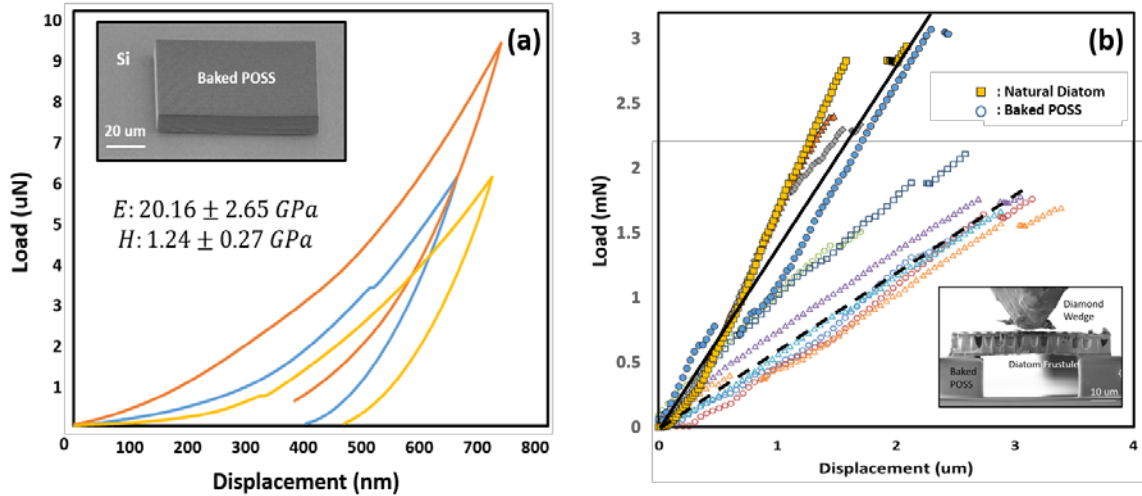
Figure 7.4 Beam bending and nanoindentation experiments on baked POSS samples. (a): Representative nanoindentation load-displacement data from experiments on the synthetic diatoms, with the reduced modulus and hardness obtained from the unloading portion of each data set. Insert shows a representative SEM image of a thin film sample used for nanoindentation. (b): representative load-displacement data from beam bending tests of natural (solid symbols) and synthetic (open symbols) diatom samples. FEM-simulated Load-displacement response is represented by the solid line (natural diatoms) and the dashed line (synthetic samples). The inset shows an SEM image of the diatom sample glued onto the stage before the experiment.

Bending experiments were performed *in situ* in an SEM equipped with a nanoindenter arm. The beams were oriented such that the tip comes into contact with the sample at the thinner top plate, which is meant to represent the type of applied forces that diatoms would experience in nature[280,285]. The POSS sample assemblies were fabricated as one monolithic

structure, such that the ends of the beams were connected to the posts on the pedestal. The natural diatom samples were prepared by FIB-lift out from *Coscinodiscus sp.* frustules and were fixed on the separately written POSS test stages in the same orientation using ion-assisted Pt deposition. These setups create fixed boundary conditions for both synthetic and natural samples.

Although the distortion from baking is minimized at the sample beams, it is common for the stage to break free from the substrate after baking, as shown by the gap in Figure 7.2(c). During the in-situ bending and fracture experiments, the load was carefully applied at the center of the sample-stage assembly, and the detachment of the stage from the substrate had a minimal effect on the mechanical response after full contact has been established.

Figure 7.4(b) shows the representative load-displacement data for the experiments performed on the synthetic and natural diatom beams, as well as the FEA simulations. It conveys that all samples first deformed elastically until brittle failure at an average displacement of 2.62 ± 0.15 µm for the synthetic samples and of 1.85 ± 0.22 µm for the natural ones, at the average failure load of 1.70 ± 0.11 mN for the former and 2.81 ± 0.15 for the latter.

Figure 7.4(b) also reveals that aside from the initial loading segments, where the contact was first established, the finite element model predicts the loading slopes and the final load in the elastic regime very close to the experimental data.

7.3.3 Finite Element Simulation

The stress-strain relationships during bending experiments reported in our previous work ignored the contribution of the moment of inertia that arises from the honeycomb areola walls[298]. This assumption does not hold for the sample loading orientation in this work. Instead we use finite element analysis (FEA) to calculate the stress in the samples. We constructed FEA models based on the 3D drawings of the samples and using the material properties of POSS and natural biosilica gleaned from nanoindentation. We simulated a rigid circular diamond roller with a diameter of 5 µm to represent the diamond wedge tip. The simulated sample-stage assembly was pinned at the plane of contact with the substrate and frictionless sliding was assigned between the roller, the beam and the stage. A total displacement of 3.0 µm was prescribed to the diamond roller in a quasi-static manner to represent the average displacement of 2.62 ± 0.15 µm at failure based on the experiments.

Figure 7.5(a) shows the overall stress distribution in the sample and reveals that the thinner areola walls experienced high compressive stress, with an average Mises stress of ~ 600 MPa, a factor of ~2 higher than that in the top and basal plates. Figure 7.5(b) conveys that the model predicts the highest stress concentration to occur around the pores in the bottom plate near the load-line, with the stress reaching ~3x of the average stress in the basal plate.
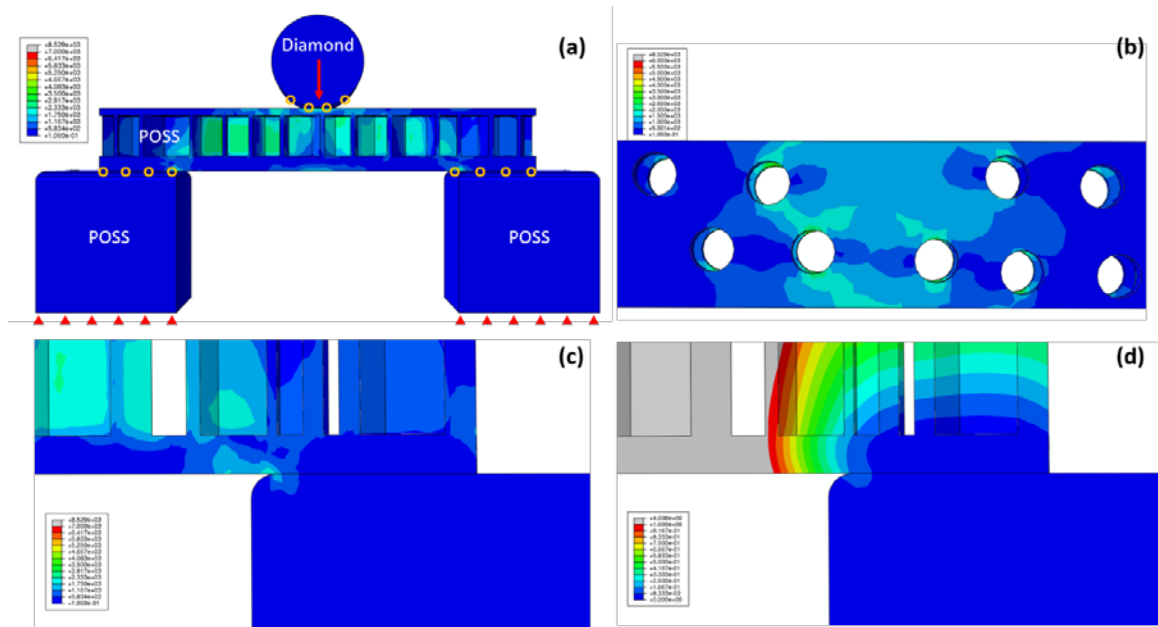
Figure 7.5 FEA simulation of the bending experiments. (a): Schematic of the finite element simulation of the beam bending test with overlay of Mises stress contour. The two POSS supports were fixed in space and the diamond wedge was prescribed the displacement at failure from beam bending experiments. Contact pairs were assigned between the wedge, sample and the supports. (b) Mises stress contour in the basal plate. The red line indicates the position of the loading line on the top plate. (c) Mises stress contour around the sample-support contact. (d) deformation gradient around the sample-support contact.

7.3.4 Fracture Experiments

A high fracture toughness is crucial to the functionality and survival of diatoms. The brittle nature of the biosilica coupled with the abundance of stress concentrators in the form of pores calls for their structural design to provide one or more toughening

mechanisms. Very few literature reports on fracture properties at the scale of diatom frustules exist because most work on fracture focuses on structural materials on the macroscopic scale.[246]

We explore fracture toughness, K_{1C}, of the *Coscinodiscus sp.* frustules and the synthetic samples by following the guidelines for SENB geometries according to ASTM standards E1820[324]. Fracture beams were fabricated with dimensions of 30(S) x 5(W) x 7(B) (µm) following the same procedure as the samples for bending experiments. The synthetic samples were fabricated directly on the posts on top of the pedestals and the natural diatom samples were extracted from the intact frustules using the lift out process described in in Aitken, et al.[298]. These experimental artifacts gave rise to slight dimensional differences in the notch and sample geometry that were accounted for in the toughness calculation.

Figure. 7.6(a) shows SEM images of natural diatom and synthetic POSS samples before SENB fracture experiments. A total of 12 synthetic and 4 natural diatom samples were tested; in all cases a single crack initiated from the notch and propagated instantaneously through the beam cross-section. We could not achieve stable crack growth, which suggests a lack of microstructure-driven fracture suppression mechanisms. Fracture toughness K_{1C}, for all samples was calculated following ASTM Standard E-1820[324]:

$$K_{1C} = \left[\frac{PS}{BW^{\frac{3}{2}}}\right] f\left(\frac{a}{w}\right) \tag{7.1}$$

where S, W and B are the dimensions of the sample, the initial crack length a is taken as the notch length, and $f\left(\frac{a}{w}\right)$ is an empirical formula given by:

$$f\left(\frac{a}{w}\right) = \frac{3\left(\frac{a}{w}\right)^{\frac{1}{2}}\left[1.99-\left(\frac{a}{w}\right)\left(1-\frac{a}{w}\right)\left(2.15-3.93\left(\frac{a}{w}\right)+2.7\left(\frac{a}{w}\right)^{2}\right)\right]}{2\left(1+2\frac{a}{w}\right)\left(1-\frac{a}{w}\right)^{\frac{3}{2}}}$$

(7.2)
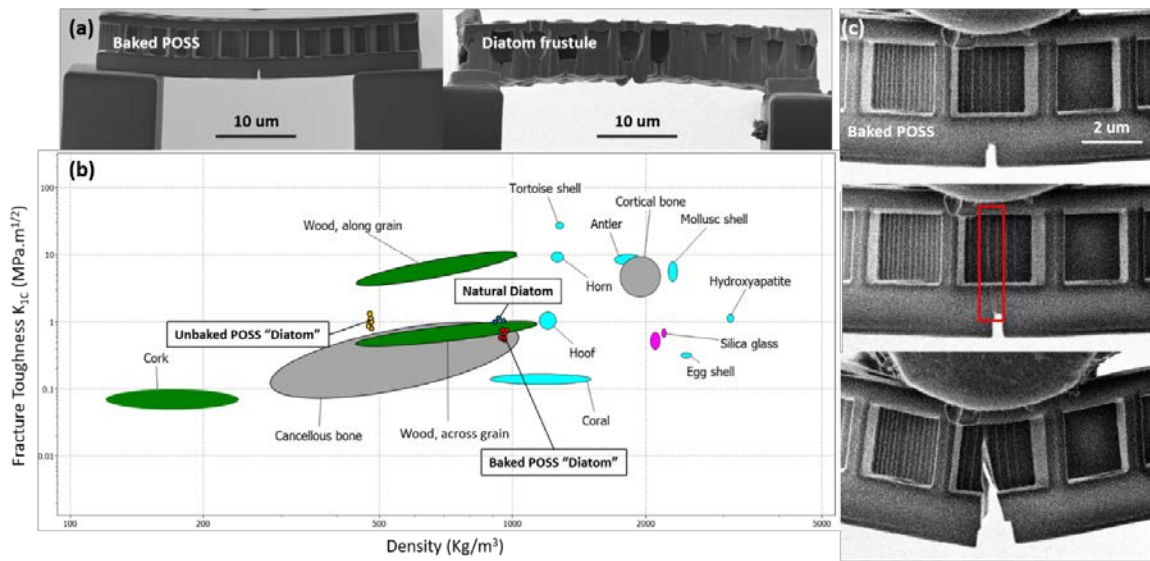
Figure 7.6 Fracture properties of baked POSS and natural diatom frustules. (a): SEM images of baked POSS (left) and diatom frustule (right) fracture samples on POSS stage. (b): fracture toughness as a function of density for selected hard biomaterials in an Ashby plot. Red, yellow and blue points indicate results from different POSS and diatom samples. Fracture toughness data was taken from references [19,30–34]. (c): Captures from a representative video of crack propagation in a POSS beam. From top to bottom: before crack initiation; after crack initiation, crack stopped at the top plate shown in red highlight; sample reloaded before fracture

Although the sample geometry conforms to ASTM standards, several requirements were relaxed because of the small sample size. These include: (1) The FIB milled notches as opposed to fatigue cracks (per ASTM recommendation) were used as the initial cracks; (2) the loading tip had a finite radius instead of an idealized line load; and (3) the sample boundaries were fixed instead of on rollers. The finite notch width in (1) would lead to over-estimation of the toughness[325]. At the scale of these samples, the FIB notches have a width of ~100 nm that is reasonably close to fatigue cracks, and the error from their finite width should be minimal. Baratta, et al discussed the error from wedge radius and boundary conditions in detail for large scale ceramics samples[325,326], and reported an up to 7% error that resulted from using the finite wedge radius as a function of beam span, and ~12% error from fixed boundary vs. ideal rollers for the silicon nitride beams. It is likely that these effects would be applicable to both natural and synthetic samples with the same dimensional ratio. These three sources of error would all lead to varying degree of over-estimation for the fracture toughness and are difficult to fully eliminate at such small scales. As a result, it is possible that the toughness determined via SENB experiments in this work would be higher as compared with bulk.

Figure 7.6 presents the toughness K_{1C} for the synthetic POSS (baked and as-written) and natural diatoms in a material property space. The density was calculated by taking the density of the fully dense POSS/silica and adjusting it by the relative density factor that accounts for the space-filling ratio of the diatom, as described in Chapter 6. All three

groups of samples, unbaked, baked, and natural, showed similar toughness values, with the natural diatom samples having the highest at 1.05 ± 0.08 MPa.m$^{1/2}$, which is ~20% higher than that of bulk silica (~0.8 MPa.m$^{1/2}$). These higher toughness values can be in part explained by the aforementioned deviation from ASTM requirements, while additional toughness contribution from the organic matrix of diatom frustules (and POSS) would also be a contributing factor.[316]

7.4 Discussion

7.4.1 Characterization of POSS Microstructure

The geometry of the POSS samples in both bending and fracture experiments was based on 3-D drawings of FIB-lifted *coscinodiscus sp.* beam samples, and were modified to fit the resolution of the TPL process. On the top plate of natural frustule samples, multiple ~100 nm-diameter pores are arranged in a radial pattern, whereas ~ 1 µm-diameter pores line the basal plate, their position in the plate corresponding to the radial pore-assemblies on the top plate[298] (Figure 7.1). In the POSS samples the radial pore-assemblies on the top plate were replaced by the ~ 1 µm pores as found on the basal plate, as shown in Figure 7.2. This lead to larger pore sizes (with fewer pores) in top plate of the synthetic diatom, and would likely lower its strength compared with the natural geometry. This effect is likely marginal because the difference in the total surface area occupied by the pores is only ~3% (natural diatoms 33%, synthetic diatoms 36%), and the hole positions remain the same. The top plate in natural

coscinodiscus sp. frustules are also ~2x thinner (800 nm) compared to the main load bearing basal plate (1.5 µm), which was replicated in the synthetic diatoms. This differentiation in plate thickness and in turn load-bearing capabilities further diminish the effect of changing the pore sizes and distribution in the less load-bearing top plate.

FTIR measurements in Figure 7.3 showed only residual amount of carbon after the baking process, and the TEM analysis revealed no distinctive features within the resulting silica-carbon compound, which suggests that baked POSS is an amorphous matrix consisting of silicon and carbon components. This amorphous microstructure of baked POSS is virtually identical to that of natural *coscinodiscus sp.* frustules shown by TEM analysis by Aitken, et al.[298]. Such a similarity in the atomic-level microstructure between the synthetic and the natural samples would likely translate to similar mechanical behaviors and mechanisms for the two systems.

7.4.2 Mechanical Properties of POSS Structures

In beam bending experiments, natural diatom beams failed at a load of 2.81 ± 0.15 mN, which is ~1.5 times higher than that of the synthetic ones. Since the geometry and microstructure of the natural and synthetic samples were largely identical, the different strength is likely a result of the greater stiffness of the diatom biosilica, as revealed in the nanoindentation experiments.

Natural diatom samples in the bending experiments were extracted from different frustules and have intrinsic variations in geometry, which could lead to variations in their load-displacement response in Figure 7.4. However, all synthetic samples were fabricated with the same template, yet they still exhibit ~ 10% variation in their final load/displacement values. This likely stemmed from variations in carbon content removed from the baking process, and from the variations in contact between the sample stage and substrate.

Aitken, et al. reported that diatom frustules have a strength 1.1 ± 0.3 GPa at a relatively low density of 2,210 kg/m^3, which were attributed to the geometrical design and the lack of flaws in the biosilica that comprises the diatom frustules[298]. This work reveals that the synthetic diatoms exhibit similar load-displacement response and failure strength during beam bending experiments, which suggests that they have mechanical properties that are similar to those of their natural counterparts.

From the FEA results in Figure 7.5, it is clear the pores are the highest stress concentrators in this loading orientation, as they did in the alternative orientation in our previous work[298]. The natural diatom samples there are raised grooves around each pore in the basal plate, likely to reinforce these stress concentrators. These grooves were not included in the POSS samples (and the finite element model) due to resolution limitations, which would lead to over-estimation of stress concentrations.

The FEA model also provided an intuitive view of the stress and deformation in the posts and the pedestal. Figure 7.5(c-d) shows the Mises stress and the displacements in one of the posts that the sample rested on at the moment of failure. The highest stress in the post occurs near the edge, similar to the Sneddon effect with a cantilever beam geometry[205]. We found the maximum Mises stress in the post to be ~100 MPa, ~20% of the average stress in the sample, and the maximum displacement was ~ 300 nm, which represents 5% of the overall prescribed displacement. These relatively low stress and displacement in the supports suggest that once they have been accounted for, the supports can be approximated as rigid boundaries. This additional compliance was accounted for in the load-displacement lines generated by the FEA model (Figure 7.4).

7.4.3 Fracture Toughness and Crack Arrestment in Diatom and POSS

Average toughness for baked synthetic beams was 0.78 ± 0.10 MPa.m$^{1/2}$, which is within 20% difference compared to the natural diatom samples. As was the case in Young's modulus and strength, the similarity in fracture toughness between the two material systems suggests that these samples share similar failure mechanism. Both materials are amorphous, with no notable toughening mechanisms at >10 nm scale, leading to similar toughness values. This lack of toughening mechanisms in the synthetic and natural diatoms is also apparent when compared with the toughness of the unbaked POSS samples, which had the same dimensions and test conditions. Average toughness of the unbaked samples was 0.93 ± 0.10

MPa.m$^{1/2}$, about 20% higher than that of the baked samples. The unbaked POSS has a density of 1.19 g/cm^3 [327] which is ~ 50% that of the baked POSS (approximated by silica in this case). The higher toughness at a lower density and stiffness of the unbaked samples is likely a result of additional toughening introduced by the ligands and carbon chains around POSS cages[246]. After the baking process most of these ligands and carbon chains were replaced with the amorphous, silica-like microstructure as found in baked POSS. This lead to baked POSS having a lower fracture toughness compared to as-written ones.

Our results show that unlike their specific strength which is one of the highest among hard bio-materials[298], diatom frustules have relatively modest toughness values compared with other hard biomaterials, such as bone or antlers. Such a lack of enhancement in toughness might be caused by the diatom's primitive nature, and that diatom frustules do not have a hierarchical complexity and toughening mechanisms at different length scale as observed in systems like cortical bone[265,277], elk antlers[273] and nacre[246]. Despite this, diatom frustules show strength and toughness that are similar to bulk silica at a much lower density ~ 30%. This might be a direct result of their structural design enhancing mechanical properties under the constraint of simple material and microstructure.

In 11 out of 12 synthetic and in 3 out of 4 natural diatom samples, crack propagation stopped when the crack tip reached the top plate, as shown by SEM video in Figure 7.6(c). Such phenomena can be explained by the I-beam characteristic of the frustule cross section. After

the initiation of the cracks, they propagate through the hexagonal areola walls that connect the top and bottom plates, where the cross-sectional area is small. The area and the amount of material increase significantly when cracks reach the top plate, and as a result the bending stiffness of the beam increases. This would lead to an increase in crack growth resistance and to the suppression of crack propagation, which has been shown in structural beams using finite element analysis[328]. Such phenomena would not translate to a higher K_{1C} or other toughness metrics but would help improve the protective functions of diatom frustules in nature. This is a prime example of how diatoms use their structural design to increase crack resistance without relying on the underlying material microstructure because the intrinsic biosilica is relatively homogeneous at the atomic scale[298] and does not possess microstructure mechanisms to prohibit crack initiation or blunt crack growth.

Hard biomaterials found in more advanced organisms, such as bone, nacre or bamboo[246], often rely on complex architecture in combination with nanocomposite-like microstructures to gain their mechanical resilience. Diatoms are much simpler organisms with a homogeneous, amorphous constituent material that comprises their frustules. As such all the microstructural-level toughening mechanisms are unavailable to them, and diatom frustules have to draw the entirety of their mechanical strength from structural design and architecture. Earlier reports have shown that this approach is highly effective in creating a lightweight, high strength structure[298]. With the experimental platform provided by POSS, we further demonstrated that diatom frustules utilize this same complex architecture to help resist crack

growth. This finding can potentially enable us to better optimize structures that are simultaneously mechanically resilient, and are comprised of relatively simple, easily reproducible materials.

7.5 Summary

We fabricated synthetic diatoms with two photon lithography direct laser writing using the geometry of natural diatom frustules as a model. After heating to 400 °C in O_2, the material used to fabricate these samples, POSS, possesses amorphous microstructure similar to that of the biosilica that comprises natural diatoms. Nanoindentation and beam bending experiments reveal the average Young's modulus of 20.2 ± 2.6 GPa and the strength of 1.70 ± 0.11 mN, which are on the same order of magnitude as the natural diatom frustules. These findings demonstrate that the synthetic structures successfully mimic natural diatom frustules at the material and structural level, while the two photon lithography technique used in the fabrication process provides full control of their structural design.

We performed fracture analysis on the natural diatom frustule and the biomimetic beam samples and found the average toughness to be 1.05 ± 0.08 MPa.m$^{1/2}$ for the natural samples and 0.78 ± 0.10 MPa.m$^{1/2}$ for the synthetic ones, which are within ~20% of bulk silica at roughly half the density. We also show that the double-wall honeycomb geometry of diatom frustules stops crack propagation at the top plate, which was consistently observed in both

types of samples. We attribute such properties to the structural design of diatom frustules. These hierarchical designs are integral to diatoms' protective functions and weight reduction, as they do not have access to complex microstructures and toughening mechanisms.

These results provide insights to how diatoms might utilize evolutionary design to enhance simple underlying material. The method to design and fabricate POSS structures can also provide a novel platform to developing a new class of bioinspired, low-density, and high-strength materials.

Chapter 8 : Conclusion and Outlook

Understanding the microstructures and the different mechanisms in which they affect properties of different material systems is at the core of a lot of work in materials science. This thesis considered two materials systems: $Cu(In,Ga)Se_2$ thin films and biosilica frustules of marine diatoms; and microstructural effects within each, with a focus on mechanical properties. This final chapter summarizes the findings presented in each chapter, as well as some general conclusions that can be drawn from these studies.

Chapters 2-4 presents a study of CIGS thin film solar cells. We first presented a historical survey of CIGS research in Chapter 2, and showcased the intrinsic material advantage of CIGS that garnered it significant attention from scientific community. We then discussed a few prominent deposition methods for CIGS, and highlighted that the current research is lacking fundamental understanding of how these methods affect film microstructure, and in turn, film properties.

Chapter 3 presents characterization and mechanical-properties studies of CIGS films from different deposition methods. We discovered that while the mechanical properties of the films, in particular stiffness and hardness, are comparable, there are significant differences in terms of grain structure as a result of the different methods. In particular, the cheaper sputter-selenization method lead to large variations in film grain size, and a multitude of

voids near the film/substrate contact. We further proposed that the voids and inhomogeneous grains would impede species diffusion in sputtered films, which will adversely affect their device efficiency.

Chapter 4 builds on the characterization results from Chapter 3, and further investigates the effects of film microstructure on species diffusion in CIGS. In particular, we focused on the diffusion of Na around the voids found in sputtered films, and found that solution passivation of TOP:S enhances Na diffusion, to the extent that it will bypass the microstructural defects such as voids or grain irregularities, and results in increased Na content at the surface of the films. We then conducted density functional theory calculations of Na defect energetics in CIGS, and showed that TOP:S indeed leads to a more preferable Na defect state at film surface, which creates a driving force for solid state diffusion, that supports the experimental findings.

Chapters 5-7 apply the similar characterization and mechanical experiment techniques used in pervious chapters, to biosilica frustules of marine diatoms. We first introduced the idea of microstructure hierarchy, and how it can elevate material properties to beyond the simple mixture of ingredients, an effect commonly found in hard biomaterials in nature. We then presented several examples of how biomaterials use hierarchy to achieve impressive properties, before surveying the existing studies on diatoms, which are limited in quantity and scope due to the small sample size and accompanying difficulties.

Chapter 6 focuses on characterizing the microstructure and material-level mechanical properties of diatoms. We combined small scale mechanical experiments and finite element simulations to separate the material-level and microstructure-level contributions to diatoms' mechanical response. We then showed that by combining flaw-free microstructure and hierarchical design, diatom frustules are able to achieve extraordinary strength-to-density ratio, which is among the highest in biomaterials.

Chapter 7 presents a study to capture the hierarchy and microstructure of diatom frustules using POSS-based silica structure from two photon lithography. We showed that POSS structures can be designed and fabricated to 1:1 capture the hierarchical design of diatom frustules. In addition, they possess the same flaw-free microstructure as diatom biosilica, and show highly similar mechanical response. We then conducted small scale fracture experiments that leverage on the reproducibility of diatom-mimetic POSS structures, and proposed that the design of diatom frustules can arrest crack propagation without access to microstructural toughening mechanisms.

The underlying theme of these studies is how slight variations in microstructures can lead to significant changes in different facets of material properties. We showed the more obvious case of how different deposition methods lead to visible changes in grain structure, and how that can significantly affect electrical performance of solar cell devices; we also showed that in the same material system, without altering the grain structure or introducing any visible

microstructure features, property enhancement can still be reached by slightly altering energetics of point defects in the system; finally we investigated the effect of hierarchical arrangement of microstructures, how they can lead to extraordinary mechanical properties with simple constituent materials, and how we can use these knowledge to make manmade materials that capture these properties.

Investigation into the effects of microstructure on material properties is an immensely complex subject that encompasses most of the materials science field. We have considered several material systems in this work, and demonstrated the different ways microstructures can lead to drastic differences in materials properties. We have also outlined several open questions and avenues of investigation within each material system, as well as the prospect of applying similar techniques to other systems. We hope this thesis will serve as a guide and reference for future work.

Bibliography

1. Montemayor, L., Chernow, V. & Greer, J. R. Materials by design: Using architecture in material design to reach new property spaces. *MRS Bull.* **40,** 1122–1129 (2015).

2. Monro, T. M. & Ebendorff-Heidepriem, H. PROGRESS IN MICROSTRUCTURED OPTICAL FIBERS. *Annu. Rev. Mater. Res.* **36,** 467–495 (2006).

3. Lima, R. S. & Marple, B. R. Thermal Spray Coatings Engineered from Nanostructured Ceramic Agglomerated Powders for Structural, Thermal Barrier and Biomedical Applications: A Review. *J. Therm. Spray Technol.* **16,** 40–63 (2007).

4. Shah, A. V *et al.* Thin-film silicon solar cell technology. *Prog. photovoltaics Res. Appl.* **12,** 113–142 (2004).

5. Greer, J. R., Th, J. & Hosson, M. De. Progress in Materials Science Plasticity in small-sized metallic systems : Intrinsic versus extrinsic size effect. *Prog. Mater. Sci.* **56,** 654–724 (2011).

6. Hirth, J. P. The influence of grain boundaries on mechanical properties. *Metall. Mater. Trans. B* **3,** 3047–3067 (1972).

7. Wang, N., Wang, Z., Aust, K. T. & Erb, U. Effect of grain size on mechanical properties of nanocrystalline materials. *Acta Metall. Mater.* **43,** 519–528 (1995).

8. Nix, W. D. & Gao, H. Indentation size effects in crystalline materials: A law for strain gradient plasticity. *J. Mech. Phys. Solids* **46,** 411–425 (1998).

9. Arzt, E. Size effects in materials due to microstructural and dimensional constraints: a comparative review. *Acta Mater.* **46,** 5611–5626 (1998).

10. Montemayor, L. C., Meza, L. R. & Greer, J. R. Design and Fabrication of Hollow Rigid Nanolattices via Two-Photon Lithography. *Adv. Eng. Mater.* **16,** 184–189 (2014).

11. Meza, L. R. *et al.* Resilient 3D hierarchical architected metamaterials. *Proc. Natl. Acad. Sci.* **112,** 11502–11507 (2015).

12. Meza, L. R., Das, S. & Greer, J. R. Strong, lightweight, and recoverable three-dimensional ceramic nanolattices. *Science (80-.).* **345,** 1322–1326 (2014).

13. Valentine, J. *et al.* Three-dimensional optical metamaterial with a negative refractive index. **455,** (2008).

14. Smith, D. R., Pendry, J. B. & Wiltshire, M. C. K. Metamaterials and Negative Refractive Index. **305,** 788–793 (2004).

15. Mendelson, M. Average Grain Size in Polycrystalline Ceramics. *J. Am. Ceram. Soc.* **52,** 443–446 (1969).

16. Schroers, J. & Johnson, W. L. Ductile bulk metallic glass. *Phys. Rev. Lett.* **93,** 255506 (2004).

17. Koch, C. C. The synthesis and structure of nanocrystalline materials produced by mechanical attrition: A review. *Nanostructured Mater.* **2,** 109–129 (1993).

18. Raj, R. & Ashby, M. F. On grain boundary sliding and diffusional creep. *Metall. Mater. Trans. B* **2,** 1113–1127 (1971).

19. Barnett, M. R., Keshavarz, Z., Beer, A. G. & Atwell, D. Influence of grain size on the compressive deformation of wrought Mg–3Al–1Zn. *Acta Mater.* **52,** 5093–5103 (2004).

20. Aitken, Z. H., Jang, D., Weinberger, C. R. & Greer, J. R. Grain Boundary Sliding in Aluminum Nano-Bi-Crystals Deformed at Room Temperature. *Small* **10,** 100–108 (2014).

21. Aitken, Z. H., Fan, H., El-Awady, J. A. & Greer, J. R. The effect of size, orientation and alloying on the deformation of {AZ31} nanopillars. *J. Mech. Phys. Solids* **76,** 208–223 (2015).

22. Jang, D. & Greer, J. R. Size-induced weakening and grain boundary-assisted deformation in 60 nm grained Ni nanopillars. *Scr. Mater.* **64,** 77–80 (2011).

23. Seager, C. H. Grain boundary recombination: Theory and experiment in silicon. *J. Appl. Phys.* **52,** 3960–3968 (1981).

24. Seager, C. H. & Ginley, D. S. Passivation of grain boundaries in polycrystalline silicon. *Appl. Phys. Lett.* **34,** 337–340 (1979).

25. Chin, V. W. L., Tansley, T. L. & Osotchan, T. Electron mobilities in gallium, indium, and aluminum nitrides. *J. Appl. Phys.* **75,** 7365–7372 (1994).

26. Seager, C. H. & Pike, G. E. Electron tunneling through GaAs grain boundaries. *Appl. Phys. Lett.* **40,** 471–474 (1982).

27. Cheng, G. S. *et al.* Large-scale synthesis of single crystalline gallium nitride nanowires. *Appl. Phys. Lett.* **75,** 2455–2457 (1999).

28. Fang, S. F. *et al.* Gallium arsenide and other compound semiconductors on silicon. *J. Appl. Phys.* **68,** R31–R58 (1990).

29. Green, M. A., Emery, K., Hishikawa, Y., Warta, W. & Dunlop, E. D. Solar cell efficiency tables (version 44). *Prog. Photovoltaics Res. Appl.* **22,** 701–710 (2014).

30. Baier, R. Electronic grain boundary properties in polycrystalline Cu (In , Ga) Se 2 semiconductors for thin film solar cells. (2012).

31. Wu, T.-T. *et al.* Improved efficiency of a large-area Cu(In,Ga)Se$_2$ solar cell by a nontoxic hydrogen-assisted solid Se vapor selenization process. *ACS Appl. Mater. Interfaces* **6,** 4842–9 (2014).

32. Pethe, S. a., Takahashi, E., Kaul, A. & Dhere, N. G. Effect of sputtering process parameters on film properties of molybdenum back contact. *Sol. Energy Mater. Sol. Cells* **100,** 1–5 (2012).

33. Ng, K. S. & Ngan, A. H. W. Breakdown of Schmid's law in micropillars. *Scr. Mater.* **59,** 796–799 (2008).

34. Oh, S. H., Legros, M., Kiener, D. & Dehm, G. In situ observation of dislocation nucleation and escape in a submicrometre aluminium single crystal. *Nat. Mater.* **8,** 95–100 (2009).

35. Uchic, M. D. Sample Dimensions Influence Strength and Crystal Plasticity. *Science (80-.).* **305,** 986–989 (2004).

36. Dimiduk, D. M., Uchic, M. D. & Parthasarathy, T. A. Size-affected single-slip behavior of pure nickel microcrystals. *Acta Mater.* **53,** 4065–4077 (2005).

37. Norfleet, D. M., Dimiduk, D. M., Polasik, S. J., Uchic, M. D. & Mills, M. J. Dislocation structures and their relationship to strength in deformed nickel microcrystals. *Acta Mater.* **56,** 2988–3001 (2008).

38. Shan, Z. W., Mishra, R. K., Syed Asif, S. A., Warren, O. L. & Minor, A. M. Mechanical annealing and source-limited deformation in submicrometre-diameter Ni crystals. *Nat. Mater.* **7,** 115–119 (2008).

39. Kim, J.-Y., Jang, D. & Greer, J. R. Tensile and compressive behavior of tungsten, molybdenum, tantalum and niobium at the nanoscale. *Acta Mater.* **58,** 2355–2363 (2010).

40. Bei, H., Shim, S., Miller, M. K., Pharr, G. M. & George, E. P. Effects of focused ion beam milling on the nanomechanical behavior of a molybdenum-alloy single crystal. *Appl. Phys. Lett.* **91,** 111915 (2007).

41. Greer, J. R., Jang, D., Kim, J.-Y. & Burek, M. J. Emergence of New Mechanical Functionality in Materials via Size Reduction. *Adv. Funct. Mater.* **19,** 2880–2886 (2009).

42. Schneider, A. S. *et al.* Correlation between Critical Temperature and Strength of Small-Scale bcc Pillars. *Phys. Rev. Lett.* **103,** 105501 (2009).

43. Lai, Y. H. *et al.* Bulk and microscale compressive behavior of a Zr-based metallic glass. *Scr. Mater.* **58,** 890–893 (2008).

44. Cheng, S., Wang, X.-L., Choo, H. & Liaw, P. K. Global melting of Zr57Ti5Ni8Cu20Al10 bulk metallic glass under microcompression. *Appl. Phys. Lett.* **91,** 201917 (2007).

45. Lee, C. J., Huang, J. C. & Nieh, T. G. Sample size effect and microcompression of Mg65Cu25Gd10 metallic glass. *Appl. Phys. Lett.* **91,** 161913 (2007).

46. Liontas, R. *et al.* Substantial tensile ductility in sputtered Zr-Ni-Al nano-sized metallic glass. *Acta Mater.* **118,** 270–285 (2016).

47. Adibi, S. *et al.* Surface roughness imparts tensile ductility to nanoscale metallic glasses. *Extrem. Mech. Lett.* **5,** 88–95 (2015).

48. Chen, D. Z. *et al.* Nanometallic Glasses: Size Reduction Brings Ductility, Surface State Drives Its Extent. *Nano Lett.* **13,** 4462–4468 (2013).

49. Chen, D. Z., Gu, X. W., An, Q., Goddard, W. A. & Greer, J. R. Ductility and work hardening in nano-sized metallic glasses. *Appl. Phys. Lett.* **106,** 61903 (2015).

50. Lee, S.-W., Jafary-Zadeh, M., Chen, D. Z., Zhang, Y.-W. & Greer, J. R. Size Effect

Suppresses Brittle Failure in Hollow Cu 60 Zr 40 Metallic Glass Nanolattices Deformed at Cryogenic Temperatures. *Nano Lett.* **15,** 5673–5681 (2015).

51. Jang, D. & Greer, J. R. Transition from a strong-yet-brittle to a stronger-and-ductile state by size reduction of metallic glasses. *Nat. Mater.* (2010). doi:10.1038/nmat2622

52. Dehm, G. Miniaturized single-crystalline fcc metals deformed in tension: New insights in size-dependent plasticity. *Prog. Mater. Sci.* **54,** 664–688 (2009).

53. Kiener, D., Grosinger, W., Dehm, G. & Pippan, R. A further step towards an understanding of size-dependent crystal plasticity: In situ tension experiments of miniaturized single-crystal copper samples. *Acta Mater.* **56,** 580–592 (2008).

54. Kiener, D., Grosinger, W. & Dehm, G. On the importance of sample compliance in uniaxial microtesting. *Scr. Mater.* **60,** 148–151 (2009).

55. Kiener, D., Motz, C. & Dehm, G. Micro-compression testing: A critical discussion of experimental constraints. *Mater. Sci. Eng. A* **505,** 79–87 (2009).

56. Shan, Z. W. *et al.* Plastic flow and failure resistance of metallic glass: Insight from in situ compression of nanopillars. *Phys. Rev. B* **77,** 155419 (2008).

57. Schuster, B. E. *et al.* Bulk and microscale compressive properties of a Pd-based metallic glass. *Scr. Mater.* **57,** 517–520 (2007).

58. Zheng, Q., Cheng, S., Strader, J. H., Ma, E. & Xu, J. Critical size and strength of the best bulk metallic glass former in the Mg–Cu–Gd ternary system. *Scr. Mater.* **56,** 161–164 (2007).

59. Guo, H. *et al.* Tensile ductility and necking of metallic glass. *Nat. Mater.* **6,** 735–739 (2007).

60. Reichelt, R. in *Science of Microscopy* 133–272 (Springer New York). doi:10.1007/978-0-387-49762-4_3

61. Williams, D. B. & Carter, C. B. *Transmission Electron Microscopy*. (Springer US, 2009). doi:10.1007/978-0-387-76501-3

62. FEI. Verios ™ Scanning Electron Microscope Datasheet. (2016).

63. Park, J. *et al.* 3D structure of individual nanocrystals in solution by electron microscopy. *Science (80-.).* **349,** 290–295 (2015).

64. Scott, M. C. *et al.* Electron tomography at 2.4-ångström resolution. *Nature* **483,** 444–447 (2012).

65. de Oteyza, D. G. *et al.* Direct Imaging of Covalent Bond Structure in Single-Molecule Chemical Reactions. *Science (80-.).* **340,** 1434–1437 (2013).

66. Giannuzzi, L. A. & Stevie, F. A. *Introduction to Focused Ion Beams*. (Springer US, 2005). doi:10.1007/b101190

67. Wasa, K. & Hayakawa, S. Handbook of sputter deposition technology. (1992).

68. FEI. Vion ™ Plasma FIB System Datasheet.

69. Tamura, M., Shukuri, S., Moniwa, M. & Default, M. Focused ion beam gallium implantation into silicon. *Appl. Phys. A Mater. Sci. Process.* **39,** 183–190 (1986).

70. Miller, M. K., Russell, K. F., Thompson, K., Alvis, R. & Larson, D. J. Review of atom probe FIB-based specimen preparation methods. *Microsc. Microanal.* **13,** 428–436 (2007).

71. Giannuzzi, L. A. & Stevie, F. A. A review of focused ion beam milling techniques for TEM specimen preparation. *Micron* **30,** 197–204 (1999).

72. Jung, P., Henry, J., Chen, J. & Brachet, J.-C. Effect of implanted helium on tensile properties and hardness of 9% Cr martensitic stainless steels. *J. Nucl. Mater.* **318,** 241–248 (2003).

73. Bassim, N., Scott, K. & Giannuzzi, L. A. Recent advances in focused ion beam technology and applications. *MRS Bull.* **39,** 317–325 (2014).

74. Marko, M., Hsieh, C., Schalek, R., Frank, J. & Mannella, C. Focused-ion-beam thinning of frozen-hydrated biological specimens for cryo-electron microscopy. *Nat. Methods* **4,** 215–217 (2007).

75. Landau, P., Guo, Q., Hosemann, P., Wang, Y. & Greer, J. R. Deformation of as-fabricated and helium implanted 100nm-diameter iron nano-pillars. *Mater. Sci. Eng. A* **612,** 316–325 (2014).

76. Gu, X. W. *et al.* Size-Dependent Deformation of Nanocrystalline Pt Nanopillars. *Nano Lett.* **12,** 6385–6392 (2012).

77. Tertuliano, O. A. & Greer, J. R. The nanocomposite nature of bone drives its strength and damage resistance. *Nat. Mater.* **15,** 1195–1202 (2016).

78. Van Grieken, R. & Markowicz, A. *Handbook of X-ray Spectrometry*. (CRC Press, 2001).

79. Lu, P., Zhou, L., Kramer, M. J. & Smith, D. J. Atomic-scale Chemical Imaging and Quantification of Metallic Alloy Structures by Energy-Dispersive X-ray Spectroscopy. *Sci. Rep.* **4,** 3945 (2015).

80. D'Alfonso, A. J., Freitag, B., Klenov, D. & Allen, L. J. Atomic-resolution chemical mapping using energy-dispersive x-ray spectroscopy. *Phys. Rev. B* **81,** 100101 (2010).

81. Egoavil, R. *et al.* Atomic resolution mapping of phonon excitations in STEM-EELS experiments. *Ultramicroscopy* **147,** 1–7 (2014).

82. Lopez-Haro, M. *et al.* Atomic-scale structure and composition of Pt3Co/C nanocrystallites during real PEMFC operation: A STEM–EELS study. *Appl. Catal. B Environ.* **152–153,** 300–308 (2014).

83. Oliver, W. C. & Pharr, G. M. An improved technique for determining hardness and elastic modulus using load and displacement sensing indentation experiments. *J. Mater. Res.* **7,** 1564–1583 (1992).

84. Gerberich, W. W., Nelson, J. C., Lilleodden, E. T., Anderson, P. & Wyrobek, J. T. Indentation induced dislocation nucleation: The initial yield point. *Acta Mater.* **44,** 3585–3598 (1996).

85. Smith, R., Christopher, D., Kenny, S. D., Richter, A. & Wolf, B. Defect generation and pileup of atoms during nanoindentation of Fe single crystals. *Phys. Rev. B* **67,** 245405 (2003).

86. Choi, Y., Lee, H.-S. & Kwon, D. Analysis of sharp-tip-indentation load–depth curve for contact area determination taking into account pile-up and sink-in effects. *J. Mater. Res.* **19,** 3307–3315 (2004).

87. Bufford, D., Liu, Y., Wang, J., Wang, H. & Zhang, X. In situ nanoindentation study on plasticity and work hardening in aluminium with incoherent twin boundaries. *Nat. Commun.* **5,** 4864 (2014).

88. Ni, X., Papanikolaou, S., Vajente, G., Adhikari, R. X. & Greer, J. R. Probing Microplasticity in Small-Scale FCC Crystals via Dynamic Mechanical Analysis. *Phys. Rev. Lett.* **118,** 155501 (2017).

89. Legros, M., Gianola, D. S. & Motz, C. Quantitative In Situ Mechanical Testing in Electron Microscopes. *MRS Bull.* **35,** 354–360 (2010).

90. Greer, J. R., Kim, J.-Y. & Burek, M. J. The in-situ mechanical testing of nanoscale single-crystalline nanopillars. *JOM* **61,** 19–25 (2009).

91. Aitken, Z. H., Jang, D., Weinberger, C. R. & Greer, J. R. Grain Boundary Sliding in Aluminum Nano-Bi-Crystals Deformed at Room Temperature. *Small* **10,** 100–108 (2014).

92. Huang, Y., Bai, X. & Zhang, Y. In situ mechanical properties of individual ZnO nanowires and the mass measurement of nanoparticles. *J. Phys. Condens. Matter* **18,** L179–L184 (2006).

93. Hutchens, S. B., Hall, L. J. & Greer, J. R. In situ Mechanical Testing Reveals Periodic Buckle Nucleation and Propagation in Carbon Nanotube Bundles. *Adv. Funct. Mater.* **20,** 2338–2346 (2010).

94. Hysitron. Hysitron PI-95 PicoIndenter Datasheet. (2016).

95. Pharr, G. M., Herbert, E. G. & Gao, Y. The Indentation Size Effect: A Critical Examination of Experimental Observations and Mechanistic Interpretations. *Annu. Rev. Mater. Res.* **40,** 271–292 (2010).

96. Buehler, M. J., Abraham, F. F. & Gao, H. Hyperelasticity governs dynamic fracture at a critical length scale. *Nature* **426,** 141 (2003).

97. Duan, K., Hu, X. & Wittmann, F. H. Scaling of quasi-brittle fracture: Boundary and size effect. *Mech. Mater.* **38,** 128–141 (2006).

98. Niki, S. *et al.* CIGS absorbers and processes. *Prog. Photovoltaics Res. Appl.* **18,** 453–466 (2010).

99. Hahn, H. & Lorent, C. De. Untersuchungen über ternäre Chalkogenide. XII. Über ternäre Chalkogenide des Chroms mit einwertigem Kupfer und Silber. *Zeitschrift für Anorg. und Allg. Chemie* **290,** 68–81 (1957).

100. Wagner, S., Shay, J. L., Migliorato, P. & Kasper, H. M. CuInSe2/CdS heterojunction

photovoltaic detectors. *Appl. Phys. Lett.* **25,** 434–435 (1974).

101.   Kazmerski, L. L., White, F. R. & Morgan, G. K. Thin-film CuInSe2/CdS heterojunction solar cells. *Appl. Phys. Lett.* **29,** 268–270 (1976).

102.   Devaney, W. E., Michelsen, R. A. & Chen, W. S. Proc. 18th IEEE Photovoltaic Specialists Conference. (18AD).

103.   Singh, U. P. & Patra, S. P. Progress in polycrystalline thin-film Cu(In,Ga) Se2 solar cells. *Int. J. Photoenergy* **2010,** (2010).

104.   Kamada, R. *et al.* New world record Cu (In, Ga)(Se, S) 2 thin film solar cell efficiency beyond 22%. in *Photovoltaic Specialists Conference (PVSC), 2016 IEEE 43rd* 1287–1291 (IEEE, 2016).

105.   Green, M. A. *et al.* Solar cell efficiency tables (version 50). *Prog. Photovoltaics Res. Appl.* **25,** 668–676 (2017).

106.   Chirilă, A. *et al.* Potassium-induced surface modification of Cu(In,Ga)Se2 thin films for high-efficiency solar cells. *Nat. Mater.* **12,** 1107–11 (2013).

107.   Ramanujam, J. & Singh, U. P. Copper indium gallium selenide based solar cells – a review. *Energy Environ. Sci.* **10,** 1306–1319 (2017).

108.   Wang, Y.-C. & Shieh, H.-P. D. Improvement of bandgap homogeneity in Cu (In, Ga) Se2 thin films using a modified two-step selenization process. *Appl. Phys. Lett.* **103,** 153502 (2013).

109.   Sandroff, C. J., Nottenburg, R. N., Bischoff, J.-C. & Bhat, R. Dramatic enhancement in the gain of a GaAs/AlGaAs heterostructure bipolar transistor by surface chemical passivation. *Appl. Phys. Lett.* **51,** 33 (1987).

110.   Sheldon, M. T., Eisler, C. N. & Atwater, H. A. GaAs Passivation with Trioctylphosphine Sulfide for Enhanced Solar Cell Efficiency and Durability. *Adv. Energy Mater.* **2,** 339–344 (2012).

111.   Yoon, J.-H. *et al.* Optical analysis of the microstructure of a Mo back contact for Cu(In,Ga)Se2 solar cells and its effects on Mo film properties and Na diffusivity. *Sol. Energy Mater. Sol. Cells* **95,** 2959–2964 (2011).

112.   Matson, R., Granata, J., Asher, S. & Young, M. Effects of Substrate and Na Concentration on Device Properties, Junction Formation, and Film Microstructure in CuInSe2 PV Devices. in *AIP Conference* (1998).

113.   Witte, W., Kniese, R. & Powalla, M. Raman investigations of Cu (In, Ga) Se 2 thin films with various copper contents. *Thin Solid Films* **517,** 867–869 (2008).

114.   Jackson, P. *et al.* Properties of Cu(In,Ga)Se $_2$ solar cells with new record efficiencies up to 21.7%. *Phys. status solidi - Rapid Res. Lett.* **9,** 28–31 (2015).

115.   Powalla, M., Voorwinden, G., Hariskos, D., Jackson, P. & Kniese, R. Highly efficient CIS solar cells and modules made by the co-evaporation process. *Thin Solid Films* **517,** 2111–

2114 (2009).

116. Wang, H. *et al.* Effect of substrate temperature on the structural and electrical properties of CIGS films based on the one-stage co-evaporation process. *Semicond. Sci. Technol.* **25,** 55007 (2010).

117. Mickelsen, R. A. & Chen, W. S. High photocurrent polycrystalline thin-film CdS/CuInSe 2 solar cell a. *Appl. Phys. Lett.* **36,** 371–373 (1980).

118. Tuttle, J. R. *et al.* Perspective on High-efficiency Cu (In, Ga) Se2-based Thin-film Solar Cells Fabricated by Simple, Scalable Processes. *Prog. Photovoltaics Res. Appl.* **3,** 383–391 (1995).

119. Kessler, F. & Rudmann, D. Technological aspects of flexible CIGS solar cells and modules. *Sol. Energy* **77,** 685–695 (2004).

120. Gloeckler, M. & Sites, J. R. Band-gap grading in Cu (In, Ga) Se 2 solar cells. *J. Phys. Chem. Solids* **66,** 1891–1894 (2005).

121. Contreras, M. A. *et al.* High efficiency graded bandgap thin-film polycrystalline Cu (In, Ga) Se2-based solar cells. *Sol. energy Mater. Sol. cells* **41,** 231–246 (1996).

122. Jackson, P. *et al.* New world record efficiency for Cu(In,Ga)Se2 thin-film solar cells beyond 20%. *Prog. Photovoltaics Res. Appl.* **19,** 894–897 (2011).

123. Zweigart, S. *et al.* Sequential deposition of Cu (In, Ga)(S, Se)/sub 2. in *Photovoltaic Energy Conversion, 1994., Conference Record of the Twenty Fourth. IEEE Photovoltaic Specialists Conference-1994, 1994 IEEE First World Conference on* **1,** 60–67 (IEEE, 1994).

124. Adurodija, F. O. *et al.* Growth of CuInSe 2 thin films by high vapour Se treatment of co-sputtered Cu-In alloy in a graphite container. *Thin Solid Films* **338,** 13–19 (1999).

125. Zank, J., Mehlin, M. & Fritz, H. P. Electrochemical codeposition of indium and gallium for chalcopyrite solar cells. *Thin Solid Films* **286,** 259–263 (1996).

126. Guillen, C., Martınez, M. A. & Herrero, J. CuInSe 2 thin films obtained by a novel electrodeposition and sputtering combined method. *Vacuum* **58,** 594–601 (2000).

127. Marudachalam, M. *et al.* Preparation of homogeneous Cu(InGa)Se2 films by selenization of metal precursors in H2Se atmosphere. *Appl. Phys. Lett.* **67,** 3978 (1995).

128. Rastogi, A. C., Balakrishnan, K. S., Sharma, R. K. & Jain, K. Growth phases during electrochemical selenization of vacuum deposited CuIn metal layers for the formation of semiconducting CuInSe 2 films. *Thin Solid Films* **357,** 179–188 (1999).

129. Sadigov, M. S., Özkan, M., Bacaksiz, E., Altunbaş, M. & Kopya, A. I. Production of CuInSe2 thin films by a sequential processes of evaporations and selenization. *J. Mater. Sci.* **34,** 4579–4584 (1999).

130. Caballero, R. & Guillén, C. Comparative studies between Cu-Ga-Se and Cu-In-Se thin film systems. *Thin Solid Films* **403,** 107–111 (2002).

131. Guillén, C. & Herrero, J. Structure, morphology and photoelectrochemical activity of CuInSe

2 thin films as determined by the characteristics of evaporated metallic precursors. *Sol. energy Mater. Sol. cells* **73,** 141–149 (2002).

132. J. M. Merino, S. Díaz-Moreno, G. Subías, M. L. A comparative study of Cu-Se and In-Se bond length distributions in CuInSe2 with related In-rich compounds. *Thin Solid Films* 295–300 (2005).

133. Huang, C.-H., Shih, Y. C., Chuang, W.-J. & Lin, C.-P. Impacts of process parameters on CIGS solar cells prepared by selenization process with Se Vapor. in *2010 10th IEEE International Conference on Solid-State and Integrated Circuit Technology* 2019–2021 (Ieee, 2010). doi:10.1109/ICSICT.2010.5667893

134. Mueller, B. J. *et al.* Influence of different sulfur to selenium ratios on the structural and electronic properties of Cu (In, Ga)(S, Se) 2 thin films and solar cells formed by the stacked elemental layer process. *J. Appl. Phys.* **116,** 174503 (2014).

135. Kaelin, M., Rudmann, D. & Tiwari, A. N. Low cost processing of CIGS thin film solar cells. *Sol. Energy* **77,** 749–756 (2004).

136. Hibberd, C. J. *et al.* Non-vacuum methods for formation of Cu (In, Ga)(Se, S) 2 thin film photovoltaic absorbers. *Prog. Photovoltaics Res. Appl.* **18,** 434–452 (2010).

137. Guillemoles, J. *et al.* One step electrodeposition of CuInSe2: Improved structural, electronic, and photovoltaic properties by annealing under high selenium pressure. *J. Appl. Phys.* **79,** 7293–7302 (1996).

138. Guo, Q., Ford, G. M., Hillhouse, H. W. & Agrawal, R. Sulfide nanocrystal inks for dense Cu (In1− x Gax)(S1− y Se y) 2 absorber films and their photovoltaic performance. *Nano Lett.* **9,** 3060–3065 (2009).

139. Mitzi, D. B. Solution processing of chalcogenide semiconductors via dimensional reduction. *Adv. Mater.* **21,** 3141–3158 (2009).

140. Guo, Q., Ford, G. M., Agrawal, R. & Hillhouse, H. W. Ink formulation and low-temperature incorporation of sodium to yield 12% efficient Cu(In,Ga)(S,Se) 2 solar cells from sulfide nanocrystal inks. *Prog. Photovoltaics Res. Appl.* **21,** 64–71 (2013).

141. Guillemoles, J. F. *et al.* Solution processing route to high efficiency CuIn (S, Se) 2 solar cells. in *Journal of Nano Research* **4,** 79–89 (Trans Tech Publ, 2008).

142. Reinhard, P., Buecheler, S. & Tiwari, A. N. Technological status of Cu (In, Ga)(Se, S) 2-based photovoltaics. *Sol. Energy Mater. Sol. Cells* **119,** 287–290 (2013).

143. Wang, W., Su, Y.-W. & Chang, C. Inkjet printed chalcopyrite CuIn x Ga 1− x Se 2 thin film solar cells. *Sol. Energy Mater. Sol. Cells* **95,** 2616–2620 (2011).

144. Kapur, V. K., Bansal, A., Le, P. & Asensio, O. I. Non-vacuum processing of CuIn 1− x Ga x Se 2 solar cells on rigid and flexible substrates using nanoparticle precursor inks. *Thin Solid Films* **431,** 53–57 (2003).

145. Lee, D.-Y., Park, S. & Kim, J. Structural analysis of CIGS film prepared by chemical spray

deposition. *Curr. Appl. Phys.* **11,** S88–S92 (2011).

146. Brown, G., Stone, P., Woodruff, J., Cardozo, B. & Jackrel, D. Device characteristics of a 17.1% efficient solar cell deposited by a non-vacuum printing method on flexible foil. in *Photovoltaic Specialists Conference (PVSC), 2012 38th IEEE* 3230–3233 (IEEE, 2012).

147. Olejníček, J. *et al.* A non-vacuum process for preparing nanocrystalline CuIn 1− xGaxSe 2 materials involving an open-air solvothermal reaction. *Sol. Energy Mater. Sol. Cells* **94,** 8–11 (2010).

148. Todorov, T. K., Gunawan, O., Gokmen, T. & Mitzi, D. B. Solution-processed Cu (In, Ga)(S, Se) 2 absorber yielding a 15.2% efficient solar cell. *Prog. Photovoltaics Res. Appl.* **21,** 82–87 (2013).

149. Kiss, J., Gruhn, T., Roma, G. & Felser, C. Theoretical Study on the Structure and Energetics of Cd Insertion and Cu Depletion of CuIn5Se8. *J. Phys. Chem. C* **117,** 10892–10900 (2013).

150. Rudmann, D. *et al.* Efficiency enhancement of Cu(In,Ga)Se[sub 2] solar cells due to post-deposition Na incorporation. *Appl. Phys. Lett.* **84,** 1129 (2004).

151. Contreras, M. A. *et al.* On the role of Na and modifications to Cu(In,Ga)Se/sub 2/ absorber materials using thin-MF (M=Na, K, Cs) precursor layers [solar cells]. in *Conference Record of the Twenty Sixth IEEE Photovoltaic Specialists Conference - 1997* 359–362 (IEEE, 1997). doi:10.1109/PVSC.1997.654102

152. Kar, M., Agrawal, R. & Hillhouse, H. W. Formation pathway of CuInSe2 nanocrystals for solar cells. *J. Am. Chem. Soc.* **133,** 17239–17247 (2011).

153. Rudmann, D. *et al.* Effects of NaF coevaporation on structural properties of Cu(In,Ga)Se2 thin films. *Thin Solid Films* **431–432,** 37–40 (2003).

154. Ård, M. B., Granath, K. & Stolt, L. Growth of Cu (In, Ga) Se 2 thin films by coevaporation using alkaline precursors. *Thin Solid Films* **361,** 9–16 (2000).

155. Granath, K., Bodegård, M. & Stolt, L. The effect of NaF on Cu (In, Ga) Se 2 thin film solar cells. *Sol. energy Mater. Sol. cells* **60,** 279–293 (2000).

156. Shin, D. *et al.* Effects of the incorporation of alkali elements on Cu (In, Ga) Se 2 thin film solar cells. *Sol. Energy Mater. Sol. Cells* **157,** 695–702 (2016).

157. Oikkonen, L. E., Ganchenkova, M. G., Seitsonen, A. P. & Nieminen, R. M. Effect of sodium incorporation into CuInSe2 from first principles. *J. Appl. Phys.* **114,** 83503 (2013).

158. Braunger, D., Hariskos, D., Bilger, G., Rau, U. & Schock, H. W. Influence of sodium on the growth of polycrystalline Cu (In, Ga) Se 2 thin films. *Thin Solid Films* **361,** 161–166 (2000).

159. Garg, A., Balakrishnan, K. S. & Rastogi, A. C. Structural properties and growth mechanism of copper and indium selenide films prepared by electrochemical selenization of metal layers. *J. Electrochem. Soc.* **141,** 1566–1572 (1994).

160. Kiss, J., Gruhn, T., Roma, G. & Felser, C. Theoretical Study on the Diffusion Mechanism of

Cd in the Cu-Poor Phase of CuInSe 2 Solar Cell Material. *J. Phys. Chem. C* **117,** 25933–25938 (2013).

161. Holz, J., Karg, F. & Philipsborn, H. v. The effect of substrate impurities on the electronic conductivity in CIS thin films. in *Proceedings of the 12th European Photovoltaic Solar Energy Conference* 1592–1595 (1994).

162. Lammer, M., Klemm, U. & Powalla, M. Sodium co-evaporation for low temperature Cu (In, Ga) Se 2 deposition. *Thin Solid Films* **387,** 33–36 (2001).

163. Probst, V. *et al.* The impact of controlled sodium incorporation on rapid thermal processed Cu (InGa) Se/sub 2/-thin films and devices. in *Photovoltaic Energy Conversion, 1994., Conference Record of the Twenty Fourth. IEEE Photovoltaic Specialists Conference-1994, 1994 IEEE First World Conference on* **1,** 144–147 (IEEE, 1994).

164. Ishizuka, S. *et al.* Na-induced variations in the structural, optical, and electrical properties of Cu(In,Ga)Se[sub 2] thin films. *J. Appl. Phys.* **106,** 34908 (2009).

165. Nakada, T., Ohbo, H., Fukuda, M. & Kunioka, A. Improved compositional flexibility of Cu(In,Ga)Se2-based thin film solar cells by sodium control technique. *Sol. Energy Mater. Sol. Cells* **49,** 261–267 (1997).

166. Rockett, A. *et al.* Na in selenized Cu (In, Ga) Se 2 on Na-containing and Na-free glasses: distribution, grain structure, and device performances. *Thin Solid Films* **372,** 212–217 (2000).

167. Granata, J. E. & Sites, J. R. Impact of sodium in the bulk and in grain boundaries of CuInSe2. in *Proceedings of the 2nd World Conference on Photovoltaic Solar Energy Conversion* **1,** 604–607 (1998).

168. Lyahovitskaya, V. *et al.* Na effects on CuInSe[sub 2]: Distinguishing bulk from surface phenomena. *J. Appl. Phys.* **91,** 4205 (2002).

169. Rockett, a., Bodegard, M., Granath, K. & Stolt, L. Na incorporation and diffusion in CuIn(1-x)Ga(x)Se2. *Conf. Rec. Twenty Fifth IEEE Photovolt. Spec. Conf. - 1996* 985–987 (1996). doi:10.1109/PVSC.1996.564295

170. Caballero, R. *et al.* The influence of Na on low temperature growth of CIGS thin film solar cells on polyimide substrates. *Thin Solid Films* **517,** 2187–2190 (2009).

171. Matson, R. J. *et al.* Metal contacts to CuInSe2. *Sol. Cells* **11,** 301–305 (1984).

172. Moons, E., Engelhard, T. & Cahen, D. Ohmic contacts to p-CuInSe 2 crystals. *J. Electron. Mater.* **22,** 275–280 (1993).

173. Scofield, J. H., Duda, A., Albin, D., Ballard, B. L. & Predecki, P. K. Sputtered molybdenum bilayer back contact for copper indium diselenide-based polycrystalline thin-film solar cells. *Thin Solid Films* **260,** 26–31 (1995).

174. Hoffman, R. A., Lin, J. C. & Chambers, J. P. The effect of ion bombardment on the microstructure and properties of molybdenum films. *Thin Solid Films* **206,** 230–235 (1991).

175. Gordillo, G., Grizalez, M. & Hernandez, L. C. Structural and electrical properties of DC sputtered molybdenum films. *Sol. energy Mater. Sol. cells* **51,** 327–337 (1998).

176. Martınez, M. A. & Guillén, C. Effect of rf-sputtered Mo substrate on the microstructure of electrodeposited CuInSe 2 thin films. *Surf. Coatings Technol.* **110,** 62–67 (1998).

177. Powalla, M. & Dimmler, B. Scaling up issues of CIGS solar cells. *Thin Solid Films* **361,** 540–546 (2000).

178. Perng, D.-C., Hung, M.-C. & Wang, K.-Y. Reliability studies of mo layer deposited on polyimide substrate for CIGS solar cell applications. in *2012 38th IEEE Photovoltaic Specialists Conference* 000891–000894 (IEEE, 2012). doi:10.1109/PVSC.2012.6317745

179. Jaegaermann, W., Löher, T. & Pettenkofer, C. Surface properties of chalcopyrite semiconductors. *Cryst. Res. Cryst. Technol.* **31,** 273 (1996).

180. Russell, P. E. *et al.* Properties of the Mo-CuInSe2 interface. *Appl. Phys. Lett.* **40,** 995–997 (1982).

181. Raud, S. & Nicolet, M.-A. Study of the CuInSe2/Mo thin film contact stability. *Thin Solid Films* **201,** 361–371 (1991).

182. Kohara, N., Nishiwaki, S., Hashimoto, Y., Negami, T. & Wada, T. Electrical properties of the Cu (In, Ga) Se 2/MoSe 2/Mo structure. *Sol. Energy Mater. Sol. Cells* **67,** 209–215 (2001).

183. Rostan, P. J., Mattheis, J., Bilger, G., Rau, U. & Werner, J. H. Formation of transparent and ohmic ZnO: Al/MoSe 2 contacts for bifacial Cu (In, Ga) Se 2 solar cells and tandem structures. *Thin Solid Films* **480,** 67–70 (2005).

184. Yoon, J. *et al.* Electrical properties of CIGS/Mo junctions as a function of MoSe2 orientation and Na doping. *Prog. Photovoltaics Res. Appl.* **22,** 90–96 (2014).

185. Abou-Ras, D. *et al.* Formation and characterisation of MoSe2 for Cu(In,Ga)Se2 based solar cells. *Thin Solid Films* **480–481,** 433–438 (2005).

186. Wada, T., Kohara, N., Nishiwaki, S. & Negami, T. Characterization of the Cu (In, Ga) Se 2/Mo interface in CIGS solar cells. *Thin Solid Films* **387,** 118–122 (2001).

187. Kamikawa-Shimizu, Y. *et al.* Effects of Mo back contact thickness on the properties of CIGS solar cells. *Phys. status solidi* **206,** 1063–1066 (2009).

188. Fisher, D. C. *et al.* The effect of Mo morphology on the performance of Cu (In, Ga) Se/sub 2/thin films. in *Photovoltaic Specialists Conference, 2005. Conference Record of the Thirty-first IEEE* 371–374 (IEEE, 2005).

189. Würz, R. *et al.* Formation of an interfacial MoSe 2 layer in CVD grown CuGaSe 2 based thin film solar cells. *Thin Solid Films* **431,** 398–402 (2003).

190. Li, Z. *et al.* Mo back contact for flexible polyimide substrate Cu (In, Ga) Se2 thin-film solar cells. *Chinese Phys. Lett.* **25,** 3452 (2008).

191. Luo, S. *et al.* Strength, stiffness, and microstructure of Cu(In,Ga)Se2 thin films deposited via

sputtering and co-evaporation. *Appl. Phys. Lett.* **105,** 11907 (2014).

192. Green, M. & Emery, K. Solar cell efficiency tables (version 39). *Prog. Photovolt Res. Appl.* 12–20 (2012). doi:10.1002/pip

193. Chirilă, A. *et al.* Highly efficient Cu(In,Ga)Se2 solar cells grown on flexible polymer films. *Nat. Mater.* **10,** 857–61 (2011).

194. T.Nakada, T.Yagioka, K.Horiguchi, T.Kuraishi, T. M. CIGS thin film solar cells on flexible foils. in *proceedings of the 24th european photovoltaic solar energy conference* 2425– 2428 (2009).

195. Agilent. *Agilent Nano Indenter G200 User Manual*. (2013).

196. Greer, J. R., Oliver, W. C. & Nix, W. D. Size dependence of mechanical properties of gold at the micron scale in the absence of strain gradients. *Acta Mater.* **53,** 1821–1830 (2005).

197. Lee, S.-W., Han, S. M. & Nix, W. D. Uniaxial compression of fcc Au nanopillars on an MgO substrate: The effects of prestraining and annealing. *Acta Mater.* **57,** 4404–4415 (2009).

198. Verma, a. S., Sharma, S., Bhandari, R., Sarkar, B. K. & Jindal, V. K. Elastic properties of chalcopyrite structured solids. *Mater. Chem. Phys.* **132,** 416–420 (2012).

199. Stoney, G. G. The Tension of Metallic Films Deposited by Electrolysis. *Proc. R. Soc. Lond. A* **82,** 172–175 (1909).

200. Feng, X., Huang, Y. & Rosakis, a. J. On the Stoney Formula for a Thin Film/Substrate System With Nonuniform Substrate Thickness. *J. Appl. Mech.* **74,** 1276 (2007).

201. Hertz, H. Über die Berührung fester elastischer Körper. *J. für die reine und Angew. Math.* **92,** 156–171 (1881).

202. Hysitron. *Hysitron TI 950 TriboIndenter User Manual*. (2012).

203. Lin, Y.-C. *et al.* Residual stress in CIGS thin film solar cells on polyimide: simulation and experiments. *J. Mater. Sci. Mater. Electron.* (2013). doi:10.1007/s10854-013-1610-7

204. Rincon. Microhardness-bulk modulus scaling and pressure-induced phase transformations in AIBIIIC2 VI chalcopyrite compounds. *J. Appl. Phys. Vol.* **86,** 2355–2357 (1999).

205. Sneddon, I. N. The relation between load and penetration in the axisymmetric boussinesq problem for a punch of arbitrary profile. *Int. J. Eng. Sci.* **3,** 47–57 (1965).

206. Lin, T.-Y., Chen, C. & Lai, C.-H. Mo effect on one-step sputtering chalcopyrite CIGS thin films. in *2012 38th IEEE Photovoltaic Specialists Conference* 001999–002002 (IEEE, 2012). doi:10.1109/PVSC.2012.6317989

207. Chirila, a. *et al.* CIGS solar cells grown by a three-stage process with different evaporation rates. in *2009 34th IEEE Photovoltaic Specialists Conference (PVSC)* 000812–000816 (IEEE, 2009). doi:10.1109/PVSC.2009.5411161

208. Rudmann, D. *et al.* Effects of Na on The Growth of Cu(In, Ga)Se2 Thin Films and Solar Cells.

MRS Proc. **763,** B1.9 (2011).

209. Sun, X., Jiang, F. & Feng, J. Roles of sodium induced defects in CuInSe2 by first principles calculation. *Comput. Mater. Sci.* **47,** 31–34 (2009).

210. Ishizuka, S. *et al.* Alkali incorporation control in Cu(In,Ga)Se[sub 2] thin films using silicate thin layers and applications in enhancing flexible solar cell efficiency. *Appl. Phys. Lett.* **93,** 124105 (2008).

211. Shafarman, W. & Zhu, J. Effect of substrate temperature and depostion profile on evaporated Cu (InGa) Se 2 films and devices. *Thin Solid Films* **362,** 473–477 (2000).

212. Yoon, J.-H. *et al.* High-temperature stability of molybdenum (Mo) back contacts for CIGS solar cells: a route towards more robust back contacts. *J. Phys. D. Appl. Phys.* **44,** 425302 (2011).

213. Aberle, A. G. Surface passivation of crystalline silicon solar cells: a review. *Prog. Photovoltaics Res. Appl.* **8,** 473–487 (2000).

214. Luo, S. *et al.* Suppression of surface recombination in CuInSe2 (CIS) thin films via Trioctylphosphine Sulfide (TOP:S) surface passivation. *Acta Mater.* **106,** 171–181 (2016).

215. Vermang, B., Fjällström, V., Pettersson, J., Salomé, P. & Edoff, M. Development of rear surface passivated Cu(In,Ga)Se2 thin film solar cells with nano-sized local rear point contacts. *Sol. Energy Mater. Sol. Cells* **117,** 505–511 (2013).

216. Vermang, B. *et al.* Employing Si solar cell technology to increase efficiency of ultra-thin Cu(In,Ga)Se 2 solar cells. *Prog. Photovoltaics Res. Appl.* **22,** 1023–1029 (2014).

217. Hsu, W.-W. *et al.* Surface passivation of Cu(In,Ga)Se2 using atomic layer deposited Al2O3. *Appl. Phys. Lett.* **100,** 23508 (2012).

218. Chen, H. C. *et al.* Large auag alloy nanoparticles synthesized in organic media using a one-pot reaction: Their applications for high-performance bulk heterojunction solar cells. *Adv. Funct. Mater.* **22,** 3975–3984 (2012).

219. Wong, T.-H. *et al.* Surface Passivation of CuInSe2 with Trioctylphosphine Sulfide. in *MRS Spring Meeting & Exhibit* (2013).

220. Kemell, M., Ritala, M. & Leskelä, M. Thin Film Deposition Methods for CuInSe 2 Solar Cells. *Crit. Rev. Solid State Mater. Sci.* **30,** 1–31 (2005).

221. Wei, S.-H., Zhang, S. B. & Zunger, A. Effects of Na on the electrical and structural properties of CuInSe2. *J. Appl. Phys.* **85,** 7214 (1999).

222. Choi, P.-P., Cojocaru-Mirédin, O., Wuerz, R. & Raabe, D. Comparative atom probe study of Cu(In,Ga)Se2 thin-film solar cells deposited on soda-lime glass and mild steel substrates. *J. Appl. Phys.* **110,** 124513 (2011).

223. Choi, P.-P., Cojocaru-Mirédin, O. & Wuerz, R. Compositional gradients and impurity distributions in CuInSe 2 thin-film solar cells studied by atom probe tomography. *Surf.*

Interface Anal. **44,** 1386–1388 (2012).

224. Xiao, H., Tahir-Kheli, J. & Goddard, W. A. Accurate Band Gaps for Semiconductors from Density Functional Theory. *J. Phys. Chem. Lett.* **2,** 212–217 (2011).

225. Xiao, H. & Goddard, W. A. Predicted roles of defects on band offsets and energetics at CIGS (Cu(In,Ga)Se₂/CdS) solar cell interfaces and implications for improving performance. *J. Chem. Phys.* **141,** 94701 (2014).

226. Wu, T.-T. *et al.* Toward high efficiency and panel size 30×40cm2 Cu(In,Ga)Se2 solar cell: Investigation of modified stacking sequences of metallic precursors and pre-annealing process without Se vapor at low temperature. *Nano Energy* **10,** 28–36 (2014).

227. Madelung, O. *Semiconductors: Data Handbook*. (Springer Berlin Heidelberg, 2004). doi:10.1007/978-3-642-18865-7

228. Becke, A. D. Density-functional thermochemistry.III. The role of exact exchange. *J. Chem. Phys.* **98,** 5648 (1993).

229. CRYSTAL 2009 User's Manual. *Cryst. 2009 User's Man.* (2009).

230. Melius, C. F. & Goddard, W. A. Ab initio effective potentials for use in molecular quantum mechanics. *Phys. Rev. A* **10,** 1528–1540 (1974).

231. Melius, C. F., Olafson, B. D. & Goddard, W. A. Fe and Ni AB initio effective potentials for use in molecular calculations. *Chem. Phys. Lett.* **28,** 457–462 (1974).

232. Stevens, W. J., Krauss, M., Basch, H. & Jasien, P. G. Relativistic compact effective potentials and efficient, shared-exponent basis sets for the third-, fourth-, and fifth-row atoms. *Can. J. Chem.* **70,** 612–630 (1992).

233. Monkhorst, H. J. & Pack, J. D. Special points for Brillouin-zone integrations. *Phys. Rev. B* **13,** 5188–5192 (1976).

234. Yakushev, M. V. *et al.* Optical properties and band gap energy of CuInSe2 thin films prepared by two-stage selenization process. *J. Phys. Chem. Solids* **64,** 2005–2009 (2003).

235. Kang, S. H., Kim, Y.-K., Choi, D.-S. & Sung, Y.-E. Characterization of electrodeposited CuInSe2 (CIS) film. *Electrochim. Acta* **51,** 4433–4438 (2006).

236. Kodigala, S. R. *Cu(In1-xGax)Se2 Based Thin Film Solar Cells*. (Academic Press, 2011).

237. Jaffe, J. & Zunger, A. Defect-induced nonpolar-to-polar transition at the surface of chalcopyrite semiconductors. *Phys. Rev. B* **64,** 241304 (2001).

238. Bröker, S. *et al.* Correlating the Local Defect-Level Density with the Macroscopic Composition and Energetics of Chalcopyrite Thin-Film Surfaces. *ACS Appl. Mater. Interfaces* **7,** 13062–13072 (2015).

239. Mönig, H. *et al.* Heat Induced Passivation of CuInSe 2 Surfaces: A Strategy to Optimize the Efficiency of Chalcopyrite Thin Film Solar Cells? *Adv. Mater. Interfaces* **1,** n/a-n/a (2014).

240. Vermang, B., Fjallstrom, V., Gao, X. & Edoff, M. Improved Rear Surface Passivation of Cu(In,Ga)Se2 Solar Cells: A Combination of an Al2O3 Rear Surface Passivation Layer and Nanosized Local Rear Point Contacts. *IEEE J. Photovoltaics* **4,** 486–492 (2014).

241. Miller, E. A. & Richmond, G. L. Photocorrosion of n-GaAs and Passivation by Na 2 S: A Comparison of the (100), (110), and (111)B Faces. *J. Phys. Chem. B* **101,** 2669–2677 (1997).

242. Kronik, B. L., Cahen, D. & Schock, H. W. Effects of Sodium on Polycrystalline Cu(In,Ga)Se 2 and Its Solar Cell Performance**. *Adv. Mater.* **10,** 31–36 (1998).

243. Hiepko, K. *et al.* Diffusion and incorporation of Cd in solar-grade Cu(In,Ga)Se2 layers. *Appl. Phys. Lett.* **99,** 234101 (2011).

244. Bastek, J. *et al.* Zinc diffusion in polycrystalline Cu(In,Ga)Se2 and single-crystal CuInSe2 layers. *Appl. Phys. Lett.* **101,** 74105 (2012).

245. Komatsu, Y., Fujiki, Y., Michiue, Y., Yajima, Y. & Sasaki, T. Solvent Extraction Separation of Alkaline Earth Metal Ions with Thenoyltrifluoroacetone and Trioctylphosphine Oxide in Carbon Tetrachloride. *Solvent Extr. Ion Exch.* **9,** 471–479 (1991).

246. Wegst, U. G. K., Bai, H., Saiz, E., Tomsia, A. P. & Ritchie, R. O. Bioinspired structural materials. *Nat. Mater.* **14,** 23–36 (2014).

247. Kumar, M. N. V. R. A review of chitin and chitosan applications. *React. Funct. Polym.* **46,** 1–27 (2000).

248. Sun, J. & Bhushan, B. Hierarchical structure and mechanical properties of nacre: a review. *Rsc Adv.* **2,** 7617–7632 (2012).

249. Weiner, S. & Wagner, H. D. The material bone: structure-mechanical function relations. *Annu. Rev. Mater. Sci.* **28,** 271–298 (1998).

250. Schmid, A.-M. M. & Schulz, D. Wall morphogenesis in diatoms: Deposition of silica by cytoplasmic vesicles. *Protoplasma* **100,** 267–288 (1979).

251. Ji, B. & Gao, H. Mechanical principles of biological nanocomposites. *Annu. Rev. Mater. Res.* **40,** 77–100 (2010).

252. Barthelat, F., Yin, Z. & Buehler, M. J. Structure and mechanics of interfaces in biological materials. *Nat. Rev. Mater.* **1,** 16007 (2016).

253. Ritchie, R. O. The conflicts between strength and toughness. *Nat. Mater.* **10,** 817 (2011).

254. Ritchie, R. O., Buehler, M. J. & Hansma, P. Plasticity and toughness in bone. (2009).

255. Currey, J. D. & Taylor, J. D. The mechanical behaviour of some molluscan hard tissues. *J. Zool.* **173,** 395–406 (1974).

256. Jackson, A. P., Vincent, J. F. V & Turner, R. M. The mechanical design of nacre. *Proc. R. Soc. London B Biol. Sci.* **234,** 415–440 (1988).

257. Currey, J. D. Mechanical properties of mother of pearl in tension. *Proc. R. Soc. London B*

Biol. Sci. **196,** 443–463 (1977).

258.   Wang, R. Z., Suo, Z., Evans, A. G., Yao, N. & Aksay, I. A. Deformation mechanisms in nacre. *J. Mater. Res.* **16,** 2485–2493 (2001).

259.   Cölfen, H. & Antonietti, M. Mesocrystals: inorganic superstructures made by highly parallel crystallization and controlled alignment. *Angew. Chemie Int. Ed.* **44,** 5576–5591 (2005).

260.   Rousseau, M. *et al.* Multiscale structure of sheet nacre. *Biomaterials* **26,** 6254–6262 (2005).

261.   Rabiei, R., Bekah, S. & Barthelat, F. Failure mode transition in nacre and bone-like materials. *Acta Biomater.* **6,** 4081–4089 (2010).

262.   Barthelat, F., Tang, H., Zavattieri, P. D., Li, C.-M. & Espinosa, H. D. On the mechanics of mother-of-pearl: a key feature in the material hierarchical structure. *J. Mech. Phys. Solids* **55,** 306–337 (2007).

263.   Barthelat, F. & Rabiei, R. Toughness amplification in natural composites. *J. Mech. Phys. Solids* **59,** 829–840 (2011).

264.   Barthelat, F. & Espinosa, H. D. An experimental investigation of deformation and fracture of nacre–mother of pearl. *Exp. Mech.* **47,** 311–324 (2007).

265.   Launey, M. E., Buehler, M. J. & Ritchie, R. O. On the Mechanistic Origins of Toughness in Bone. *Annu. Rev. Mater. Res.* **40,** 25–53 (2010).

266.   Rho, J.-Y., Kuhn-Spearing, L. & Zioupos, P. Mechanical properties and the hierarchical structure of bone. *Med. Eng. Phys.* **20,** 92–102 (1998).

267.   Buehler, M. J. Nature designs tough collagen: explaining the nanostructure of collagen fibrils. *Proc. Natl. Acad. Sci.* **103,** 12285–12290 (2006).

268.   Uzel, S. G. M. & Buehler, M. J. Molecular structure, mechanical behavior and failure mechanism of the C-terminal cross-link domain in type I collagen. *J. Mech. Behav. Biomed. Mater.* **4,** 153–161 (2011).

269.   Buehler, M. J. Molecular nanomechanics of nascent bone: fibrillar toughening by mineralization. *Nanotechnology* **18,** 295102 (2007).

270.   Hassenkam, T. *et al.* High-resolution AFM imaging of intact and fractured trabecular bone. *Bone* **35,** 4–10 (2004).

271.   Fratzl, P. & Weinkamer, R. Nature's hierarchical materials. *Prog. Mater. Sci.* **52,** 1263–1334 (2007).

272.   Shen, Z. L., Dodge, M. R., Kahn, H., Ballarini, R. & Eppell, S. J. Stress-strain experiments on individual collagen fibrils. *Biophys. J.* **95,** 3956–3963 (2008).

273.   Launey, M. E., Chen, P.-Y., McKittrick, J. & Ritchie, R. O. Mechanistic aspects of the fracture toughness of elk antler bone. *Acta Biomater.* **6,** 1505–14 (2010).

274.   Jäger, I. & Fratzl, P. Mineralized collagen fibrils: a mechanical model with a staggered

arrangement of mineral particles. *Biophys. J.* **79,** 1737–1746 (2000).

275. Fantner, G. E. *et al.* Sacrificial bonds and hidden length dissipate energy as mineralized fibrils separate during bone fracture. *Nat. Mater.* **4,** 612 (2005).

276. Nalla, R. K., Kruzic, J. J., Kinney, J. H. & Ritchie, R. O. Mechanistic aspects of fracture and R-curve behavior in human cortical bone. *Biomaterials* **26,** 217–231 (2005).

277. Koester, K. J., Ager, J. W. & Ritchie, R. O. The true toughness of human cortical bone measured with realistically short cracks. *Nat. Mater.* **7,** 672–677 (2008).

278. Werner, D. *The Biology of Diatoms*. (Blackwell, 1977).

279. Bradbury, J. Nature's Nanotechnologists: Unveiling the Secrets of Diatoms. *PLoS Biol.* **2,** e306 (2004).

280. Pondaven, P. *et al.* Grazing-induced Changes in Cell Wall Silicification in a Marine Diatom. *Protist* **158,** 21–28 (2007).

281. Stoermer, E. & Julius, M. in *Freshwater Algae of North America: Ecology and Classification* pp 559–594 (Elsevier, 2002).

282. Finkel, Z. V. & Kotrc, B. Silica Use Through Time: Macroevolutionary Change in the Morphology of the Diatom Fustule. *Geomicrobiol. J.* **27,** 596–608 (2010).

283. Almqvist, N. *et al.* Micromechanical and structural properties of a pennate diatom investigated by atomic force microscopy. *J. Microsc.* **202,** 518–32 (2001).

284. Subhash, G., Yao, S., Bellinger, B. & Gretz, M. R. Investigation of mechanical properties of diatom frustules using nanoindentation. *J. Nanosci. Nanotechnol.* **5,** 50–6 (2005).

285. Hamm, C. E. *et al.* Architecture and material properties of diatom shells provide effective mechanical protection. *Nature* **421,** 841–843 (2003).

286. Losic, D., Short, K., Mitchell, J. G., Lal, R. & Voelcker, N. H. AFM nanoindentations of diatom biosilica surfaces. *Langmuir* **23,** 5014–21 (2007).

287. Bjørnøy, S. H. Nanomechanical testing of diatoms. (2012).

288. Vebner, M. Nanomechanical Testing of Diatoms. (2013).

289. Schaedler, T. A. *et al.* Ultralight Metallic Microlattices. *Science (80-.).* **334,** 962–965 (2011).

290. Huang, J., Wang, X. & Wang, Z. L. Controlled replication of butterfly wings for achieving tunable photonic properties. *Nano Lett.* **6,** 2325–2331 (2006).

291. Saranathan, V. *et al.* Structure, function, and self-assembly of single network gyroid (I4132) photonic crystals in butterfly wing scales. *Proc. Natl. Acad. Sci.* **107,** 11676–11681 (2010).

292. Weaver, J. C. *et al.* The stomatopod dactyl club: a formidable damage-tolerant biological hammer. *Science (80-.).* **336,** 1275–1280 (2012).

293. Grunenfelder, L. K. *et al.* Bio-inspired impact-resistant composites. *Acta Biomater.* **10,** 3997–

4008 (2014).

294.   Jang, D., Meza, L. R., Greer, F. & Greer, J. R. Fabrication and deformation of three-dimensional hollow ceramic nanostructures. *Nat. Mater.* **12,** 893–8 (2013).

295.   Xu, C., Gallant, B. M., Wunderlich, P. U., Lohmann, T. & Greer, J. R. Three-Dimensional Au Microlattices as Positive Electrodes for Li–O 2 Batteries. *ACS Nano* **9,** 5876–5883 (2015).

296.   Maggi, A., Allen, J., Desai, T. & Greer, J. R. Osteogenic cell functionality on 3-dimensional nano-scaffolds with varying stiffness. *Extrem. Mech. Lett.* **13,** 1–9 (2017).

297.   Chernow, V. F., Alaeian, H., Dionne, J. A. & Greer, J. R. Polymer lattices as mechanically tunable 3-dimensional photonic crystals operating in the infrared. *Appl. Phys. Lett.* **107,** 101905 (2015).

298.   Aitken, Z. H., Luo, S., Reynolds, S. N., Thaulow, C. & Greer, J. R. Microstructure provides insights into evolutionary design and resilience of Coscinodiscus sp. frustule. *Proc. Natl. Acad. Sci.* **113,** 2017–2022 (2016).

299.   Stoermer, E. F. & Julius, M. L. Centric Diatoms. *Freshw. Algae North Am. Ecol. Classif.* 559–594 (2003). doi:10.1016/B978-012741550-5/50016-7

300.   Kröger, N., Deutzmann, R., Bergsdorf, C. & Sumper, M. Species-specific polyamines from diatoms control silica morphology. *Proc. Natl. Acad. Sci. U. S. A.* **97,** 14133–8 (2000).

301.   Moore, T. M. The Total Release Method for FIB In-Situ TEM Sample Preparation. *Micros. Today* **13,** 40–42 (2005).

302.   Oliver, W. C. & Pharr, G. M. Measurement of hardness and elastic modulus by instrumented indentation: Advances in understanding and refinements to methodology. *J. Mater. Res.* **19,** 3–20 (2011).

303.   Li, C.-W. & Volcani, B. E. Aspects of Silicification in Wall Morphogenesis of Diatoms. *Philos. Trans. R. Soc. B Biol. Sci.* **304,** 519–528 (1984).

304.   Gordon, R. & Drum, R. W. The Chemical Basis of Diatom Morphogenesis. *Int. Rev. Cytol.* **150,** 243–372 (1994).

305.   Rogerson, A., Defreitas, A. S. W. & Mcinnes, A. G. Observations on Wall Morphogenesis in Coscinodiscus asteromphalus (Bacillariophyceae) Observations on Wall Morphogenesis in Coscinodiscus asteromphalus Since the introduction of scanning electron microscopy in the late 1960 â€™ s , diatoms have been favor. *Trans. Am. Microsc. Soc.* **105,** 59–67 (1986).

306.   Schmid, A.-M. M. & Volcani, B. E. WALL MORPHOGENESIS IN COSCINODISCUS WAILESII GRAN AND ANGST. I. VALVE MORPHOLOGY AND DEVELOPMENT OF ITS ARCHITECTURE. *J. Phycol.* **19,** 387–402 (1983).

307.   Hildebrand, M. *et al.* Nanoscale control of silica morphology and three-dimensional structure during diatom cell wall formation. *J. Mater. Res.* **21,** 2689–2698 (2011).

308.   Iler, R. K. *The Chemistry of Silica: Solubility, Polymerization, Colloid and Surfae Properties*

and Biochemistry. (Wiley-Interscience, 1979).

309. Bridoux, M. C. & Ingalls, A. E. Structural identification of long-chain polyamines associated with diatom biosilica in a Southern Ocean sediment core. *Geochim. Cosmochim. Acta* **74,** 4044–4057 (2010).

310. Hench, L. L. Bioceramics. *J. Am. Ceram. Soc.* **81,** 1705–1728 (2005).

311. Meyers, M. A., Chen, P.-Y., Lin, A. Y.-M. & Seki, Y. Biological materials: Structure and mechanical properties. *Prog. Mater. Sci.* **53,** 1–206 (2008).

312. Wegst, U. G. K. & Ashby, M. F. The mechanical efficiency of natural materials. *Philosophical Magazine* **84,** 2167–2186 (2004).

313. Vollrath, F., Madsen, B. & Shao, Z. The effect of spinning conditions on the mechanics of a spider's dragline silk. *Proc. Biol. Sci.* **268,** 2339–2346 (2001).

314. Brambilla, G. & Payne, D. N. The ultimate strength of glass silica nanowires. *Nano Lett.* **9,** 831–835 (2009).

315. Sumper, M. & Kröger, N. Silica formation in diatoms: the function of long-chain polyamines and silaffins. *J. Mater. Chem.* **14,** 2059 (2004).

316. Poulsen, N., Sumper, M. & Kroger, N. Biosilica formation in diatoms: Characterization of native silaffin-2 and its role in silica morphogenesis. *Proc. Natl. Acad. Sci.* **100,** 12075–12080 (2003).

317. Bridoux, M. C., Annenkov, V. V, Keil, R. G. & Ingalls, A. E. Widespread distribution and molecular diversity of diatom frustule bound aliphatic long chain polyamines (LCPAs) in marine sediments. *Org. Geochem.* **48,** 9–20 (2012).

318. Pohnert, G. Biomineralization in diatoms mediated through peptide- and polyamine-assisted condensation of silica. *Angewandte Chemie - International Edition* **41,** 3167–3169 (2002).

319. Luo, S. & Greer, J. R. Capturing the geometry, microstructure and mechanical properties of marine diatom frustules using nanoscale 3-D silica structures. *Placeholder*

320. Moon, J. H., Seo, J. S., Xu, Y. & Yang, S. Direct fabrication of 3D silica-like microstructures from epoxy-functionalized polyhedral oligomeric silsesquioxane (POSS). *J. Mater. Chem.* **19,** 4687 (2009).

321. Xu, Y., Zhu, X. & Yang, S. Crack-Free 3D Hybrid Microstructures from Photosensitive Organosilicates as Versatile Photonic Templates. *ACS Nano* **3,** 3251–3259 (2009).

322. Ayandele, E., Sarkar, B. & Alexandridis, P. Polyhedral Oligomeric Silsesquioxane (POSS)-Containing Polymer Nanocomposites. *Nanomaterials* **2,** 445–475 (2012).

323. Hench, L. L. *An Introduction to Bioceramics*. (World Scientific, 1993).

324. ASTM. E 1820-15 Standard Test Method for Measurement of Fracture Toughness. *Annu. B. ASTM Stand.* 1–56 (2001). doi:10.1520/E1820-15

325. Baratta, F. in *Methods for Assessing the Structural Reliability of Brittle Materials* 194-194–29 (ASTM International). doi:10.1520/STP35245S

326. Baratta, F. & Matthews, W. *Errors Associated with Flexural Testing of Brittle Materials*. (1987).

327. Kopesky, E. T., Haddad, T. S., McKinley, G. H. & Cohen, R. E. Miscibility and viscoelastic properties of acrylic polyhedral oligomeric silsesquioxane-poly(methyl methacrylate) blends. *Polymer (Guildf).* **46,** 4743–4752 (2005).

328. Chandra Kishen, J. M. & Kumar, A. Finite element analysis for fracture behavior of cracked beam-columns. *Finite Elem. Anal. Des.* **40,** 1773–1789 (2004).